Alma Mater Studiorum · Università di Bologna

SCUOLA DI SCIENZE

Dipartimento di Fisica e Astronomia

Corso di Laurea Magistrale in Astrofisica e Cosmologia

Constraints on Magnetic fields and particle acceleration in the inter-cluster bridge A399–A401

Candidato:

Marco Balboni

Relatore:

Prof.ssa Annalisa Bonafede

Correlatore:

Dott. Gianni Bernardi

Sessione II

Anno Accademico 2020/2021

Contents

Abstract

Galaxy clusters are the most massive gravitationally bound structures in the Universe. In the past decades, diffuse non-thermal emission coming from these objects has been widely studied, unveiling complex internal structures and tracing the presence of energetic particles and magnetic fields. Theoretical and numerical models have been proposed to explain radio emission on such large scales, invoking particle (re-)acceleration mechanisms and magnetic field amplification processes. Yet, many aspects of this environment are still unclear, in particular regarding the magnetic field structure and origins.

With the advent of the LOw Frequency ARray (LOFAR), new observations in the low frequency range ($10 - 240$ MHz) have been achieved. In particular, unprecedented signatures of diffuse radio emission were found in clusters, providing further information about known objects and unveiling new ones.

Beyond the cluster environment, elongated filaments of matter (galaxies, dark matter and magnetized gas) are located between clusters, forming an even larger unbound structure, known as the *Cosmic Web*. Galaxy clusters are located at the nodes of this web, and interact with each other through this network with matter accretion and merger events. Numerical models predict that, during these processes, a high amount of energy is released in the inter-cluster medium. A small fraction of this energy can accelerates particles and amplifies magnetic fields, and, eventually, produce radio emission. Radio emission is therefore a unique tracer of magnetic fields on the largest scale structure of the Universe, allowing to place putative constraints on primordial magnetic fields.

Recent LOFAR observations have detected filaments of diffuse synchrotron emission (*bridge*) connecting two merging galaxy clusters, Abell 399 and Abell 401 (Govoni et al., 2019). Such result is the first observational evidence of radio emission coming from an inter-cluster region, tracing the presence of relativistic particles and magnetic fields in-between clusters. The origin of this non-thermal component is still uncertain, although Govoni et al. (2019) suggested that it could be caused by multiple weak

shocks, that are produced during the merger process, and generate highly polarized ($\sim 70\%$) emission.

In this thesis, we have used new LOFAR observations to study the polarized emission in the A399–A401 inter-cluster region. We made use of the Rotation Measure synthesis technique, that allows to recover information about the magnetic field weighted by the thermal gas density along the line of sight. As we did not detect polarized emission from the bridge, we proceeded to compare our results with the shock-driven emission model proposed by (Govoni et al., 2019).
Through this comparison, we evidenced the presence of a depolarization process which, reduces the radiation degree of polarization. In particular, we investigated the case of an external medium with a turbulent magnetic field inside. From this analysis we obtained limits on such depolarization model to be compared with numerical predictions. Then, we analyzed the bridge emission model proposed by Govoni et al. (2019), deriving simulated bridge properties like density and magnetic field intensity. Finally, the further comparison between simulated and observational results allowed us to provide, for the first time, a lower limit of an inter-cluster magnetic field.

This thesis is organized as follows:

- In **Chapter 1** we introduce the properties of both galaxy cluster and the inter-clusters region/cosmic web, with a focus on the non-thermal emission.

- In **Chapter 2** we describe the basics concepts of the radio observations, providing also an overview about LOFAR.

- In **Chapter 3** we describe the Faraday rotation effect and the Rotation Measure synthesis (RM synthesis) technique, which will be used in this thesis work and allows to recover the polarized emission of the observed target in the presence of a Faraday rotating medium.

- In **Chapter 4** we describe the analysis performed in this thesis: we present new polarization images of the bridge field, showing no detection of bridge polarized emission. We perform injection of a bridge emission model inside the real data, finding evidence for depolarization compatible with an external screen. Then, we derive constraints to the bridge non-thermal properties that can be responsible for the depolarization of the emission. Our results are in agreement with the shock-driven emission model proposed by Govoni et al. (2019). Thus, assuming such model for the bridge emission, we obtain lower limits on the bridge magnetic field.

- In **Chapter 5** we summarize the results and conclude. In particular, we compare our results with other limits on B in cluster outskirts and filaments.

Sommario

Gli ammassi di galassie sono gli oggetti più massivi dell'Universo legati gravitazionalmente. Nei decenni passati si è studiata l'emissione diffusa e non termica provenienete da questi oggetti, rivelando complesse strutture e tracciando la presenza di particelle energetiche e campi magnetici. Per giustificare un'emissione radio su così grande scala, sono stati proposti modelli teorici e numerici, i quali prevedevono meccanismi di ri-accelerazione delle particelle e amplificazione dei campi magnetici. Nonostante ciò, diversi aspetti di tale emissione non sono ancora chiari, soprattutto nel contesto di struttura e origine del campo magnetico.

Grazie all'interferometro di nuova generazione LOFAR, LOw Frequency ARray, è stato possibile studiare gli ammassi di galassie anche alle basse frequenze (10 - 240 MHz). Come risultato di tali osservazioni, sono state rivelate caratteristiche peculiari all'interno degli ammassi mai osservate prima, fornendo nuove informazioni sulla natura di questi oggetti.

Gli ammassi di galassie non sono strutture isolate. Infatti, lunghi filamenti di materia (galassie, materia oscura e gas magnetizzato) sono presenti nelle regioni tra gli ammassi, formando una complessa struttura detta *Cosmic Web*. Gli ammassi di galassie si trovano nei nodi di questa struttura e interagiscono tra loro attraverso di essa, accrescendo materia o generando fenomeni di merger. Durante tali eventi i modelli numerici prevedono che una grande quantità di energia venga rilasciata nel mezzo inter-cluster. Una frazione di questa energia genera un'accelerazione di particelle e amplificazione dei campi magnetici, causando una conseguente emissione non termica nella banda radio. Di conseguenza, gli studi radio sono ottimali per tracciare il campo magnetico durante tali eventi, permettendo, inoltre, di porre vincoli anche sul campo magnetico primordiale.

Recenti osservazioni condotte con LOFAR, hanno rivelato un'estesa (*bridge*) emissione da sincrotrone localizzata tra due ammassi di galassie in avvicinamento, Abell 0399 e Abell 0401 (Govoni et al., 2019). Tale risultato, mostra la prima evidenza di

un'emissione radio proveniente da una area inter-ammassi di galassie e, di conseguenza, traccia in essa la presenza di campi magnetici e particelle relativistiche. L'origine di questa emissione è ancora incerto. Govoni et al. (2019) hanno proposto che potrebbe essere originata da diversi shock tra i due ammassi, i quali, originatesi durante il processo di merging, produrrebbero una radiazione altamente polarizzata ($\sim 70\%$).

In questa tesi, abbiamo analizzato nuovi dati ottenuti con LOFAR per studiare l'emissione polarizzata proveniente dalla regione tra Abell 0399 e Abell 0401. A questo scopo, abbiamo utilizzato la tecnica di Rotation Measure synthesis, la quale permette anche di ottenerre informazioni sul campo magnetico lungo la linea di vista, pesato per la densità del mezzo in cui si trova. Poiché non abbiamo rivelato alcuna emissione polarizzata, abbiamo confrontato i nostri risultati con il modello a shock proosto da (Govoni et al., 2019).
Da tale confronto, abbiamo evidenziato la presenza di un meccanismo di depolarizzazione il quale riduce la quantità di radiazione polarizzata proveniente dal bridge. In particolare, abbiamo studiato il caso di depolarizzazione causata da un mezzo esterno permeato da un campo magnetico turbolento. Da questa analisi abbiamo ottenuto limiti su tale modello di depolarizzazione e li abbiamo nuovamente confrontati con le predizioni numeriche. Perciò, abbiamo analizzato il modello a shock proposto in Govoni et al. (2019), derivando parametri come densità e campo magnetico da poter poi confrontare con i dati osservativi. Il successivo confronto tra simulazioni e osservazioni, ci ha permesso di porre, per la prima volta, un limite inferiore al campo magnetico in una regione inter-ammassi.

Il seguente lavoro è organizzato come segue:

- Nel **Capitolo 1** introduciamo le proprietà degli ammassi di galassie e delle regioni tra di essi. In particolare, ci focalizziamo sull'emissione non termica da tali regioni.
- Nel **Capitolo 2** presentiamo i concetti base dell'interferometria, mostrando, inoltre, le caratteristiche del nuovo inteferometro LOFAR.
- Nel **Capitolo 3** descriviamo la rotazione di Faraday e la tecnica della Rotation Measure synthesis (RM synthesis), che verrà poi utilizzata nella tesi, e che permette di derivare l'emissione polarizzata di un oggetto anche in presenza di rotazione di Faraday.
- Nel **Capitolo 4** descriviamo l'analisi fatta in questa tesi: presentiamo le nuove immagini in polarizzazione ottenute, le quali mostrano assenza di emissione polarizzata dal bridge. In seguito, descriviamo il processo di "iniezione" di un modello

di emissione del bridge all'interno dei dati scientifici, mostrando evidenza di depolarizzazione causata da uno schermo di Faraday esterno. Dopodiché, otteniamo vincoli per le proprietà non termiche della regione del bridge responsabili della depolarizzazione. Ciò che troviamo è che i nostri risultati sono in accordo con le previsioni del modello proposto in (Govoni et al., 2019). Infine, assumendo tale modello per l'emissione del bridge, ricaviamo un limite inferiore sull'intensità del campo magnetico del bridge.

- Nel **Capitolo 5** riassumiamo i risultati e li discutiamo.

1. Galaxy clusters and the Cosmic web

1.1 Clusters of galaxies

Galaxy clusters are the most massive gravitationally bound structures in the Universe, with typical masses of about $10^{14} - 10^{15} M_{\odot}$ and virial radii (R_{vir}) of $\sim$ 1 Mpc . Clusters of galaxies have been firstly identified in optical observations as concentrations of galaxies but, contrary to their name, are more than just a collection of galaxies. Indeed, they might have been called something different if they had first been discovered in a waveband other than visible light, because all the stars in all of a cluster's galaxies represent only a small fraction of a cluster overall mass. In the 1930s, Zwicky (1937) discovered that it requires a large amount of unseen matter to bind the fast moving galaxies in the Coma cluster into a long lasting object. Today we know that most of the cluster mass, $\sim$ 80%, is in the form of dark matter, while the baryonic matter constitutes only a small fraction, $\sim$ 20%, of the total mass. The baryonic component is mainly in form of a hot ($\sim 10^7 - 10^8$ K), tenuous ($\sim 10^{-3}$ cm^{-3}) plasma known as Intra Cluster Medium (ICM), whereas stars and galaxies represent only a few percent of the total mass.
Galaxy clusters are not isolated but connected by elongated filaments of matter that form a large unbound structure, known as the Cosmic Web. Galaxy clusters are located at the nodes of this web, accreting matter flowing through filaments. This accretion process is at the very base of the hierarchical scenario for the structures formation, including the formation of clusters through a sequence of mergers of clusters and groups (e.g. Voit, 2005; Peebles and Yu, 1970; Press and Schechter, 1974)

1.1.1 Emission from galaxy clusters

Galaxy clusters observations can be performed in different bands. In fact, in addition to the optical and Infra-Red (IR) light produced by the galaxies, there is an important thermal emission from the ICM in the X-rays. In addition, radio observations have

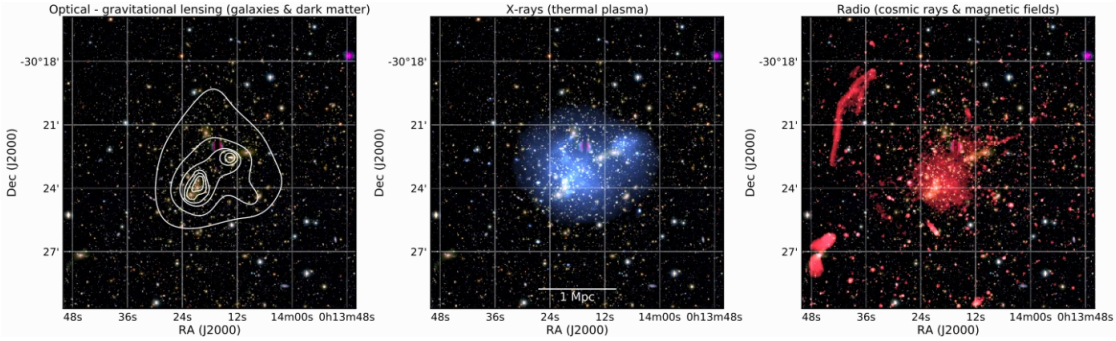

Figure 1.1: Optical, X-ray and radio view of the galaxy cluster Abell 2744. White contours on the optical (*left*) image represent the mass surface density derived from weak lensing. In the middle panel the $0.5 - 2$ keV X-ray emission (blue) reveals the thermal ICM. The radio emission (red) at 1.4 GHz is shown in the *right* panel (van Weeren et al., 2019).

shown that in some clusters the ICM can also contain a non-thermal component of cosmic rays, which is emitting radiation in the radio band. As a consequence of these two emission mechanisms, galaxy clusters can be observed both in the X-ray and in the radio band, as well as in the optical range.

Optical emission

The optical and near-IR emission from galaxy clusters is predominantly starlight. The galaxy populations in clusters is mainly constituted by ellipticals and lenticulars (i.e., early-type galaxies). This is particularly true in the central regions, where the largest and most luminous galaxies are found. The old and relatively homogeneous nature of their stellar populations leads the majority of cluster galaxies to occupy a relatively narrow and distinctive locus known as the "red sequence" (Allen et al., 2011, and references therein). Therefore, galaxy colors can help identify distant clusters because many cluster galaxies are significantly redder than other galaxies at a similar redshift, owing to their lack of ongoing star formation (Voit, 2005).

X-ray emission

Clusters of galaxies are X-ray sources because galaxy formation is inefficient. Only about a tenth of the total amount of baryons in the Universe resides within stars and galaxies, leaving the vast majority adrift in intergalactic space in form of a diffuse medium which is difficult to observe (Voit, 2005). Within galaxy clusters, however, gravity and shocks squeeze the gas, heating it to virial temperatures of $10^7 - 10^8$ K, leading to X-ray emission through the bremsstrahlung mechanism. Galaxy clusters therefore 'light up' at X-ray wavelengths as luminous, continuous, spatially-extended

sources.

The primary X-ray emission mechanisms from the diffuse ICM are collisional: free-free emission; free-bound (recombination) emission; and bound-bound emission (mostly line radiation) (Allen et al., 2011). Hence, the shape of the spectrum is determined by the plasma temperature, density and chemical abundances (Böhringer and Werner, 2010). However, the chemical analysis is generally trivial to perform, thus, the main quantities that one usually derives from the spectrum shape are temperature, density and chemical composition of the gas. The temperature and the density are well constrained by the shape and the normalization of the continuum spectrum, dominated by bremsstrahlung, whether the element abundances (e.g. iron, oxygen, and silicon) are mostly reflected in the intensity of the spectral lines (Böhringer and Werner, 2010).

Further investigations can be done by using these first information obtained from the spectrum. As an example, the gas temperature inferred from a cluster's X-ray spectrum can be used as a proxy for estimating the depth of a cluster's potential well and so allowing studies on the matter (dark matter) that generates this potential.

Radio emission

Galaxy clusters are also observed in the radio band due to emission from both compact sources and extended sources. Radio emission from compact sources comes from the Active Galactic Nuclei (AGNs) harbored in cluster galaxies, that emit radio synchrotron emission. The sizes of these sources range from a few kpc up to $\sim$ 1 Mpc, extending well beyond the host galaxy (van Weeren et al., 2019). A major difference with radio galaxies that are located outside clusters (and groups) is that the jets and lobes of cluster radio galaxies often show signs of interaction with the ICM, leading to the so-called wide-angle, narrow angle and "head-tail" radio source morphologies (van Weeren et al., 2019, and references therein).

Radio observations have shown that the ICM also contains a non-thermal component (cosmic rays) which is not directly associated to cluster radio galaxies. In fact, GeV cosmic ray electrons (CRe) emit, in the presence of $\sim$ μGauss magnetic fields, synchrotron radiation on Mpc scales (van Weeren et al., 2019, and references therein). During the last decade, significant progress has been made in our understanding of this non-thermal component, through observations, theoretical, and numerical work. There is now compelling evidence that ICM shocks waves, and likely also turbulence, are able to (re-)accelerate particle to relativistic energies creating this non-thermal CR component (van Weeren et al., 2019).

The presence of extended synchrotron emission also indicates the existence of large-scale ICM magnetic fields with a strength of the order of $0.1 - 10$ μGauss (e.g. Brüggen et al., 2012; Clarke et al., 2001). Cluster magnetic fields play an important role in

particle acceleration processes and inhibit transport processes like heat conduction, spatial mixing of gas, and the propagation of cosmic rays (e.g. Pfrommer et al., 2017; Ruszkowski and Oh, 2010). However, few details are known about the precise properties of these fields since they are difficult to measure (van Weeren et al., 2019).

1.2 Diffuse radio emission in galaxy clusters

As previously anticipated, diffuse radio emission from non-thermal plasma has been detected inside galaxy clusters. Despite this extended emission is always due to synchrotron radiative processes, differences have been observed in radio diffuse emitting regions. In particular, a classification of diffuse cluster radio sources has been made, and here we refer to the classification proposed by van Weeren et al. 2019. Before introducing this classification, we provide a description of the synchrotron theory and the current knowledge of magnetic fields inside galaxy clusters.

1.2.1 Synchrotron theory

Synchrotron radiation, is produced by the motion of relativistic electrons in a magnetic field. It is commonly assumedn that CRe follow a power-law energy distribution

$$n(E)\,dE \propto E^{-\delta} dE, \tag{1.1}$$

For a homogeneous and isotropic population of electrons with a power law energy distribution, the total intensity spectrum S is described by a power law too

$$S(\nu) \propto \nu^{-\alpha}, \tag{1.2}$$

where the spectral index α is related to the index of the energy (or momentum) distribution δ as

$$\delta = 1 + 2\alpha. \tag{1.3}$$

The power law spectrum can be further modified by other effects, like self absorption of the radiation and energy losses. In particular, below the frequency where the synchrotron emitting region becomes optically thick, the total intensity spectrum can be described by:

$$S(\nu) \propto \nu^{5/2}. \tag{1.4}$$

An example of synchrotron spectrum that shows both the optically thick and thin regions is shown in (Fig. 1.2).
When energy losses become important, the spectrum steepens at higher frequencies,

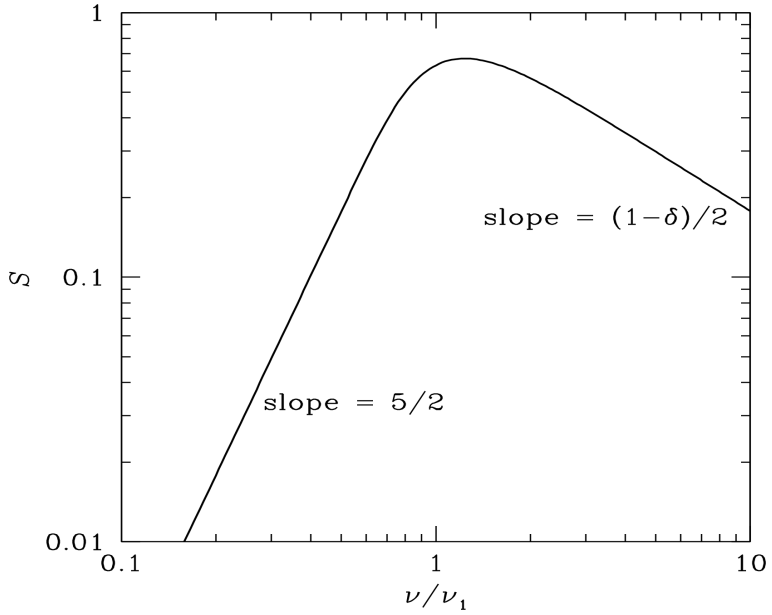

Figure 1.2: The spectrum of an homogeneous synchrotron source (real astrophysical sources are inhomogeneous, so their low-frequency spectral slopes are smaller than 5/2 and their spectral peaks are not so sharp). The spectrum turns over at frequencies smaller than ν_1 where the plasma becomes optically thick (Condon and Ransom, 2016).

i.e. $\alpha' = \alpha + 0.5$ (Fig. 1.3).

Diffuse cluster radio emission typically has a steep spectral index, i.e. $\alpha \geq 1$, depending upon the physics of the acceleration mechanism and the energy losses (synchrotron, inverse-Compton).

Synchrotron emission radiating from a population of relativistic electrons in a uniform magnetic field is linearly polarized. In the optically thin case, the degree of intrinsic linear polarization p_i for a homogeneous and isotropic distribution of relativistic electrons with a power-law spectrum as in Eq. 1.1, is:

$$p_i = \frac{3\delta + 3}{3\delta + 7}, \tag{1.5}$$

independent of frequency and viewing angle, and with the electric (polarization) vector perpendicular to the projection of the magnetic field lines onto the plane of the sky. The intrinsic polarization degree can be as high as $\sim 75 - 80\%$ for typical spectral index values, although, in practice, the observed polarization degree is often smaller due to several effects that will be described in the following sections.

The characteristic life time $t_{\rm age}$ of a synchrotron source depends upon the competition between radiative losses and the energy lost due to the Inverse-Compton (IC)

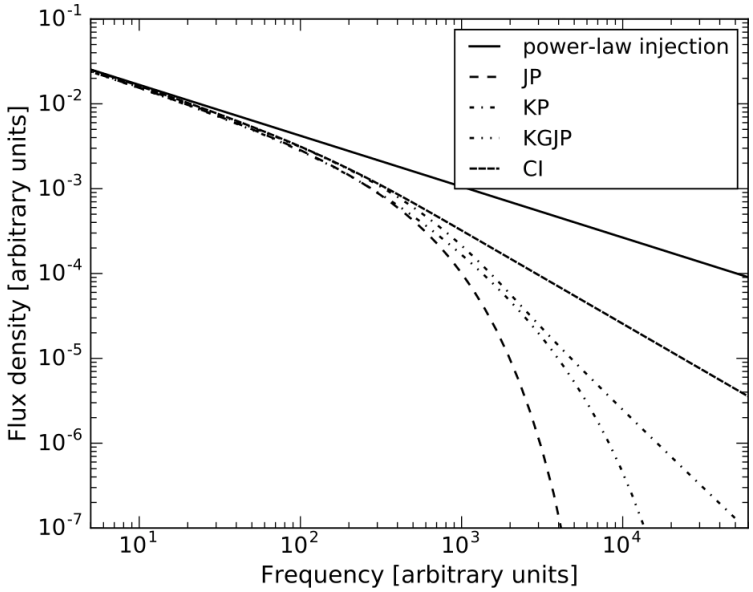

Figure 1.3: Spectra for different synchrotron models (from van Weeren et al., 2019). All models have $\alpha_{inj} = -0.6$. The power-law spectrum depicts the spectral shape before any energy losses.

scattering between relativistic electrons and Cosmic Microwave Background (CMB):

$$t_{\rm age} \approx 3.2 \times 10^{10} \frac{B^{0.5}}{B^2 + B^2_{\rm CMB}} [(1+z)\,\nu]^{-1/2} \text{ yr} \tag{1.6}$$

Where B is the magnetic field strength, z the source redshift, $B_{\rm CMB}$ the equivalent magnetic field strength of the CMB ($B_{\rm CMB}[\mu{\rm G}] \simeq 3.25(1+z)^2$), and ν the observing frequency in MHz. In clusters, we have $t_{\rm age} \lesssim 10^8$ yr. Making the standard assumptions on CRe velocities inside clusters, the typical diffusion length-scale in the ICM of a GeV electron is of the order of 10s kpc (for more details see Brunetti and Jones, 2014). This means that Mpc-scale diffuse radio sources cannot be generated by CR electrons that are accelerated at a single location in the ICM, but they need to be re-accelerated or produced in-situ.

There are several physical mechanisms that can accelerate particles in the ICM and produce the synchrotron emission:

- **Diffuse shock acceleration (DSA)**: In this Fermi I-like process, particles are accelerated thanks to the presence of a shock, with the acceleration taking place diffusively. In this process, particles cross back and forth across the shock front as they scatter from magnetic inhomogeneities in the shock down and upstream region. At each crossing, particles gain additional energy, forming a power-law energy distribution of CR (van Weeren et al., 2019).

- **Second order Fermi acceleration (Fermi II)**: This is a stochastic pro-

cess where particles scatter from magnetic inhomogeneities, for example from magneto-hydrodynamical (MHD) turbulence (e.g. Schlickeiser et al., 1987; Brunetti et al., 2001). Particles can either gain or loose energy when scattering, but when motions are random, the probability of a head-on collision, where energy is gained, is slightly larger (van Weeren et al., 2019). Because of its random nature, second order Fermi acceleration is an inefficient process.

- **Adiabatic Compression**: Old relativistic radio plasma, produced, for instance, in the past from an AGN, can be compressed adiabatically by a shock wave. With this process, old electrons regain energy boosting the radio synchrotron emission (Enßlin and Gopal-Krishna, 2001; Bruggen et al., 2003).

- **Secondary models**: In this models, radio emitting electrons are present over large scale not because an in-situ acceleration, but thanks to an in-situ production of relativistic particles via secondary processes. This implies that CR electrons are produced as a secondary particles, for example, during collisions between relativistic protons and thermal ions (hadronic model). Since the very long lifetime of CR protons compared to CR electrons, they can be produced in a compact region in the cluster (e.g. AGN, shock, etc..) and then diffuse over the entire cluster extension (Dennison, 1980; Blasi and Colafrancesco, 1999; Enßlin, T. et al., 2011).

1.2.2 Magnetic fields in galaxy clusters

The presence of synchrotron emission also implies that magnetic fields permeate galaxy clusters on Mpc-scales, with typical intensity of $0.1 - 10$ μG (Beck and Krause, 2005; van Weeren et al., 2019). Magnetic fields play key roles in particle acceleration and in the process of large scale structure formation, having effects on turbulence, cloud collapse, large-scale motions, heat and momentum transport, convection and viscous dissipation. In particular, cluster magnetic fields inhibit transport processes like heat conduction, spatial mixing of gas, and propagation of cosmic rays (van Weeren et al., 2019)

The origin of the observed magnetic fields remains largely uncertain. A commonly accepted hypothesis is that they result from the amplification of much weaker, pre-existing seeds via shock/compression and/or turbulence/dynamo mechanisms during merger events and structure formation, and different magnetic field scales survive as the result of turbulent motions (see Donnert et al., 2018, for a review on magnetic field amplification).

The origin of seed fields is unknown. They could be either primordial, i.e. generated in the early Universe prior to recombination, or produced locally at later epochs of the

Universe, in early stars and/or (proto)galaxies, and then injected in the interstellar and intergalactic medium. Another fount of magnetic field are the astrophysical sources at low redshift ($z \leq 6$). These, on their side, can inject magnetic field inside the circumgalactic medium and cosmic voids, during the star formation process through ejecta of magnetized winds.

The discriminant among these models is the magnetic field strength on large scales, like filaments, sheets and voids. Simulations show that the magnetic field profile resulting from different models tends to diverge in the periphery of galaxy clusters due to the different efficiency with which each model produces large-scale magnetic fields (Vazza et al., 2017; Donnert et al., 2018).
An example of such differences is the dependence of the magnetic field on the gas density. In fact, the magnetic field strength in the case of a primordial seeds field scales as $n^{2/3}$, where n is the gas density. Instead, if the magnetic fields are originated by dynamo amplification of weaker initial seeds, there is a stronger dependence on gas density because the increase of solenoidal motions in denser regions (Vazza et al., 2017).
Observations of magnetic fields on such scales may be able to discriminate amongst models.

Equipartition assumption

The usual assumption made in order to estimate the magnetic field from a radio source is to minimize its total energy content U_t. For a synchrotron emitting source, this quantity is given by the particle energy (electrons, U_e, and protons, U_p) and the magnetic field energy (U_B):

$$U_t = U_e + U_r + U_B. \tag{1.7}$$

The magnetic field energy contained in the source volume V is given by:

$$U_B = \frac{B^2}{8\pi}\,\Phi\,V \tag{1.8}$$

where Φ is the filling factor, i.e. the fraction of the volume occupied by the magnetic field. The electron total energy in the range between a minimum energy ϵ_1 and a maximum energy ϵ_2:

$$U_e = V \times \int_{\epsilon_1}^{\epsilon_2} N(\epsilon)\,d\epsilon = V N_0 \int_{\epsilon_1}^{\epsilon_2} \epsilon^{-\delta+2}\,d\epsilon \tag{1.9}$$

can be expressed as a function of the synchrotron luminosity L_s (Govoni and Feretti, 2004) obtaining:

$$U_{el} = C_{12}(\alpha, \epsilon_1, \epsilon_2)\,L_s\,B^{-3/2}, \tag{1.10}$$

(where α is the spectral index). Then, assuming a linear relation between the energy contained in protons and electrons:

$$U_p = k\, U_e,$$

the total energy can be written as a function of the magnetic field:

$$U_{tot} = (1+k)\, C_{12}\, L_s\, B^{-3/2} + \frac{B^2}{8\pi}\, \Phi\, V. \tag{1.11}$$

In order to obtain an estimate of the magnetic field, minimal energy is usually assumed, which implying that the magnetic field and particles energies are roughly the same:

$$U_B = \frac{3}{4}\,(1+k)\, U_e. \tag{1.12}$$

For this reason the minimum energy is known as *equipartition* value:

$$U_t(\mathrm{min}) = \frac{7}{4}\,(1+\mathrm{k})\,\mathrm{U_e} = \frac{7}{3}\,\mathrm{U_B}. \tag{1.13}$$

The magnetic field for which the total energy content is minimum is:

$$B_{eq} = 6\pi\,(1+k)\, C_{12}\, \frac{L_s}{\Phi V}. \tag{1.14}$$

There are several uncertainties in the determination of magnetic field strengths. The value of k, ratio of the energy in relativistic protons to that in electrons, depends on the mechanism of generation of relativistic electrons, which is poorly known so far. Uncertainties are also related to the volume filling factor Φ. Values usually assumed in literature for clusters are $k = 1$ (or $k = 0$) and $\Phi = 1$ (Govoni and Feretti, 2004).

Faraday rotation effect

The Faraday rotation effect occurs during the propagation of electromagnetic waves in a magnetized plasma. A linearly polarized wave can be decomposed into two opposite-handed circularly polarized components. The right-handed and left-handed circularly polarized waves propagate with different phase velocities within the magneto-ionic material. This effectively rotates the plane of polarization of the electromagnetic wave (Govoni and Feretti, 2004). If a wave travels a path length L, the intrinsic polarization angle Ψ_0 will be rotated by an angle $\Delta\Psi$, according to:

$$\Psi_{Obs} = \Psi_0 + \Delta\Psi. \tag{1.15}$$

It is possible to derive that the change in the polarization angle, $\Delta\Psi$, for an external screen located between the source of radiation and the observer, that is not emitting polarized radiation (also called *simple Faraday screen*), is given by (Govoni and Feretti, 2004):

$$\Delta\Psi = \frac{e^2\lambda^2}{2\pi m_e^2 c^4}\int_0^L n_e\, B_\parallel\, dl \propto \lambda^2\phi, \tag{1.16}$$

where e is the electron charge, m_e is the electron mass, λ is the wavelength, c is the light speed, n_e is the electron density, $B_\parallel$ is the magnetic field component parallel to the line - of - sight (los) and ϕ is the *Faraday depth* and is equal to:

$$\phi = \frac{e^2}{2\pi m_e^2 c^4}\int_0^L n_e\, B_\parallel\, dl, \tag{1.17}$$

which is the term that contains the information about the magnetic field and the particle distribution of the medium crossed by the radiation.
This technique to measure the magnetic field is the one chosen for this thesis work. Therefore a more detailed description of such technique will be provided in Chapter 3.

Magnetic field from IC emission

When the synchrotron radio and IC X-ray emission are produced by the same population of relativistic electrons the total synchrotron and IC powers are related (Govoni and Feretti, 2004). The IC emissivity is proportional to the energy density in the photon field, u_{ph}, which, for typical IC processes with the CMB photons, is well know from the CMB radiation field. As the synchrotron emissivity is proportional to the energy density in the magnetic field, $u_B = B^2/8\pi$, This leads to a simple proportionality relation between L_{sync} and L_{IC} :

$$\frac{L_s}{L_{IC}} \propto \frac{u_B}{u_{ph}}, \tag{1.18}$$

from such relation (see van Weeren et al., 2019) it is possible to derive an expression for the magnetic field:

$$B = \left(\frac{20\,\mathrm{keV}}{kT}\right)\left(\frac{\nu}{\mathrm{GHz}}\right)^{(\delta-1)/(\delta+1)} e^{\frac{2.84(\delta-r)}{\delta+1}}\,\mu\mathrm{G} \tag{1.19}$$

$$r = 0.7\, ln\left[\frac{R_{obs}(kT,\nu)}{1.11\times10^{-8}}\right] \tag{1.20}$$

$$R_{obs}(kT,\nu) = \frac{f_{IC}(kT)}{f_{sync}(\nu)} \tag{1.21}$$

where f_{IC} and f_{sync} are the IC and synchrotron fluxes, respectively, and δ is the slope of the electron energy distribution. Such expression is correct if the power law assumption holds also at low frequencies, if not, the magnetic field will be overestimated (van Weeren et al., 2019, and reference therein).
The main problem of this method is that X-ray detections due to IC from synchrotron emitting electrons are difficult to obtain. In fact, extended cluster sources, such as radio halos (See Sec. 1.2.3), are typically faint objects whose emission, in particular at high energies (hard X-ray), is challenging to detect (Govoni and Feretti, 2004). Moreover, these extended sources are co-spatial with the thermal ICM which emits in the X-ray too, making it harder to separate the components. Furthermore, bright radio galaxies are usually located in the clusters center and can also produce non-thermal X-ray emission. Hence, for extended cluster sources, one typically derives upper limit on the IC X-ray emission. Combining such upper limits with the information from the radio band, lower limit on the global ICM magnetic fields can be obtained (van Weeren et al., 2019). Typical values of this limit are in the range $0.1 - 0.5$ μG (e.g. Rossetti and Molendi, 2004; Wik et al., 2009).

1.2.3 Diffuse radio cluster source classification

There are several types of radio sources in the ICM. Here we classify the radio diffuse cluster sources in three broad classes: **radio halos**, **cluster radio relics**, **revived AGN fossil plasma sources** (phoenices and GReET).

Radio halos

With radio halo one refers to an extended structure, located at the cluster centre, that roughly follows the ICM gas density spatial distribution. A general property of this class is that these sources are not localized, in the sense that particle re-acceleration, or production, occurs throughout a significant volume of the cluster and is not associated with presence of shock (Fig 1.4). As so, these sources should trace Fermi II and/or secondary electrons production.

Actually, a further division inside this class can be made. In fact, we distinguish between *Giant radio halo* and *Mini-halo* diffuse sources, which differ in some aspects.

Giant radio halo are extended sources that roughly follow the brightness distribution of the ICM, with a smooth regular morphology. At 1.4 GHz they are not common sources and are mostly found in massive dynamically disturbed clusters (e.g. Cuciti et al., 2021).
As their emission is co-spatial with X-ray emission, giant radio halos have a typical

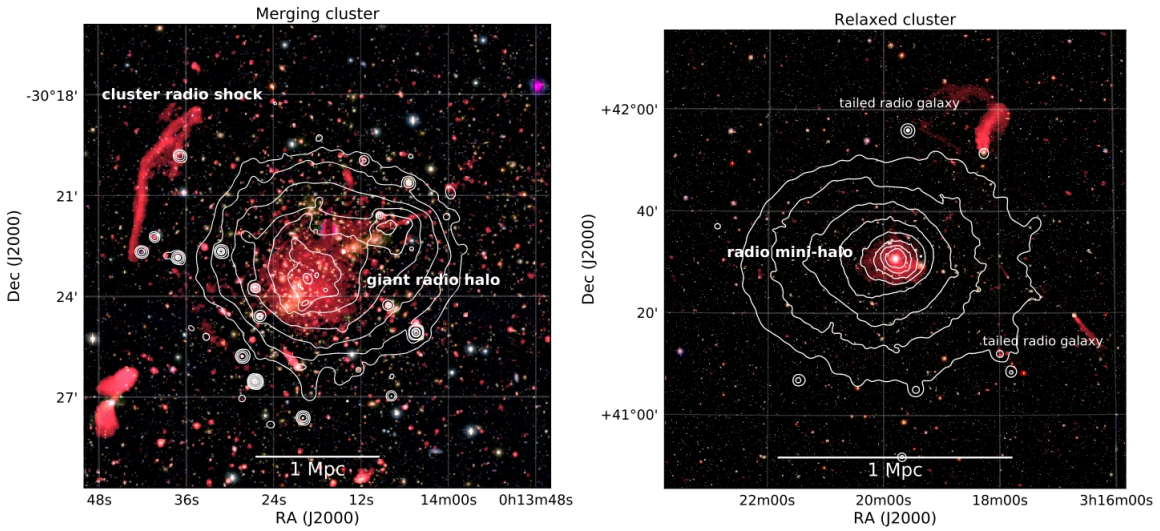

Figure 1.4: Left panel: VLA 1−4 GHz image of the merging galaxy cluster Abell 2744 with different source classes labeled (from Pearce et al., 2017). Right panel: VLA 230–470 MHz image of the relaxed cool core Perseus cluster (from Gendron-Marsolais et al., 2017). X-ray contours are shown in white.

Mpc size. Along with Fermi II mechanisms, there are also the *hadronic models* that could explain radio halos emission (van Weeren et al., 2019). However, the latter are not able to justify steep spectra ($\alpha \geq 1.5$) and, in addition, they predict gamma-ray emission which has not been observed yet by the *Fermi* telescope (van Weeren et al., 2019).

Most radio halos have integrated spectral indices in the range $-1.4 < \alpha < -1$ (e.g. Giovannini et al., 2009). Few studies at more than two frequencies for these structure have been made so far, then there is a lack of information about the spectrum of these sources (van Weeren et al., 2019). With future spectral studies, in particular regarding the change of spectral index with the frequency, important constraints on the origins of radio halos will be inferred.

Finally, radio halos are largely unpolarized.

Mini-halos are diffuse sources with $\sim 100 - 500$ kpc size and are found in relaxed cool core clusters, with the radio emission surrounding the central radio loud brightest cluster galaxy.

Compared to giant radio halos, their synchrotron volume emissivities of mini-halos are generally higher. However, since the mini-halo emission surrounds the central radio galaxy, whose lobes often have excavated cavities in the X-ray emitting gas, the separation between AGN lobes and mini-halos can be difficult (Mazzotta and Giacintucci, 2008). Because of this, X-ray observations provide help to the identification and classification of mini-halos (e.g Bagchi et al., 2009).

As for giant radio halos, few detailed studies have been made on the spectral index,

which, however, seems to be similar to giant halos. Investigate on mini-halos spectral index would provide also information on the origin of CR electrons, allowing to discriminate between turbulent re-acceleration and secondary models (van Weeren et al., 2019).
Other important studies can be made regarding the possible connection between mini and giant halos. In fact different hints have been found suggesting that during a merger event the mini-halo CRe can be transported in the external regions and re-accelerated again through turbulent motions, originating a giant halo (Brunetti and Jones, 2014). However some observations support this scenario, it is not clear yet what is the transition mechanism between radio mini-halo and the subsequent turbulent acceleration (see van Weeren et al., 2019, and reference therein). Therefore, more information are still required.

Cluster radio shocks (relics)

Cluster radio shocks (or radio relics) are diffuse sources of elongated shape, extending up to Mpc scales, highly polarized ($\gtrsim 20\%$) and with a clear spectral index gradient (see Fig 1.7).
They seems to be less common than radio halos or mini-halos (Kale et al., 2015). In an simple scenario, these sources can be produced during a cluster binary merger. In fact, in an idealized binary merger, 'equatorial' shocks form first and move outwards in the equatorial plane. After the dark matter core passage, two 'merger' shocks lunch into the opposite directions along the merger axis, which can explain the formation of cluster double radio shocks in observed merging clusters (Fig. 1.5).
Radio relics typically have elongated shapes with sizes that roughly range between 0.5

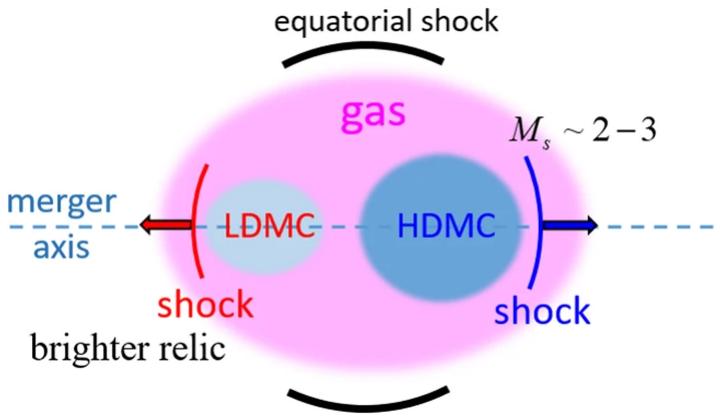

Figure 1.5: Schematic picture of an idealized binary cluster merger about 1 Gyr after core passage. Equatorial shocks expand outwards in the equatorial plane perpendicular to the merger axis, while merger shocks launch in the opposite directions along the merger axis. Typically, the shock ahead of lighter DM core has the higher shock kinetic energy flux and becomes the brighter radio shock. From van Weeren et al. (2019).

to 2 Mpc, see Fig. 1.6. These shapes are expected for sources that trace shock waves in the cluster outskirts and are seen close to edge-on.
Most large radio shocks that are found in the cluster outskirts show asymmetric transverse brightness profiles, with a sharp edge on the side away from the cluster center. On the side of the cluster center, instead, the emission fades more gradually.

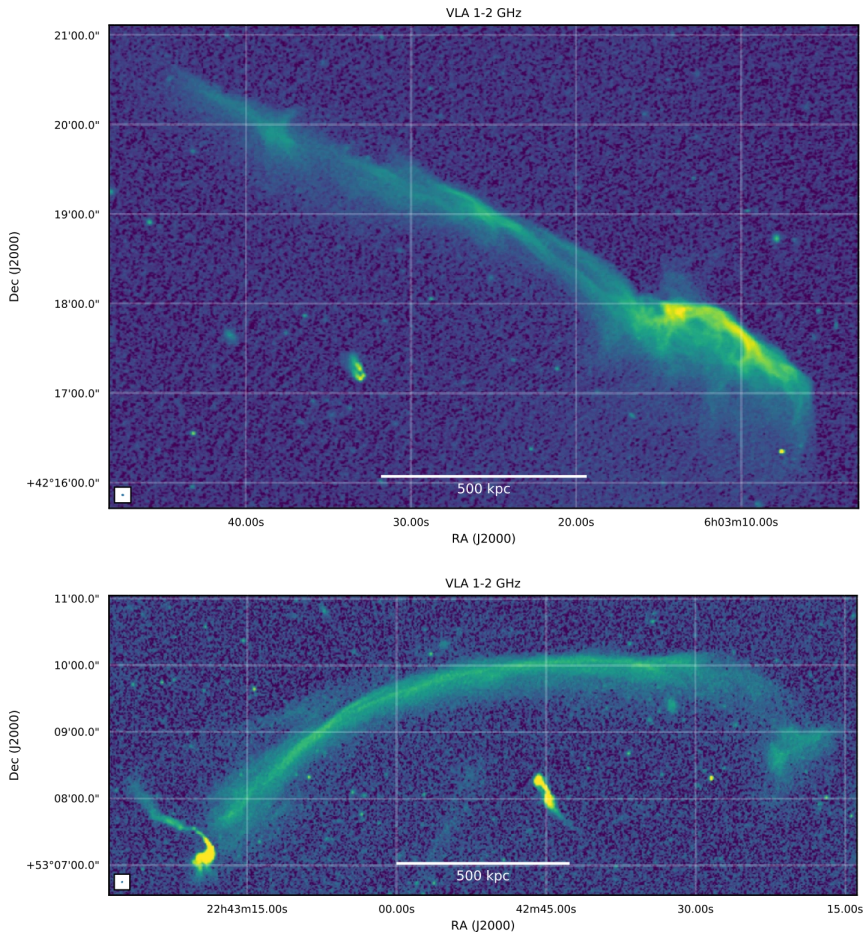

Figure 1.6: VLA $1-2$ GHz high-resolution ($\sim$ 2") images of the shocks in the Toothbrush (top panel; Rajpurohit et al., 2018) and Sausage Cluster (bottom panel; Di Gennaro et al., 2018) respectively. Both images show the multiple filamentary substructures that composes the shock.

Deep high-resolution observations of large elongated radio shocks have also revealed a significant amount of filamentary substructures, as shown in Fig. 1.6. The nature of such structures is not fully understood. One possibility is that they trace changes in the magnetic field. Alternatively, they reflect the complex shape of the shock surfaces (van Weeren et al., 2019). This filamentary morphology of cluster radio shocks seems to be ubiquitous because all radio shocks that have been studied with good signal–to–noise ratio (SNR) and at high resolution display them.

The integrated radio spectra of cluster radio shocks display power-law shapes, with spectral indices ranging from about −1.0 to −1.5. In particular, relics often show a clear spectral index gradient across their width, as presented in Fig. 1.7. Such spectral

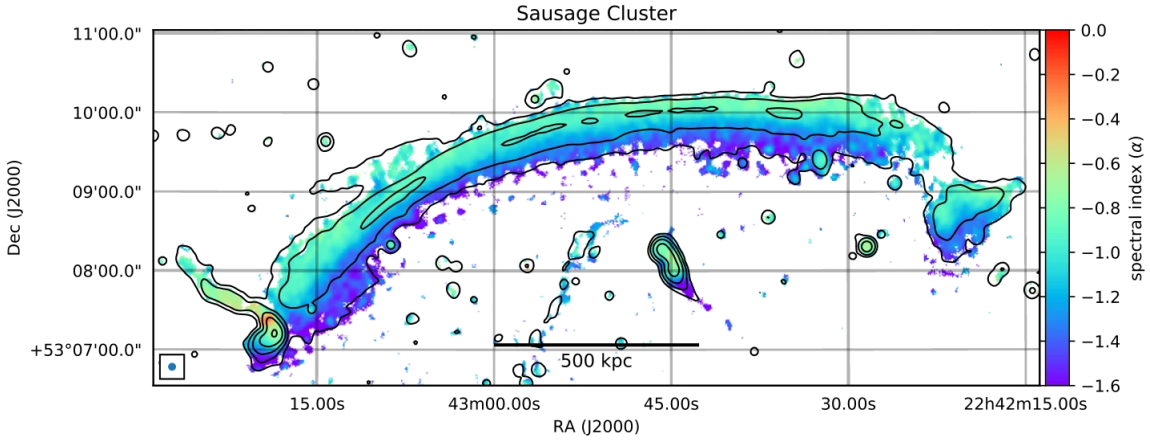

Figure 1.7: Spectral index distribution across the northern cluster radio shock in CIZAJ2242.8+5301 between 0.15 and 3.0 GHz at 5" resolution (Di Gennaro et al., 2018). Black contours are from a 1–4 GHz continuum image (from van Weeren et al., 2019).

index steepening traces the shock (re)-acceleration process. In fact, the region with the flattest spectral index is located near the shock front, away from the cluster center. Then, moving away from the shock front towards the cluster center, the spectral index steepens. This steepening is thought to be caused by synchrotron and IC losses in the shock downstream region.

Another important feature of cluster radio relics is the polarization. These sources are amongst the most polarized sources in the extragalactic sky (up to 70%) and very elongated radio shocks usually show the highest polarization fraction.

Revived AGN fossil plasma

The study of mildly relativistic AGN fossil plasma throughout clusters is and important topic since old populations of relativistic electrons have been invoked as seed particles for the formation of radio halos and cluster radio shocks. They also retrace past AGN activity and constitute a source of non-thermal pressure in the ICM (van Weeren et al., 2019).

Two representative classes of sources of this re-energized emitting plasma are *phoenices* and *GReETs*.

Phoenices are sources which trace old radio plasma from past episodes of AGN activity. When a shock compresses this old plasma, the resulting increase in the momentum of the relativistic electrons and the magnetic field strength can produce a source characterized by a steep and curved radio spectrum (Enßlin and Gopal-Krishna, 2001). However, connection between shocks waves and phoenices is still missing.
Compared to cluster radio shocks, revived fossil plasma sources and phoenices are on average found at smaller cluster centric distances, have smaller sizes, $\lesssim 300 - 400$ kpc and have low radio powers. Moreover, these revived fossil sources have a range of morphologies, from roundish shapes to elongated and filamentary, and with integrated spectra typically steeper than 1.5 and with irregular distribution across the source (van Weeren et al., 2019, and reference therein).
Also polarized emission has been detected coming from phoenices.

GReETs are diffuse radio source originated by the re-acceleration of aged plasma located in the tail of a wide angle tail galaxy. This process of re-energization is so gentle that it barely balances the radiative losses of cosmic rays, with a particle acceleration time-scale comparable to the radiative loss timescale of the electrons emitting at < 100 MHz. Because of this, such sources have been labeled GReETs (Gently Re-energized Tail, Fig 1.8) (van Weeren et al., 2019).
A proposed physical explanation for the re-energization mechanism is that Rayleigh-

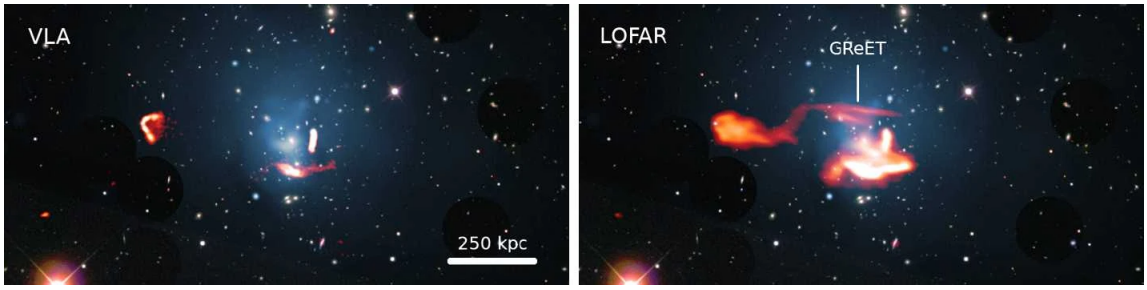

Figure 1.8: Optical image of the galaxy cluster Abell 1033, with over plotted in blue the X-ray emission and in orange the synchrotron radio emission. The left panel shows our view of the galaxy cluster at conventional radio frequencies (VLA at 1.4 GHz). The right panel shows the discovery of the first GReET, visible uniquely at very low frequencies (LOFAR at 140 MHz; de Gasperin et al., 2017) (from van Weeren et al., 2019)

Taylor and Kelvin-Helmholtz instabilities in the tails generate turbulent waves that re-accelerate electrons via second order Fermi mechanisms. The challenge is to understand how the re-acceleration rate is maintained quasi-constant in the tail over a long time-scale. A proposed solution is to assume that turbulence is continuously forced in the tail by the interaction between perturbations in the surrounding medium with the tail itself (de Gasperin et al. 2017).

However, because of the very few examples of GReETs are known, the precise nature of GReETs and their existence as a distinct class of objects remains to be confirmed.

1.3 The cosmic web

The large-scale distribution of matter revealed by galaxy surveys features a complex network of interconnected filamentary galaxy associations. This network, known as the *Cosmic Web* (Bond et al. 1996), contains structures from a few Mpc up to tens and even hundreds of Mpc. The weblike spatial arrangement of galaxies and mass into elongated filaments, sheetlike walls, and dense compact clusters, the existence of large near-empty void regions, and the hierarchical nature of this mass distribution-marked by sub-structure over a wide range of scales and densities are its three major characteristics (Aragón-Calvo et al., 2010). Its appearance has been most dramatically illustrated by the recently produced maps of the nearby cosmos (Fig 1.10), the 2dFGRS, the SDSS, and the 2MASS redshift surveys (e.g. Colless et al. 2003; Ahumada et al. 2020; Huchra et al. 2012).

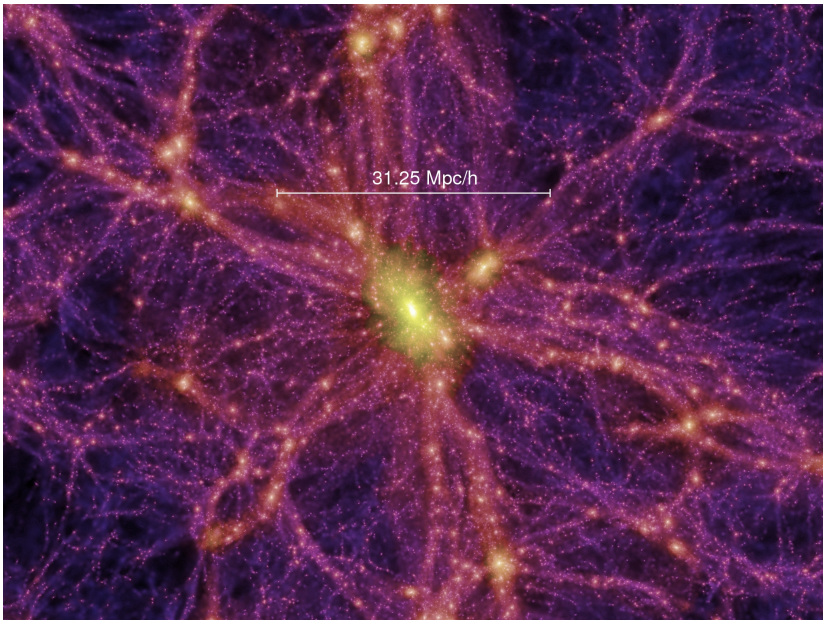

Figure 1.9: A zoom-in of a node in the Cosmic Web in the *Millennium simulation*. The Millennium simulation is one of the largest N-body simulation which traces the distribution and the evolution of matter. In this image, it is showed how an intersection of the cosmic web can be, leading to cluster formation inside nodes (Springel et al., 2005a).

The Cosmic Web is the most salient manifestation of the anisotropic nature of gravitational collapse, the motor behind the formation of structure in the cosmos (Peebles,

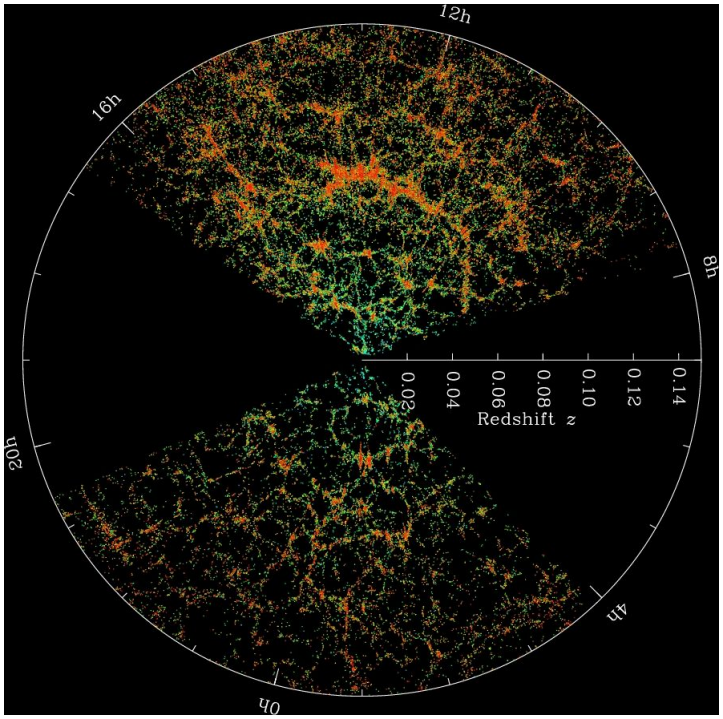

Figure 1.10: The SDSS map of the Universe. Each dot is a galaxy; the color bar shows the local density. One can see that the matter distribution roughly follows a web like pattern, as expected from simulations (credit SloanDigitalSkySurvey-WebSite).

1980). N-body computer simulations have profusely illustrated how a primordial field of tiny Gaussian density perturbations transforms into a pronounced and intricate filigree of filamentary features, characterized by dense compact clumps at the nodes of the network (Fig 1.9; Springel et al., 2005a). The filaments connect into the cluster nodes and act as the transport channels along which matter flows into clusters.

Fundamental understanding of anisotropic collapse on cosmological scales came with the seminal study by Zel'Dovich 1970, who recognized the key role of the large-scale tidal force field in shaping the Cosmic Web. The collapse of a primordial cloud of dark matter passes through successive stages, first assuming a flattened sheet like configuration as it collapses along its shortest axis. This is followed by a rapid evolution toward an elongated filaments the intermediate axis collapses and, if collapse continues along the longest axis, may ultimately produce a dense, compact and virialized cluster or halo (Aragón-Calvo et al., 2010).
The hierarchical setting of these processes, occurring simultaneously over a wide range of scales and modulated by the expansion of the universe, complicates the picture considerably. Modern experiments like the Millennium simulation (Springel et al., 2005a) clearly show the hierarchical nature in which not only the clusters build up but also the filamentary network itself.

The Cosmic Web theory of Bond et al. 1996 succeeded in synthesizing all relevant aspects into a coherent dynamical and evolutionary framework. It is based on the realization that the outline of the Cosmic Web may already be recognized in the primordial density field. The statistics of the primordial tidal field explains why the large-scale universe looks predominantly filamentary and why in over dense regions sheetlike membranes are only marginal features (Pogosyan et al., 2009). Of key importance is the observation that the rare high peaks, which will eventually emerge as clusters, are the dominant agents for generating the large-scale tidal force field: it is the clusters which weave the cosmic tapestry of filaments (Bond et al., 1996; Aragón-Calvo et al., 2010, and references therein). They cement the structural relations between the components of the Cosmic Web and themselves form the junctions at which filaments tie up. This relates the strength and prominence of the filamentary bridges to the proximity, mass, shape, and mutual orientation of the generating cluster peaks: the strongest bridges are those between the richest clusters that stand closely together and point into each other's direction (Aragón-Calvo et al., 2010; Bond et al., 1996).

The emerging picture is one of a primordially and hierarchically defined network whose weblike topology is imprinted over a wide spectrum of scales. Weblike patterns on ever larger scales get to dominate the density field as cosmic evolution proceeds, and as small-scale structures merge into larger ones. Within the gradually emptying void regions, however, the topological outline of the early weblike patterns remains largely visible (Aragón-Calvo et al. 2010).

1.3.1 Non-thermal properties of the large-scale structure

As explained in the previous section, simulations and observations have demonstrated that elongated filaments of matter (galaxies, dark matter and magnetized gas) are located between clusters. Such filamentary structure is filled with a gas, the so called Warm Hot Intergalactic Medium (WHIM). that has a significantly lower density than the ICM, $\lesssim 10^{-4}$ particles cm^{-3}, and cooler temperature, 10^{5-7} K. About half of the Universe baryons reside in this WHIM (Eckert et al. 2015).
Galaxy filaments are expected to be surrounded by strong accretion shocks, where the plasma is first shock-heated (Sunyaev and Zeldovich, 1972; Miniati et al., 2000). However, studying the WHIM and associated shocks is notoriously difficult due to a lack of sensitive observational tools. Owing to their high-Mach numbers ($M \gtrsim 10$), WHIM accretion shocks should accelerate particles (Miniati et al. 2001; Ryu et al. 2003), similar to what happens in clusters. Radio studies of the WHIM would offer a unique diagnostic tool to determine the strength of the WHIM magnetic field and pinpoint

the location of the accretion shocks.
Similarly, cluster mergers can re-energized the non-thermal component of WHIM and amplify magnetic field therein. This phenomenon leads to an enhanced synchrotron emission from such regions that could be detected by observations at low radio frequencies (Govoni et al., 2019; Botteon et al., 2020). In this case, both shocks (Wittor et al., 2019) and turbulent gas motions (Brunetti and Vazza, 2020) can cause the emission, depending on the nature of the process.

In any case, the detection of the very faint radio emission from these regions around galaxy clusters is difficult. With larger catalogs of polarized sources, deep continuum images, and simulations, some progress has already been made in deriving the properties of magnetic fields beyond clusters in the cosmic web (e.g. Xu et al., 2006; Vernstrom et al., 2017). Deep observations with the SKA, LOFAR and other radio telescopes might have the sensitivity to detect radio emission beyond cluster environments and in low mass systems such as groups. A challenge will be to properly classify such emission, since deep observations will also pick up extended low-surface brightness emission associated with (old) radio galaxies (van Weeren et al., 2019).

Despite the expected challenges, some works have already studied synchrotron emission outside clusters. In particular, constraints on the origin and evolution of magnetic field on large scales have been obtained. As described in Sec. 1.2.2, the study of magnetic field in structures like filaments or sheets allows to discern between theoretical models that predict different values of $\overrightarrow{B}$ in those structures.

Vernstrom et al. (2021) used stacking technique to increase the SNR and performing estimates of the magnetic field strength inside inter-cluster regions, obtaining values in the range of $30 - 60$ nG. In addition, based on their results, they stated that the primordial seed magnetic field strength should be higher than the simulated one.

Likewise, O'Sullivan et al. (2020) studied the emission from pairs of compact sources and, exploiting the Faraday rotation effect, obtained an upper limit for the co-moving cosmological magnetic field (B_0) of $B_0 \leq 4$ on Mpc scales. The authors have also compared their results with simulations, testing different magnetogenesis scenarios: a strong initial field, a weak initial field but with dynamo amplification and an astrophysical scenario where $\overrightarrow{B}$ is injected solely by AGN and galactic outflows. What they found was that the astrophysical and primordial scenario are both consistent with the data but the dynamo amplification is disfavoured.

1.3.2 First discovery of a radio bridge

For the first time, a recent study of the LOFAR Two-meter Sky Survey (LoTSS, Shimwell et al. 2017) data, have detected of a radio emission coming from a region located between two merging galaxy clusters, A399 and A401 (Fig. 1.11, Govoni et al. 2019). This unprecedent result have probed the presence of relativistic particles and magnetic fields in the inter-cluster region, originating a "radio bridge" connecting the two clusters.

Such discovery provided new challenges for theoretical models, that, now, have to

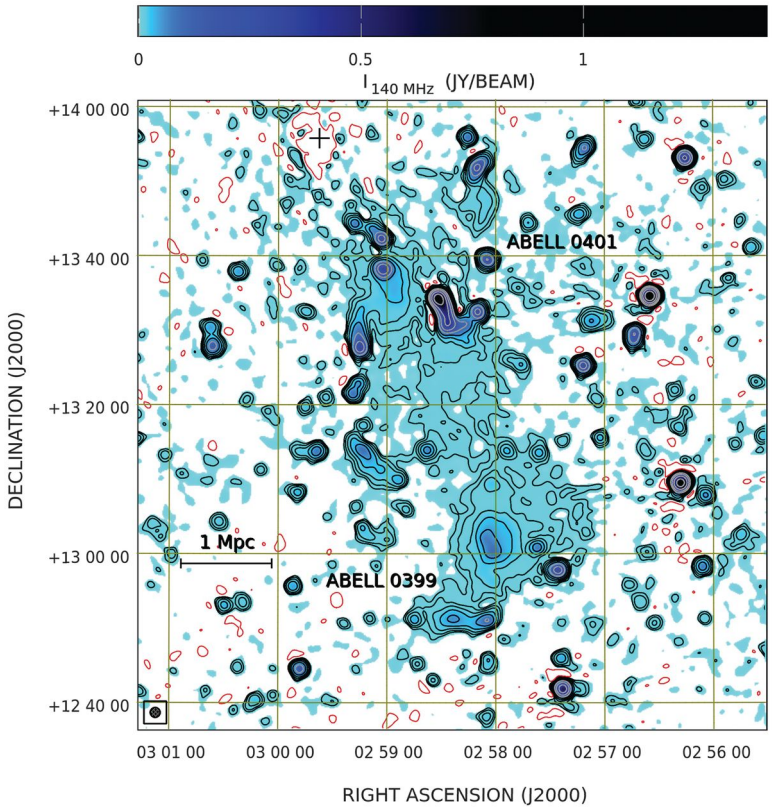

Figure 1.11: First image of diffuse radio emission in inter-cluster region (Govoni et al. 2019).

justify particles re-acceleration and magnetic fields amplification in such bridge region. Two models have been proposed (Govoni et al. 2019 and Brunetti and Vazza 2020) but are still under investigation.

In addition to this first discovery, also a second radio bridge has been discovered by Botteon et al. 2020 always using LoTSS data. This shows that more studies on those kind of data will provide new discoveries of such unexplained radio bridge, helping find out their origin and improving our knowledge of the largest scale structure in our Universe.

1.4 This thesis

In this thesis we study the polarized emission coming from the recently discovered *radio-bridge* region described before. In fact, simulation results (Govoni et al., 2019) show that a possible explanation for such inter-cluster emission, is the presence of a pre-exinsting population of relativistic electrons that are re-accelerate by weak ($M \sim 2-3$) shocks. This will lead to an emission with a high polarization fraction, about 70%, so, in principle, the emission of the bridge should be detected by studying the polarized radiation too.
Studying such polarized emission and exploiting simulation models, we aim to provide, for the first time, constraints on the magnetic field in a inter-cluster region.

2. Observations at low frequencies

2.1 Antenna fundamentals

Radio astronomy is the study of radio emission from celestial sources in a wide frequency range, between $\sim$ 10 MHz and $\sim$ 1 THz. These limits are posed by the atmosphere, in particular, at the high-frequency end of the radio window, rotational transitions of atmospheric molecules have energies $E = h\nu$ comparable with those of high radio-frequency photons, so vibrating molecules absorb most extraterrestrial radiation in this range. At long wavelengths ($\nu < 10$ MHz), the ionosphere is no longer transparent to radiation (Condon and Ransom, 2016). Already at $\nu < 1$ GHz, the ionosphere scatters incoming radio waves, requiring to develop specific corrections to observations.

At radio wavelengths, the incoming radiation can be treated as a superposition of electromagnetic waves, therefore, radio telescopes are essentially receiving antennas. An antenna is a passive device that converts electromagnetic radiation in space into electrical currents or vice versa, depending on whether it is used to receive or transmit. An important parameter of a receiving antenna is the *effective area*, which represents the antenna response to the incoming radiation. For unpolarized radiation, the total monochromatic flux density of a source, S_ν, the output power of the antenna at the same frequency, P_ν, and the effective area A_e are related through:

$$A_e = \frac{2P_\nu}{S_\nu}. \tag{2.1}$$

As the antenna response varies with direction, $A(\theta, \phi)$, one defines the *average collecting area* over a solid angle Ω as:

$$\langle A_e \rangle = \frac{1}{4\pi} \int_{4\pi} A_e \, d\Omega, \tag{2.2}$$

and it can be demonstrated (see Condon and Ransom, 2016) that:

$$\langle A_e \rangle = \frac{\lambda^2}{4\pi} \tag{2.3}$$

where λ is the observing wavelength.

Another important parameter defining a receiving antenna is the *beam solid angle*, Ω_A, which is the angle within the antenna receives the most of the incoming power. In the case of a lossless antenna, this quantity is defined as:

$$\Omega_A = \int_{4\pi} \frac{A_e(\theta, \phi)}{A_0} \, d\Omega, \tag{2.4}$$

where A_0 is the maximum effective collecting area. So, given the previous equations, one can write:

$$\Omega_A = \frac{\lambda^2}{A_0}. \tag{2.5}$$

Thus, the collective area defines the size of the beam solid angle, i.e. defines the "directionality" of an antenna.

2.2 Radio telescopes and interferometric arrays

Single dish radio telescopes use large reflectors to collect and focus power onto feeds, such as waveguide horns or dipoles backed by small reflectors, that are connected to receivers (Fig. 2.1). The most common reflector shape is a paraboloid of revolution because it can focus the plane wave from a distant point source onto a single focal point. However, depending on the observed frequency, other types of antenna can be used (e.g., LOFAR stations, see van Haarlem, M. P. et al. (2013)). As discussed

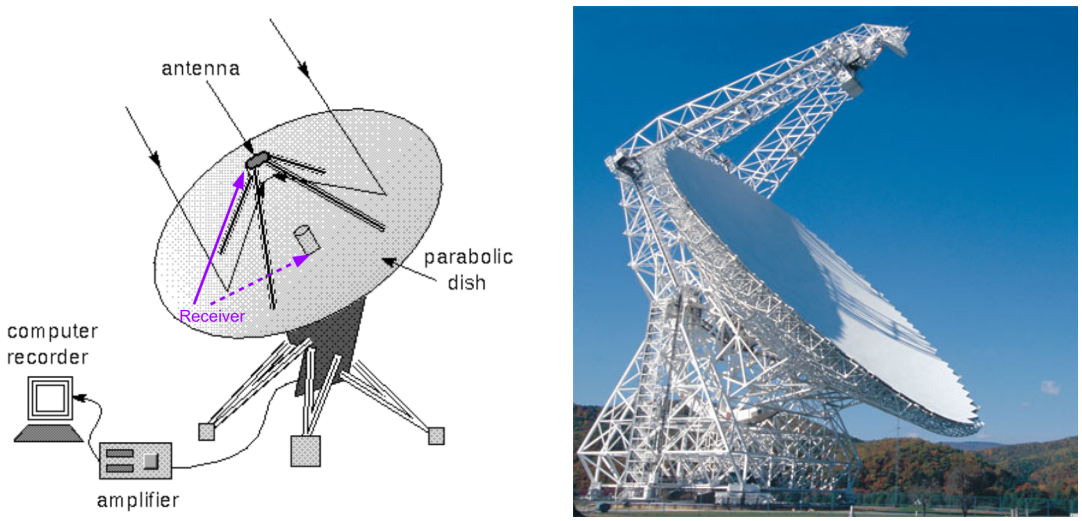

Figure 2.1: On the *left*, a single dish scheme where the basic components of a single-dish radio telescope are illustrated. On the *right*, the 100 m, single dish Green Bank Telescope.

before, the response of an antenna, in our case a of radio telescope, is not the same

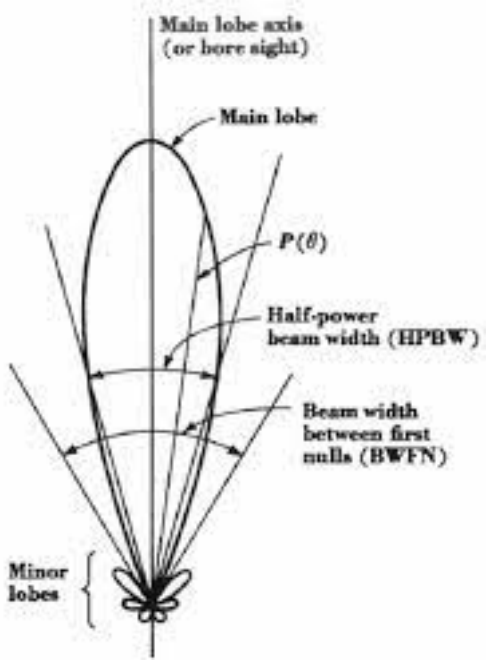

Figure 2.2: Example of antenna power-pattern. The higher lobe is called *main beam*, whether the smaller lobes are called *side lobes*.

in all direction. For a radio telescope, the variation of the instrumental response with the angle is called *power pattern*, and is represented by the diffraction figure of a point source (Fig 2.2). The most important feature of such pattern is the main beam, which angular size, called *half-power beam width* (HPBW), sets the resolution limit of the telescope:

$$\theta_{\mathrm{HPBW}} \sim \frac{\lambda}{D} \tag{2.6}$$

where D is the diameter of the telescope. The HPBW is sometimes called the resolving power of a telescope because two equal point sources separated by the HPBW are just resolved by the Rayleigh criterion (Condon and Ransom, 2016). Better angular resolutions need larger telescopes, however, it is prohibitive to construct single-dish radio telescope greater than ~ 100 m. A solution to this problem comes from interferometry.

Interferometric techniques have been developed to combine several single element telescopes into a multi-element array developed to overcome the limited angular resolution of single dishes.
The simplest radio interferometer is a pair of radio telescopes whose voltage outputs are correlated (multiplied and averaged), as shown in Fig 2.3. Even the most elaborate interferometers with $N \gg 2$ antennas, often called elements, can be treated as $\frac{N(N-1)}{2}$ independent two-element interferometers (Condon and Ransom, 2016). Figure 2.3 shows two identical dishes separated by the baseline vector $\overrightarrow{b}$ of length b. Both

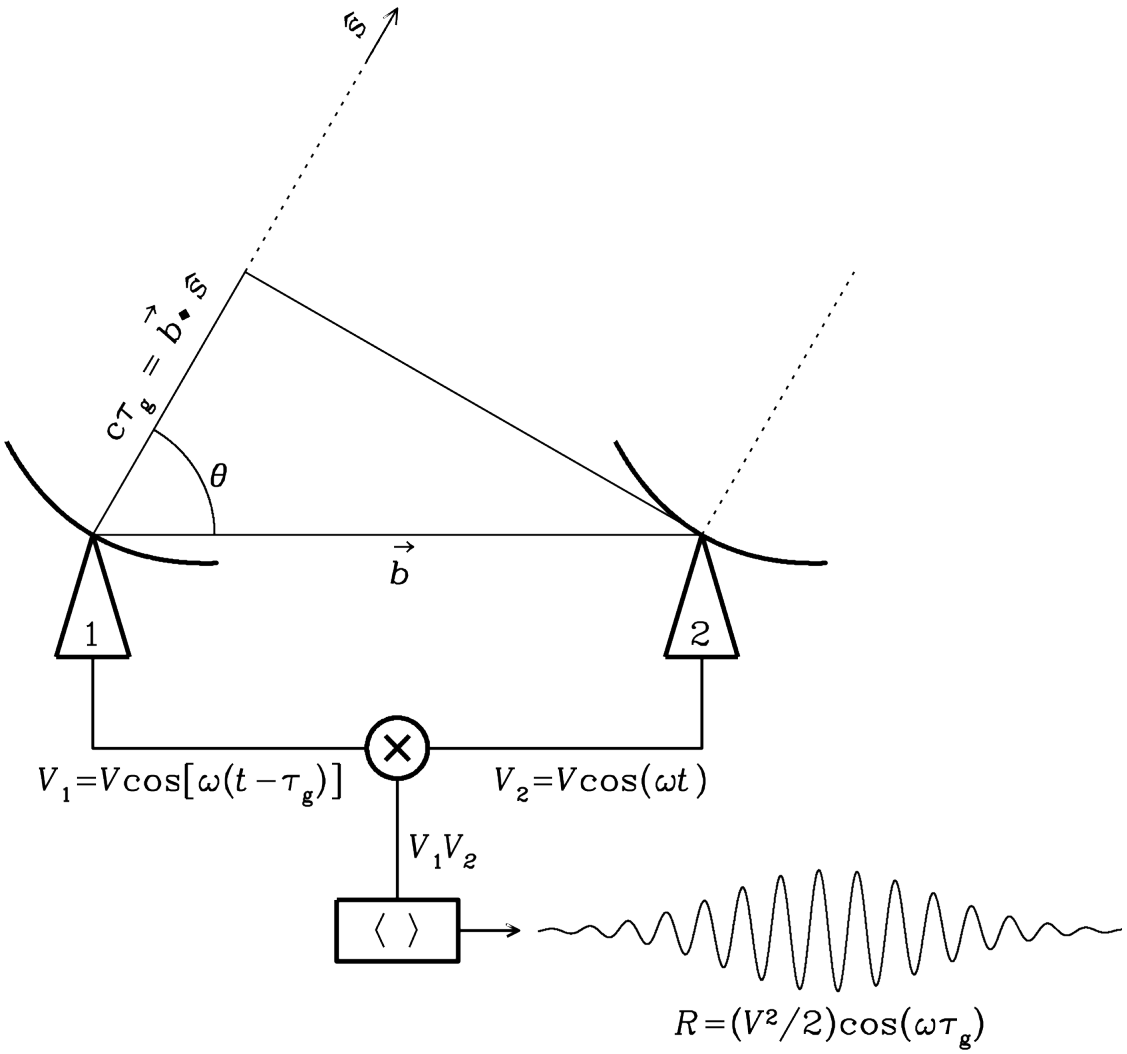

Figure 2.3: Scheme of the two-element interferometer: $\overrightarrow{b}$ is the baseline vector, V_1 and V_2 are the output voltages, V_1 is delayed by the geometric delay τ_g (from Condon and Ransom, 2016)

dishes are pointing in the same direction specified by the unit vector $\hat{s}$. Plane waves from a distant source reach the antenna 2 before 1, with a time delay that is connected to the *geometric delay*:

$$\tau_g = \frac{\overrightarrow{b} \cdot \hat{s}}{c} \tag{2.7}$$

where c is the light speed. The two output voltage of antenna 1 and 2, in the case of a quasi-monochromatic interferometer, are:

$$V_1 = V\cos[\omega(t-\tau_g)] \quad \text{and} \quad V_2 = V\cos(\omega t). \tag{2.8}$$

The two signals are subsequently passed to the *correlator* that multiplies and averages them in time, obtaining what is called *fringe pattern*. Combining signals described

both by cosine and sine functions (for further details see Condon and Ransom 2016) one obtains complex functions called *visibilities*, which are the Fourier transform of the sky brightness:

$$V_\nu(u,v,w) = \iint \frac{I_\nu(l,m)}{\sqrt{1-l^2-m^2}}\, e^{-2\pi i[ul+vm+w(\sqrt{1-l^2-m^2}-1)]}\, dl\, dm, \quad (2.9)$$

where (u,v,w) are the baseline coordinates $(b_x/\lambda,\, b_y/\lambda,\, b_z/\lambda)$ in the coordinate system of the array, I is the sky brightness and l, m are cosine sky coordinates. The w term is important only for wide fields of view (FoV). In fact, in the case of small FoV, the term $\sqrt{1-l^2-m^2}$ is approximately of unit size, making Eq. (2.9) an ordinary invertable two-dimensional Fourier transform. A common rule is that this is valid when:

$$\forall\ w,l,m : w\left(\sqrt{1-l^2-m^2}\right) \ll 1, \quad (2.10)$$

however, the small FoV assumption does not always hold, especially at low frequencies (FoV $\propto \lambda/D$), and more advanced techniques have been developed in order to perform a correct image analysis (Sec. 2.2.1). Visibilities obtained using the i-th and j-th, V^{ij}, antennas can be written as:

$$V^{ij} = A^{ij} e^{-i\phi^{ij}} \quad (2.11)$$

where A^{ij} and ϕ^{ij} are the visibility amplitude and phase, respectively. Observed visibility, V^{ij}_{obs}, are different from intrinsic visibility, V^{ij}_{trues}, i.e. the actual Fourier transform of the sky brightness distribution, as the incoming sky signals, are corrupted as they propagate through the telescope receiving system. Several factors can cause such distorsions: phase distorsions due to the atmosphere (both at low frequencies and high frequencies), amplitude variations due to the electronics, polarization leakages etc. The process of correction for these errors is called *calibration*. In particular, complex factors called *gains* are defined to account for these corruptions (See Eq. 2.12) and, once found their values (usually observing known sky sources), used to correct the registered signal:

$$V^{ij}_{obs} = G^{ij}\, V^{ij}_{trues} \quad (2.12)$$

where G^{ij} is the gain of that specific antenna pair.

Once visibilities are calibrated, $V_\nu(u,v,w)$, they can be Fourier-transformed to obtain a sky image. For simplicity, we will describe the basics of image processing under the assumption of a small FoV, so the relation between V_ν and I_ν becomes a simple 2D Fourier transform (for a more general treatment of the imaging process see Sec. 2.2.1).

Under this assumption, the sky brightness distribution can be written as:

$$I_\nu(l,m) = \iint V_\nu(u,v)\, e^{2\pi i(ul+vm)}\, dl\, dm. \tag{2.13}$$

$V_\nu(u,v)$ is a continuous function, but our measurements are discrete, and $V_\nu(u,v)$ are sampled only at certain points of the (u,v) plane. Therefore, what we really measure is the product between $V_\nu(u,v) and S_\nu(u,v)$, where $S_\nu(u,v)$ is the *sampling function*, which is equal to 1 where $V_\nu(u,v)$ is measured and 0 otherwise. The Fourier transform of the product between $V_\nu(u,v)$ and $S_\nu(u,v)$ is the *dirty image* I^D_ν:

$$I^D_\nu(l,m) = \iint S_\nu(u,v)\, V_\nu(u,v)\, e^{2\pi i(ul+vm)}\, dl\, dm. \tag{2.14}$$

The dirty image is the sky brightness convolved with the so called *dirty beam*, which is the point spread function (PSF) of the image, B_D (we omitted the dependences upon l, m and ν):

$$I^D = I * B^D \tag{2.15}$$

and the dirty beam is the Fourier transform of the sampling function:

$$B^D = \iint S(u,v)\, e^{2\pi i(ul+vm)}\, dl\, dm. \tag{2.16}$$

Therefore, in order to obtain the real sky brightness we have to *deconvolve* the dirty image from the instrumental response. There are different deconvolution algorithms, all based on the classical Högbom `CLEAN` algorithm (Högbom, 1974; Clark, 1980), which assumes that $I(l,m)$ can be considered as a collection of point sources. This algorithm searches throughout the dirty image for the brightest (I_{pxl}) pixel. Once found, it places a copy of the PSF at the pixel location, scaled to the pixel intensity multiplied by a factor $\gamma \sim 0.1 - 0.2$, called *loop gain*. Then, subtracts this quantity from the dirty image and saves the value $\gamma\, I_{pxl}$ into a clean component map, I^C. This process continues subtracting peaks until a fixed threshold of signal is reached, producing the *residual image*, I^R:

$$I^R = I^D - \gamma[I^C * B] \tag{2.17}$$

At the end of the process, the clean components are convolved with the *clean beam* (*restoring* process), which is a Gaussian 2D function having the Full Width at Half Maximum (FWHM) of the dirty beam. Finally the convolved clean components are summed with I^R to produce the final image.

2.2.1 WSClean

When the field of view is sufficiently large, the two-dimensional inversion approach is no longer accurate. There are various ways to account for the three-dimensional nature of the sky curvature, here we will describe the w–stacking algorithm implemented in the `WSClean v2.10.0` software package (Offringa et al., 2014). In this technique, Eq. (2.9) is re-written factorizing the w-dependent term from the others, obtaining:

$$V(u,v,w) = \iint \frac{I(l,m)e^{-2\pi iw\left(\sqrt{1-l^2-m^2}-1\right)}}{\sqrt{1-l^2-m^2}} e^{-2\pi i(ul+vm)}\, dl\, dm. \tag{2.18}$$

The FoV is divided in tiles of sufficiently small angular size so that the w term of each tile can be approximated as *constant*, i.e. the small FoV approximation holds for each tile. Therefore, inside each tile, Eq. (2.18) is an ordinary two-dimensional Fourier transform going from (u,v) space to (l,m) space (2D Fourier transform), and can be inverted to get:

$$\frac{I(l,m)}{\sqrt{1-l^2-m^2}} = e^{2\pi iw\left(\sqrt{1-l^2-m^2}-1\right)} \iint V(u,v,w)\, e^{2\pi i(ul+vm)}\, du\, dv. \tag{2.19}$$

Then, in order to reconstruct for sky signal from every direction (i.e. for the all possible w term), Eq. (2.19) is integrated (both sides) over w_{min} to w_{max}, the minimum and maximum value of w, resulting in:

$$\frac{I(l,m)(w_{max}-w_{min})}{\sqrt{1-l^2-m^2}} = \int_{w_{min}}^{w_{max}} dw\, e^{2\pi iw\left(\sqrt{1-l^2-m^2}-1\right)} \iint V(u,v,w)\, e^{2\pi i(ul+vm)}\, du\, dv. \tag{2.20}$$

The final step is to make the (u,v,w) parameters discrete, so that the integration over u and v can become an inverse Fourier transform and the integration over w becomes a sum.

These are the principles of the w-stacking technique, which calculates the 2D Fourier transform for a fixed w and then sums over all possible w values. With this technique, it is possible to quickly recover $I(l,m)$ and correct for large FoVs, i.e., overcoming the planar-sky assumption.

2.3 LOFAR overview

LOFAR (van Haarlem, M. P. et al., 2013), is a new and innovative radio telescope designed and constructed by ASTRON to open the lowest frequency radio regime for a broad range of astrophysical studies.
Capable of operating in the $10 - 240$ MHz frequency range (corresponding to wave-

Figure 2.4: Aerial photograph of the Superterp, the heart of the LOFAR core, from August 2011. The large circular island encompasses the six core stations that make up the Superterp. Three additional LOFAR core stations are visible in the upper right and lower left of the image. Each of these core stations includes 96 low-band antennas and two sub-stations of 24 high-band antenna tiles each (from van Haarlem, M. P. et al. 2013.

lengths of $30 - 1.2$ m), LOFAR consists of an interferometric array of dipole antenna stations distributed throughout the Netherlands and Europe. These stations have no moving parts and, due to the effectively all-sky coverage of the component dipoles, give LOFAR a large FoV. At station level, the signals from individual dipoles are combined digitally into a phased array. Electronic beam-forming techniques make the system agile and allow for rapid repointing of the telescope as well as the simultaneous observation of multiple, independent areas of the sky.

In the Netherlands, a total of 40 LOFAR stations have been deployed with an additional 8 international stations currently built throughout Europe (Figure 2.5). The densely sampled, 2-km-wide, core hosts 24 stations and is located ~ 30 km from ASTRON's head-quarters in Dwingeloo.

The fundamental receiving elements of LOFAR are two types of small antennas that, together, cover the $30 - 240$ MHz operating bandpass. The high-band antennas (HBAs) have been optimized to operate in the $110 - 250$ MHz range. In practice, the frequency range above 240 MHz is heavily contaminated by radio frequency interference

Figure 2.5: Current distribution of the International stations that have been built in Germany (5), France (1), Sweden (1) and the UK (1). Data from all international stations are routed through Amsterdam before transfer to a central processing in Groningen, NL. For the German stations, data are first routed through Jülich before transfer on to Amsterdam (from van Haarlem, M. P. et al., 2013).

(RFI) so operationally the band is limited to $110 - 240$ MHz.

At the lowest frequencies, instead, LOFAR utilizes the LBAs, which are designed to operate from the ionospheric cutoff of the "radio window" near 10 MHz, up to the onset of the commercial FM radio band at about 90 MHz. Due to the presence of strong RFI at the lowest frequencies and the proximity of the FM band at the upper end, this range is operationally limited to $30 - 80$ MHz by default.

In order to fully exploit this new wavelength regime with unprecedented resolution and sensitivity, LOFAR must meet several non-trivial technical challenges. For example, the meter-wave regime is prone to high levels of man-made interference. RFI excision requires high spectral and time resolution, and high dynamic range analog to digital (A/D) converters. Furthermore, for the typical sampling rate of 200 MHz, the long range data transport rates over the array are of order 150 Gbit/s requiring

dedicated fibre networks. Such large data transport rates naturally also imply data storage challenges. For example, typical interferometric imaging observations can easily produce 35 Tbyte/h of raw, correlated visibilities.

In addition to hardware and data transport challenges, LOFAR faces many technical challenges that are conceptual or algorithmic in nature. Low-frequency radio signals acquire are distorted by the ionosphere. For baselines longer than a few kilometers, the dynamic and non-isoplanatic nature of the ionosphere has a dramatic impact on the quality of the resulting scientific data. Correcting for these effects in LOFAR data has required improving existing calibration techniques that can simultaneously determine multi-directional station gain solutions to operate in the near, real-time regime. Likewise, LOFAR's huge FoV means the traditional interferometric assumption of a coplanar array is no longer valid. Consequently, highly optimized versions of imaging algorithms that recognize that the interferometric response and the sky brightness are no longer related by a simple $2D$ Fourier transform were required.

Scientifically, this new technology makes LOFAR a powerful and versatile instrument. With the longer European baselines in place, LOFAR can achieve sub-arcsecond angular resolution over most of its $30 - 240$ MHz nominal operating bandpass, limited primarily by atmospheric effects and scattering due to interplanetary scintillation. This resolution, when combined with the large FoV, makes LOFAR an excellent instrument for all-sky surveys.

2.4 The LoTSS survey

The LOFAR Surveys Key Science Project (PI:Röttgering) is conducting a three-tiered survey: Tier-1 includes LBA and HBA observations across the whole 2π steradians of the Northern sky; deeper Tier-2 and Tier-3 observations are focused on smaller areas with high-quality multi-wavelength datasets. The LOFAR Two-meter Sky Survey (LoTSS, Shimwell et al. 2017) is the first tier of observations. LoTSS is an ongoing survey at high resolution (6") and high sensitivity ($100\,\mu$Jy beam^{-1}, Fig. 2.6) of the northern sky (Fig. 2.7), using the HBAs in a $120 - 168$ MHz frequency range (with frequency resolution of ~ 97 kHz) and with an observing time of 8 h per pointing.

The main scientific motivations for LoTSS are to explore the formation and evolution of massive black holes, galaxies, clusters of galaxies and large-scale structure. More specifically, the survey was initially designed to detect: 100 radio galaxies at $z > 6$ and diffuse radio emission associated with the intra-cluster medium of 100 galaxy clusters at $z > 0.6$, along with up to 3×10^7 other radio sources (see Shimwell et al., 2017, and reference therein).

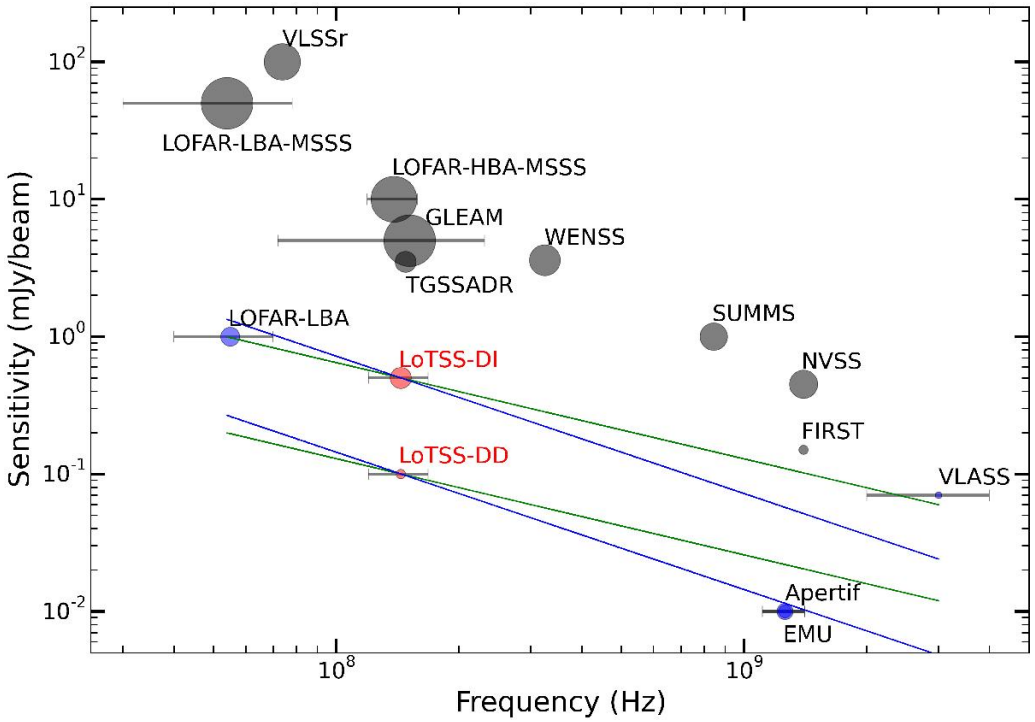

Figure 2.6: Summary of the sensitivity, frequency, and resolution of a selection of recent and planned large-area radio surveys. The size of the markers is proportional to the survey resolution. Grey, blue, and red markers show the ongoing/completed surveys, forthcoming surveys, and the LOFAR HBA surveys, respectively. The horizontal lines show the frequency coverage for surveys with large fractional bandwidths (> 0.2, see Shimwell et al., 2017).

Besides the primary objectives there are many other open questions that have further motivated LoTSS. The survey will significantly increase the known samples of young and old AGNs, including giant, dying and relic sources, allowing detailed studies of the physics of AGNs. It will also detect millions of AGN out to the highest redshifts (Wilman et al., 2008), including obscured AGNs, radiatively inefficient AGNs, and "radio-quiet" AGNs, and thus allow statistical studies of the evolution of the properties of different classes of AGNs over cosmic time (e.g., Best et al., 2014).

The sensitive images of the steep spectrum radio emission from local galaxy clusters and the expected detection of many of radio halos out to moderate redshifts will transform our knowledge of magnetic fields and particle acceleration mechanisms in clusters (e.g., Cassano et al., 2010).

Hundreds of thousands of star-forming galaxies will be detected up to $z \gtrsim 1$ (e.g., Hardcastle et al., 2016; Smith et al., 2014). They will trace the cosmic star formation rate density in a manner unaffected by the biases of dust obscuration or source confusion (e.g., Jarvis et al., 2015). The survey images, in combination with other datasets, will be used to measure cosmological parameters, including tests of alternative theories of

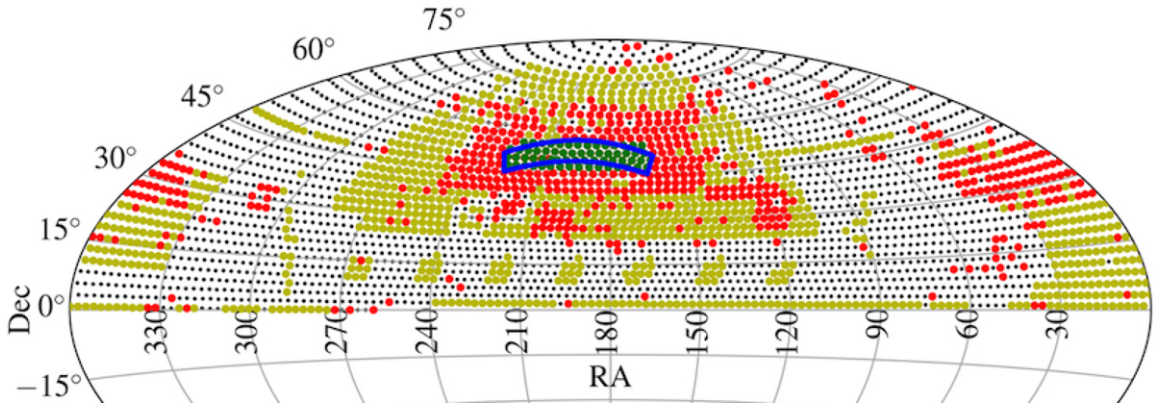

Figure 2.7: Status of the LoTSS observations as of May 2018. The green dots show the images that are presented in Shimwell et al. (2019). The red, yellow, and black dots show the observed pointings (but yet unpublished), pointings presently scheduled for observation between May 2018 and May 2020,and unobserved pointings, respectively. The HETDEX Spring Field region is outlined in blue.

gravity and using the integrated Sachs-Wolfe effect to constrain the nature of dark energy (e.g., Raccanelli et al., 2012; Jarvis et al., 2015; Schwarz et al., 2015).

Detailed maps of nearby galaxies will be used for studies of cosmic ray diffusion and magnetic fields. The shortest LOFAR baselines (less than 50 m) allow for degree scale emission to be accurately recovered, and the number of well-imaged supernova remnants and HII regions will be increased by an order of magnitude to forward studies of the interstellar medium and star formation. Large–scale Galactic synchrotron emission observations will provide new information about the strength and topology of the large-scale Galactic magnetic field (Iacobelli et al., 2013).

Finally, the survey datasets will be used for a range of other projects. As an example, the low-frequency polarization maps will be used by the Magnetism Key Science project to measure the Faraday spectra of sources (Beck et al., 2013).

3. RM synthesis technique

In this chapter we are going to describe the technique that will be used in this thesis to constrain the magnetic field in the A399–A401 bridge. This method, called *RM synthesis*, exploits the Faraday rotation effect caused by a magnetized medium over linearly polarized radiation. Therefore, here we first give a more extensive description of the Faraday rotation effect than the one provided in section 1.2.2 (following Govoni and Feretti, 2004; Brentjens and de Bruyn, 2005; O'Sullivan et al., 2012)) and then proceed with an overview of the RM synthesis (from Brentjens and de Bruyn, 2005).

3.1 Polarization recap

Synchrotron radiation is linearly polarized (Sec. 1.2.1). The polarization of an electromagnetic wave is generally described in terms of the Stokes parameters I, Q, U and V, which are parameters of a reference system that can represent the orientation of the wave electric field. We define (see, e.g. O'Sullivan et al., 2012) the complex linear polarization P as:

$$P = pIe^{2i\Psi} = Q + iU \tag{3.1}$$

where Ψ is the observed polarization angle. A graphic view of such definition can bee seen in Fig. 3.1. The measured magnitude of the degree of linear ($V = 0$) polarization, p, is

$$p = \frac{\sqrt{Q^2 + U^2}}{I} \tag{3.2}$$

and the polarization angle Ψ is

$$\Psi = \frac{1}{2} \arctan \frac{U}{Q}. \tag{3.3}$$

3.2 Faraday rotation effect

As previously explained in Sec. 1.2.2, due to the birefringence of a magneto-ionic medium, the polarization angle of a linearly polarized radiation that propagates through

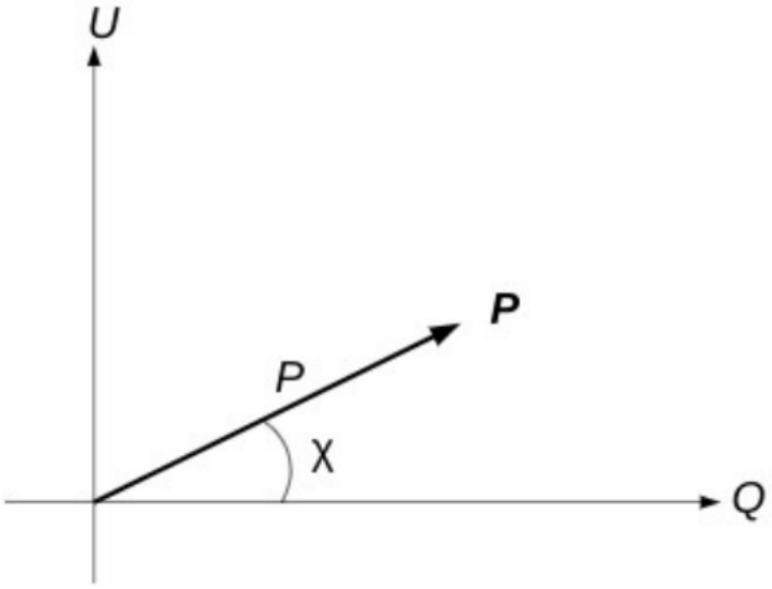

Figure 3.1: Scheme of the polarization vector **P** in the (Q, U) plane, highlights its module and the polarization angle.

the plasma is rotated as a function of frequency (Brentjens and de Bruyn, 2005). This effect is called Faraday rotation, and it can be better understood if one thinks of a linearly polarized radiation as the combination of two circularly polarized waves, one left and one right-handed. These two waves propagate with different velocities in the magneto-ionic medium. In fact, according to the dispersion relation for a wave with angular frequency ω ($\omega = 2\pi\nu$), the refracting index n of a magnetized dielectric medium can take two possible values (Govoni and Feretti, 2004):

$$n_{L,R} = \left(1 - \frac{\omega_p^2}{\omega^2 \pm \omega\Omega_e}\right)^{1/2} \tag{3.4}$$

where L, R stand for *left* and *right* respectively, $\omega_p = \left(\frac{4\pi n_e e^2}{m_e}\right)^{1/2}$ is the plasma frequency and $\Omega_e = \frac{eB}{m_e c}$ is the cyclotron frequency.
In the limit $\omega \gg \Omega_e$, Eq. 3.4 can be approximated as:

$$n_{L,R} \approx 1 - \frac{1}{2}\frac{\omega_p^2}{(\omega^2 \pm \omega\Omega_e)} \tag{3.5}$$

thus the time difference Δt between the two opposite handed waves to travel a path length dl results:

$$\Delta t \approx \frac{\omega_p^2 \Omega_e dl}{c\omega^3} = \frac{4\pi e^3}{\omega^3 m_e^2 c^2} n_e \, B \, dl \tag{3.6}$$

and the phase difference between two signals is $\Delta\theta = \omega\Delta t$.
Decomposing the initial linearly polarized radiation in two circular components shows that these two propagate differently in the magnetized medium. In fact, different refracting indexes mean different propagation velocities for the left and right circularly polarized waves. This causes the two waves not to be in the same configuration as for the initial radiation. Therefore, after the transition across the medium, the two circular components are out of phase with those of the original radiation. The global effect is a change in the polarization angle of the linearly polarized radiation when crosses a magnetized plasma (Fig. 3.2).
In particular, travelling along a cluster path length L, the intrinsic polarization angle Ψ_0 will be rotated by an angle $\Delta\Psi = \frac{1}{2}\Delta\theta$, resulting in an observed polarization angle Ψ_{Obs} of:

$$\Psi_{Obs}(\lambda) = \Psi_0 + \Delta\Psi = \Psi_0 + \frac{e^3\lambda^2}{2\pi m_e^2 c^4}\int_0^L n_e(l)\, B_\parallel(l)\, dl \tag{3.7}$$

where $B_\parallel$ is the component of the magnetic field along the line of sight. The observed

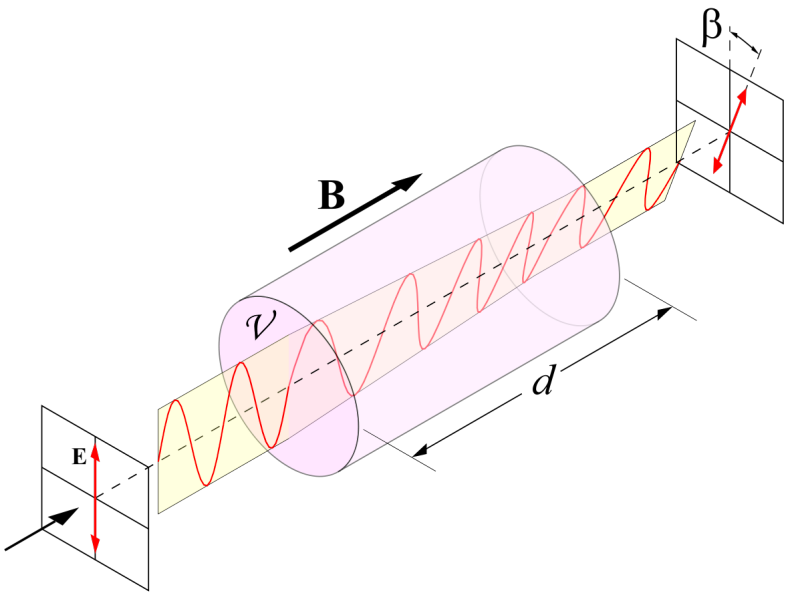

Figure 3.2: Scheme of how the Faraday rotation causes changes in the polarization angle of a radiation (credit Wikipedia).

angle Ψ_{Obs} is usually written in terms of the Faraday depth ϕ:

$$\Psi_{Obs}(\lambda) = \Psi_0 + \lambda^2\phi \tag{3.8}$$

where:

$$\phi = \frac{e^2}{2\pi m_e^2 c^4}\int_0^L n_e(l)\, B_\parallel\, dl \tag{3.9}$$

Or, equivalently (see Brentjens and de Bruyn, 2005):

$$\phi \simeq 0.81 \int_0^L n_e \, \boldsymbol{B} \cdot d\boldsymbol{l} \left[\frac{\mathrm{rad}}{\mathrm{m}^2}\right] \tag{3.10}$$

with n_e electron density in cm^{-3}, $\mathbf{B}$ the magnetic field in μG and d$\mathbf{l}$ is the infinitesimal path length in parsecs. By convention, a positive Faraday depth implies a magnetic field pointing toward the observer.
We note that, Eq. 3.8 is valid only in the simplest possible scenario, where there is a single background source along the line of sight and with a Faraday rotation due only to a foreground magneto-ionic medium.
Another quantity related to the Faraday rotation effect is the *Rotation Measure* (RM). Following Brentjens and de Bruyn (2005) and Burn (1966) we explicitly distinguish ϕ and RM. The Faraday depth, ϕ, is defined as indicated by Eq. 3.10, while the rotation measure is defined as the slope of a polarization angle Ψ versus λ^2:

$$RM = \frac{\mathrm{d}\Psi(\lambda^2)}{\mathrm{d}\lambda^2} \tag{3.11}$$

Therefore, only in the case of *Faraday thin source*, i.e. with a linear $\Psi(\lambda^2)$ behaviour (Eq. 3.8), the Faraday depth is equal to the rotation measure and we obtain:

$$\Psi_{Obs}(\lambda) = \Psi_0 + RM\lambda^2 \tag{3.12}$$

Throughout this thesis, we are only going to consider Faraday thin sources, therefore, in Chapter 4 we will use interchangeably the terms Faraday depth and rotation measure, and their respective symbols (ϕ and RM).

3.2.1 Depolarization mechanisms

Given Eq. (3.1), in the simplest possible case the complex polarized intensity of a synchrotron radiation affected by Faraday rotation is:

$$P(\lambda^2) = p_0 \, e^{2i(\Psi_0 + RM\lambda^2)} \tag{3.13}$$

where p_0 is the intrinsic degree of polarization of the synchrotron emission, Ψ_0 is the intrinsic polarization angle at the source of the emission and RM describes the Faraday rotation caused by the foreground magneto-ionic medium. If this scenario occurs, but one observes different fraction of polarized emission at different wavelengths, then there must be something else that causes such change. In particular, if the polarized emission decrease with increasing wavelength, an additional process that generates *depolarization* is at play.

With depolarization we refer to a process that reduces the degree of polarization of a source. Two typical cases of depolarization are beam and bandwidth depolarization. The beam depolarization occurs when the polarization angle changes significantly on scales much smaller than the beam size. When this occur, Stokes Q and U parameters change their sign and their integral over the beam area is smaller compared to the case of uniform polarization angles.

Bandwidth depolarization occurs when the polarization angle changes significantly over the observing band. Similarly to beam depolarization, if the polarization angle changes significantly across the observing band (as it happens for high RM sources, for instance), the polarized intensity integrated across the bandwidth is smaller compared to the case where no rotation occurs. Such problem is largely mitigated by the RM synthesis technique (Sec. 3.3.1), as the complex polarization of a source is added coherently across the bandwidth.

In addition to these two effects, other depolarization events have been found in different sources. A complete treatment of more complex models of depolarization can be found in Sokoloff et al. (1998), here we will follow the overview of such models provided in O'Sullivan et al. (2012).

There are three common depolarization mechanisms:

- **Differential Faraday rotation**

  This effect occurs when the emitting and rotating regions are co-spatial and filled with a uniform magnetic field. The polarization plane of the emission at the far side of the region undergoes a different amount of Faraday rotation compared to the polarized emission coming from the near side, causing depolarization when summed over the entire region. For a uniform slab of emitting and rotating medium we have:

  $$P = p_0 \frac{\sin \phi\lambda^2}{\phi\lambda^2} e^{2i(\Psi_0 + \frac{1}{2}\phi\lambda^2)}. \tag{3.14}$$

  Eq. (3.14) shows depolarization follows a synch function ($\frac{\sin \phi\lambda^2}{\phi\lambda^2}$), i.e. increasing a longer wavelengths. It should also be noted that, operationally, the imaginary part that quantifies the Faraday rotation remains the same as in Eq. (3.1).

- **Internal Faraday dispersion**

  In this case emitting and rotating regions are filled with a turbulent magnetic field. Depolarization occurs because the plane of polarization experiences a random walk through the region. For identical distributions of all the constituents of the magneto-ionic medium along the line of sight, it can be described by:

  $$P = p_0 \, e^{2i\Psi_0} \left(\frac{1 - e^{2i\phi\lambda^2 - 2\zeta_{RM}^2 \lambda^4}}{2\zeta_{RM}^2 \lambda^4 - 2i\phi\lambda^2} \right) \tag{3.15}$$

where ζ_{RM} is the internal Faraday dispersion of the random field. Unlike Eq. (3.14), this time there is not a specific real term which causes the depolarization. Indeed, there is a combination of different terms, complex and real, that together reduces the module of the complex polarization vector $|P|$. To be noticed that, also in this case, there is still a wavelength dependence.

- **External Faraday dispersion/beam depolarization**

  This last effect occurs in a purely external, non-emitting Faraday screen. In the case of turbulent fields, depolarization occurs when several turbulent regions can not be resolved by the observations. On the other hand, for a regular magnetic field, any variation in the strength or direction of the field within the observing beam will lead to depolarization. Both effects can be described by:

$$P = p_0 \, e^{-2\sigma_{RM}^2 \lambda^4} \, e^{2i(\Psi_0 + RM\lambda^2)} \tag{3.16}$$

  where σ_{RM} is the dispersion around the mean RM across the source on the sky. As for the first case, in Eq. (3.16) the imaginary and real terms are separated. The imaginary term parameterizes the rotation of the polarization vector causes by the Faraday rotation effect, without modify the module of P. The real part, instead, is the one that defines the amount of depolarization of P, which becomes stronger at higher values of σ_{RM} and longer wavelengths.

Finally, there is also a fourth possibility. In fact, multiple interfering RM components can cause a change in the degree of polarization. With multiple RM components one refers to the fact that emission from a source can be Faraday-rotated by multiple Faraday screens (i.e. magnetized plasma) with different RM values. These structures can be cospatial with the source (e.g. unresolved inner regions of a radiosource, see O'Sullivan et al. 2012), but also they can be foreground regions, e.g. galactic or intergalactic. Regarding the change in the polarization degree, multiple RM components can be both increase or decrease the amount polarized signal of a source and, in certain cases, can also changes from the linear $\Psi(\lambda^2)$ behaviour. More information about this effect can be found in O'Sullivan et al. (2012).

3.3 RM synthesis

The RM synthesis technique allows to find the correct Faraday depth, ϕ (Eq. 3.10), for a rotating medium and study the polarized emission of a source. As already explained in Sec. 1.2.2, once determined the value of ϕ, one can derive information about the magnetic field and particles distribution of the medium crossed by linearly polarized radiation.

As introduced in Sec. 3.2.1, the simplest case for the Faraday rotation is the one with a single source along the line of sight and with an external rotating medium. In such case the observed polarization vector can be modeled by Eq. (3.13), and the corresponding polarization angle is given by Eq. (3.12):

$$\Psi_{Obs}(\lambda) = \Psi_0 + RM\lambda^2.$$

In order to recover for the RM value, one first plots the observed polarization angles as a function of wavelength squared. Then, fit the plotted points with a straight line whose slope is the selected RM and find the best fit model.
However, this model suffers from the so called $n\pi$ ambiguities problem (see Brentjens and de Bruyn, 2005) and is usually oversimplified. In general, especially in clusters, the magnetic field could not be homogeneous or the rotating and the emitting medium can be mixed. Moreover, one can observe more than one source along the line of sight and also complex Faraday source (i.e. which shows multiple ϕ components and then can not be described by only one ϕ) are present.

3.3.1 RM technique

The RM synthesis developed by Brentjens and de Bruyn (2005) is a more complete method to analyze the Faraday rotation on a polarized source. They extended the rotation measure work of Burn (1966) to the cases of limited sampling of λ^2 space. They have found a Fourier transform connection between the observed polarization vector as a function of the wavelength squared, $P(\lambda^2)$, and the same vector as a function of the Faraday depth, $F(\phi)$, called *Faraday dispersion function* (FDF) or *Faraday spectrum* (Burn 1966).
Burn (1966) has shown that:

$$P(\lambda^2) = \int_{-\infty}^{+\infty} F(\phi)\, e^{2i\phi\lambda^2} d\phi \tag{3.17}$$

which is very similar to a Fourier transform. A fundamental difference is that $P(\lambda^2)$ only has a physical meaning for $\lambda^2 > 0$. Because P cannot be measured at $\lambda^2 < 0$, equation 3.17 is only invertible if one makes some assumptions on the value of P at $\lambda^2 < 0$ based on its value at $\lambda^2 \geq 0$ (Burn 1966). Brentjens and de Bruyn (2005) have generalized Eq. (3.17) introducing the weight function $W(\lambda^2)$, also called *sampling function*. It is nonzero at all λ^2 points where measurements are taken and zero elsewhere. Obviously, $W(\lambda^2) = 0$ for $\lambda^2 < 0$ because the lack of measurements

there. Hence, they define the observed polarized flux density as:

$$\tilde{P}(\lambda^2) = W(\lambda^2)P(\lambda^2) \tag{3.18}$$

which substituted in Eq. 3.17 gives:

$$\tilde{P}(\lambda^2) = W(\lambda^2)\int_{-\infty}^{+\infty} F(\phi)\, e^{2i\phi\lambda^2} d\phi \tag{3.19}$$

Once defined $\widetilde{P}$ in this way, they also defined other two quantities:

$$\tilde{F}(\phi) = F(\phi) \otimes R(\phi) \tag{3.20}$$

$$R(\phi) = K\int_{-\infty}^{+\infty} W(\lambda^2)\, e^{-2i\phi\lambda^2} d\lambda^2 \tag{3.21}$$

where $\otimes$ denotes convolution, $R(\phi)$ is called Rotation Measure Transfer Function (RMTF) and K is:

$$K = \left(\int_{-\infty}^{+\infty} W(\lambda^2)\, d\lambda^2\right)^{-1} \tag{3.22}$$

With all these new quantities, they were able to find a relation between $\tilde{F}(\phi)$ and $\tilde{P}(\phi)$:

$$\tilde{F}(\phi) = K\int_{-\infty}^{+\infty} \tilde{P}(\lambda^2)\, e^{-2i\phi\lambda^2} d\lambda^2 \tag{3.23}$$

that, in a more general way, can be written as:

$$\tilde{F}(\phi) = K\int_{-\infty}^{+\infty} \tilde{P}(\lambda^2)\, e^{-2i\phi(\lambda^2-\lambda_0^2)} d\lambda^2 \tag{3.24}$$

$$R(\phi) = K\int_{-\infty}^{+\infty} W(\lambda^2)\, e^{-2i\phi(\lambda^2-\lambda_0^2)} d\lambda^2 \tag{3.25}$$

where λ_0 is the wavelength to which all polarization vectors are derotated.
Equations 3.24 and 3.19 form a Fourier pair that enables to transform polarization information from λ^2 space to ϕ space and back. Note that $R(\phi)$ is a complex valued function. The real part corresponds to the response of the transform parallel to the (Q, U) vector at $\lambda = \lambda_0$ and the imaginary part corresponds to the response orthogonal to it.
$\tilde{F}(\phi)$ is an approximate reconstruction of $F(\phi)$. More accurately, it is $F(\phi)$ convolved with $R(\phi)$ after Fourier filtering by the weight function $W(\lambda^2)$. The quality of the reconstruction depends mainly on the weight function $W(\lambda^2)$. The higher is the number of λ^2 measurements, for a fixed bandwidth, the lower are the sidelobes of $R(\phi)$. Instead, the wider is the range of measured λ^2 the higher is the resolution in ϕ space.

Hence, a complete and wide range of λ^2 measurements leads to a collimated RMTF and a fine sample in ϕ space, allowing a better reconstruction of $F(\phi)$ (Brentjens and de Bruyn, 2005).
This is pretty similar to what happens when performing image sysnthesis with an array of radio telescopes. In that case, the larger is the baseline the finer/higher will be the resolution , while the higher is the number of measurements the lower will be the sidelobes on the dirty beam. In particular, the RTMF and the dirty beam of an array are conceptually the equivalent, in fact both define the quality and the resolution of the finale image.

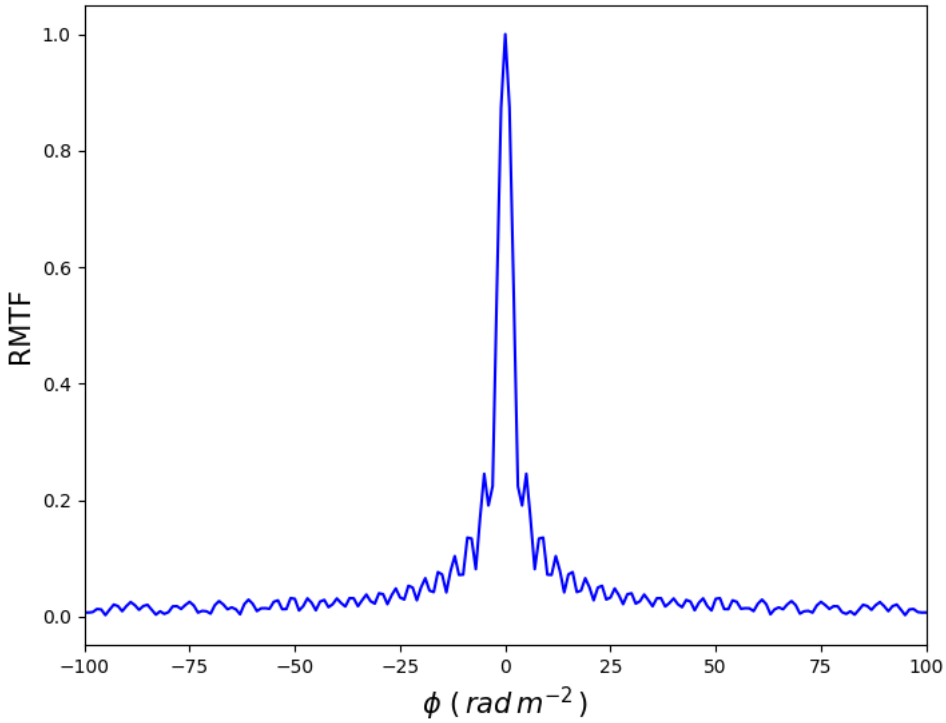

Figure 3.3: RMTF obtained from our analysis, in a ϕ range between ± 100 and with a ϕ_{max} (Eq 3.31) of ~ 45.

In practice, integrals are replaces by sum, because of the finite number of λ^2 measurements (just like a radio interferometer discretely samples the uv-space) . Then, if the product between the Faraday depth and the squared channel width ($\delta\,\lambda^2$) is small,

$\phi\,\delta\lambda^2 \ll 1$, for every channel, the previous quantities become:

$$\tilde{F}(\phi) \approx K \sum_{i=1}^{N} \tilde{P}_i\, e^{-2i\phi(\lambda_i^2-\lambda_0^2)} \tag{3.26}$$

$$R(\phi) \approx K \sum_{i=1}^{N} W_i\, e^{-2i\phi(\lambda_i^2-\lambda_0^2)} \tag{3.27}$$

$$K = \left(\sum_{i}^{N} W_i\right)^{-1} \tag{3.28}$$

In these equations, $\tilde{P}_i = W_i P_i(\lambda_i^2)$, $W_i = W(\lambda_i^2)$ and N is the total channels number. In any case, all the considerations on the final image quality explained before are still valid.

Three main parameters are involved in the RM synthesis process: the channel width $\delta\lambda^2$, the width of the λ^2 distribution $\Delta\lambda^2$ and the shortest wavelength squared λ^2_{min}. These parameters determine respectively the maximum observable Faraday depth, the resolution in ϕ space, and the largest scale in ϕ space to which the observations are sensitive (Brentjens and de Bruyn, 2005). An estimate for the FWHM of the main peak of the RMTF is given by:

$$\delta\phi \approx \frac{2\sqrt{3}}{\Delta\lambda^2} \tag{3.29}$$

instead, the scale in ϕ space to which the sensitivity drops to 50% is:

$$\text{max-scale} \approx \frac{\pi}{\lambda^2_{min}} \tag{3.30}$$

and , finally, the maximum Faraday to which an observation has more than 50% sensitivity is:

$$\|\phi_{max}\| \approx \frac{\sqrt{3}}{\delta\lambda^2} \tag{3.31}$$

From these equations one can derive which are the limits for the RM synthesis, given a specific set of data.

Eq. 3.29 tells us that wider bandwidth corresponds to higher resolution in the Faraday space. This is one of the reason why LoTSS data are optimal for our studies, indeed they cover a sufficiently broad frequency range to perform a proper sampling of the Faraday spectrum.

Another important information for the RM synthesis comes from Eq (3.31). It essentially defines what is the maximum detectable Faraday depth by *RM* studies. Such quantity depends on the minimum channel width of the data (actually the minimum width of the channel squared), and one can see that the smaller is the channel width the bigger is ϕ_{max}. Once again, LoTSS data are optimal for this kind of studies because

have a high spectral resolution over the full bandwidth (see Sec. 2.4).
It should be noted that LoTSS data have a uniform sampling in frequency but Eq. (3.31) refers to the sampling in wavelength. Because of the fact that the conversion from frequency to wavelength is not "rigid", the $\delta\lambda^2$ varies based on which frequency range one is considering. Because of that, the maximum observable Faraday depth is reported using the minimum available frequency of the observation since the resulting ϕ_{max} is the smallest. Therefore, if one is concerned about large Faraday depth, would be interested in using high frequency data, and viceversa for low ϕ studies.

Once performed the RM synthesis and obtained the FDF convolved for the RMTF, $\tilde{F}(\phi)$, one knows the polarized intensity of the studied source as a function of the Faraday depth ϕ. In order to identify the correct ϕ of the medium which is causing the depolarization, peak (or peaks) in such Faraday spectrum should be found. In the simple case of a depolarization from an homogeneous medium, a single in peak in the Faraday spectrum would appear, indicating both the amount of polarized intensity of the observed source and the corresponding Faraday depth, ϕ_{peak}.

3.3.2 Polarization analysis

RMTF improvement

One of the main goals in the RM synthesis process is the improvement of the reconstructed Faraday spectrum, $\tilde{F}(\phi)$. Have a high quality Faraday spectrum means have a good knowledge of the source Faraday structure, which results in stronger constraints of its physical properties.
An important element in the final spectrum quality is the RMTF, which essentially defines the ϕ-resolution in the Faraday space. As discussed in the previous section, the goodness of such function depends on the number of measured wavelengths and on the total wavelengths range, that establishes the FWHM. Apart from these two quantities, Brentjens and de Bruyn (2005) have found that a better response in the RMTF peak can be obtained using as λ_0 the weighted average of the observed λ^2

$$\lambda_0^2 = \frac{\int_{\infty}^{\infty} W(\lambda^2)\lambda^2 d\lambda^2}{\int_{-\infty}^{+\infty} W(\lambda^2) d\lambda^2} \tag{3.32}$$

Such improvement can be seen in Fig. 3.4a and 3.4b. A drawback of having $\lambda_0^2 \neq 0$ is that, to recover information on the orientation of the electric field direction at the source plane (i.e. the intrinsic polarization angle), the polarization angle that is derived still needs to be transformed to a polarization angle at $\lambda_0^2 = 0$. Then one should perform the multiplication of the reconstructed $\tilde{F}(\phi) = \tilde{Q}(\phi) + i\tilde{U}(\phi)$ by $e^{-2i\phi\lambda_0}$.

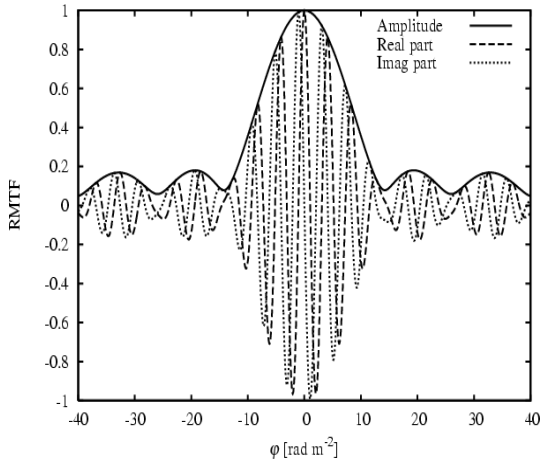

(a) Example of a RMTF where all (Q, U) vectors have been derotated to $\lambda_0^2 = 0$ from Brentjens and de Bruyn (2005). They used 126 channels in the dataset.

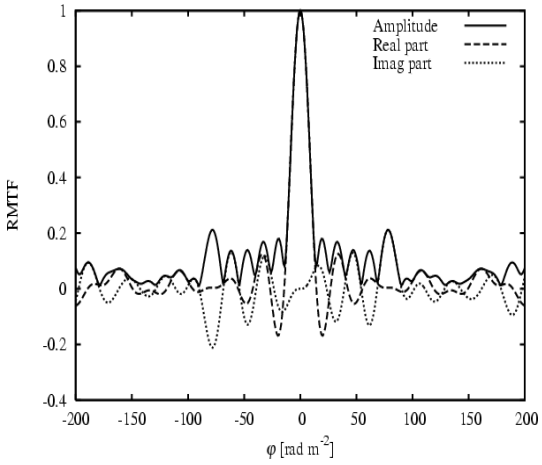

(b) RMTF of the same dataset as described in the figure beside. This time, however, all **P** vectors have been derotated to the average λ^2.

For the purpose of this thesis, which is to recover for ϕ, this wavelengths shift does not affect the final result. Therefore, we will not perform such further derotation.

Intrinsic polarization

When derotated the function $\tilde{F}(\phi)$ as explained before, one can derive the intrinsic polarization angle of the emitted radiation (i.e. the polarization at the source). In order to do this, one has to find the ϕ at the peak in the Faraday spectrum, ϕ_{peak}, typically fitting the whole peak with a Gaussian. Then, it is possible to recover both $\tilde{Q}(\phi_{peak})$ and $\tilde{U}(\phi_{peak})$ values from of the RM synthesis outputs and using them to derive the intrinsic polarization angle through

$$\Psi_0 = \frac{1}{2} \arctan\left(\frac{\tilde{U}(\phi_{peak})}{\tilde{Q}(\phi_{peak}}\right) \tag{3.33}$$

Consequently, the magnetic field orientation can be simply obtained by rotating the polarization angle of 90°.
This can be also a way to add information to the magnetic field orientation of the source.

RM clean

One may have noticed that we kept the $\sim$ symbol when talking about the Faraday spectrum, and its components (Q, U), derived from the RM synthesis. This is because the output function, $\tilde{F}(\phi)$, is still the convolution between the "real" $F(\phi)$ and the RMTF.

In order to recover the $F(\phi)$ spectrum one has to deconvolve the $F(\phi)$ function. This technique was introduced by Heald et al. (2009) on Spitzer Infrared Nearby Galaxies Survey (SINGS) obtained with the Westerbork telescope. They used a variation of the Högbom `CLEAN`, where the deconvolution is complex-valued and operates along the ϕ dimension, which is the third axis of the $Q(\phi)$ and $U(\phi)$ cubes produced by the RM synthesis technique. The technique, called `RM-CLEAN`, iteratively subtracts scaled versions of the RMSF from the reconstructed Faraday dispersion function until the noise floor is reached, after which a smoothed representation of the "CLEAN model" is used as the approximate true Faraday dispersion function.
For instance, Heald et al. (2009) used as noise the noise in the individual $Q(\phi)$ and $U(\phi)$ maps and a gain factor of 0.1. It should be noted that the only benefit of this technique is the reduction of the sidelobe pattern, Fig.3.5. No improvement were obtained in the ϕ resolution, as it depends by the overall bandwidth range. For further details see Heald et al. (2009).

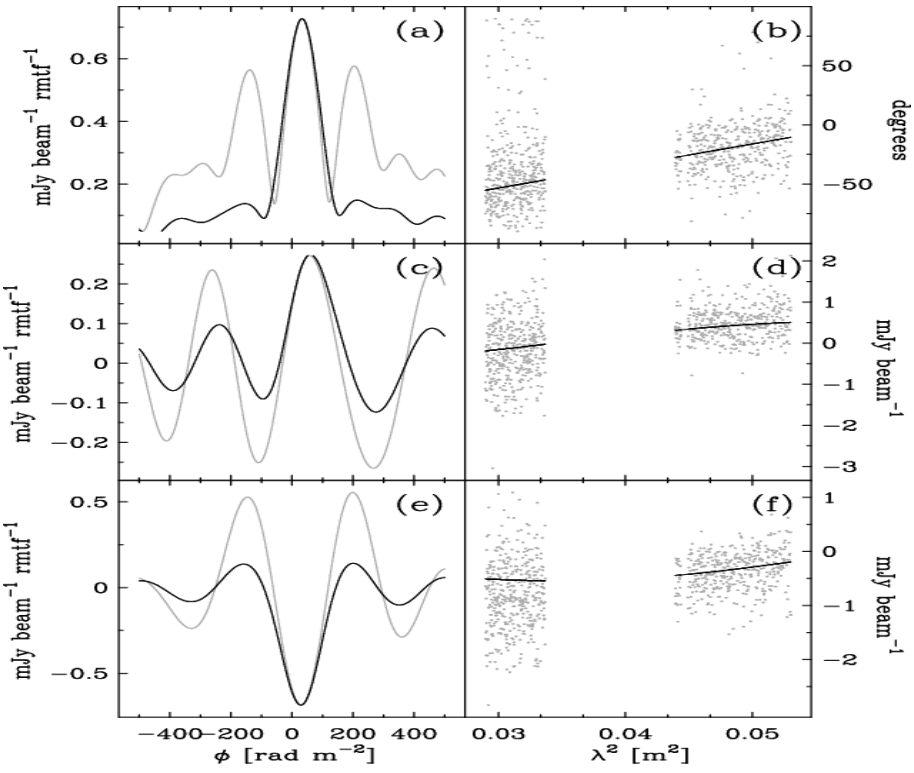

Figure 3.5: Deconvolved Faraday spectrum, using the `RM-CLEAN` technique, of a bright point source. *Top: P, middle: Q, bottom: U.* Gray lines are the dirty spectra; black lines are the cleaned spectra. It can be see that there is a significant reduction of the sidelobe structure. From Heald et al. (2009).

4. The bridge between A399–A401

We investigated the radio polarized emission coming from the inter-cluster region located between clusters Abell 399 and Abell 401. Informations about these two objects are summarized in Tab. 4.1.

Object	z	RA	DEC	Mass ($10^{14} M_{\odot}$)	kT$_{ICM}$ (keV)
Abell 0399	0.0718	$02^{h}\ 57^{m}\ 56^{s}$	$+13°\ 00'\ 59"$	5.7	≈ 7
Abell 0401	0.0737	$02^{h}\ 58^{m}\ 57^{s}$	$+13°\ 34'\ 46"$	9.3	≈ 8

Table 4.1: Summary of the main characteristics of the A399–A401 pair.

At radio wavelengths, both clusters show a radio halo, and, as explained in Govoni et al. (2019), X-ray and optical observations indicate that the system is still in the initial phase of a merger. Observations of the Sunyaev-Zeldovich (SZ) effect confirmed the presence of a connecting bridge between the two clusters, with density of $(4.3 \pm 0.7) \times 10^{-4}$ cm^{-3} (Bonjean et al., 2018), which shows also filamentary X-ray emission (Akamatsu et al., 2017).

This target was studied by Govoni et al. (2019), who detected many radio sources in that region.
They revealed the presence of radio halos in the two clusters. Both halos are round and regular in shape and extending, at 140 MHz, up to 970 kpc for Abell 0399 and 800 kpc for Abell 0401.
They also found a number of radio galaxies associated with the clusters, both of compact and extended shape. As an example, Fig 4.1 shows that Abell 0401 is among several point like and distorted radio galaxies. Moreover, near the edge of Abell 0401, in the further north-west region from the cluster center, another radio source shows a long tail to the south. All these radio sources may supply relativistic electrons to the cluster environment, but no clear connection has been found.
As mentioned in Sec 1.3.2, the main discovery of that study is the detection of a radio emission connecting the two radio halos. This discovery provided the first evidence of relativistic electrons and magnetic fields on Mpc scales in the inter-cluster environment.

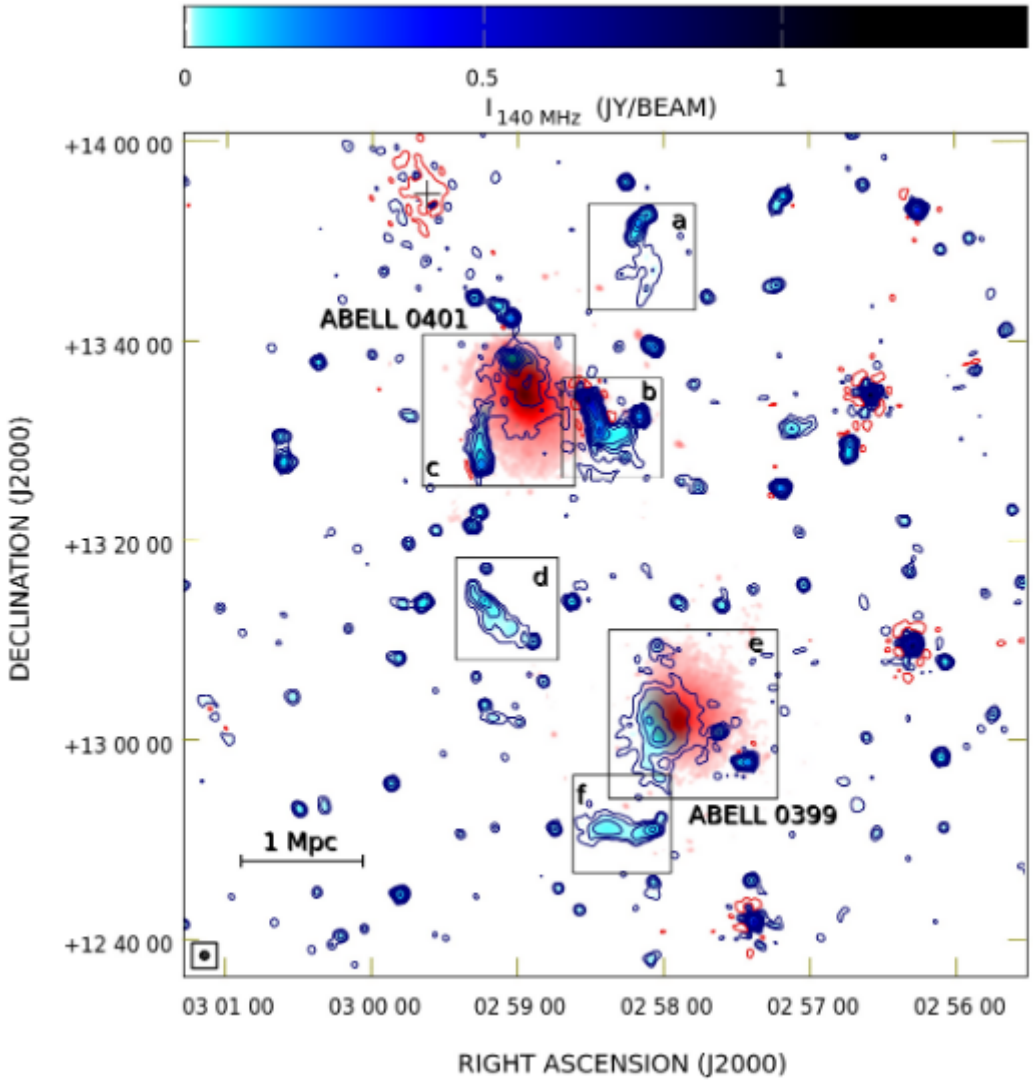

Figure 4.1: Composite image showing the low-frequency radio emission and the X-ray emission toward A399–A401. In red tones the X-ray image, obtained with the XMM-Newton satellite, in the $0.2-12$ keV band. Blue tones and contours represent the radio emission as obtained with LOFAR at 140 MHz. The radio image has a resolution of 50", shown on the bottom left. Contour levels start at 4 mJy/beam and increase by factors of 2. Regions of interest are labeled and marked with boxes. The black cross in the top of the image indicates a strong radio source removed from the image. From Govoni et al. (2019)

.

A first explanation of such radio emission has been provided by Govoni et al. (2019), whose asserted that could be due to multiple weak shocks present in the bridge region that re-accelerate a pre-existing population of mildly relativistic particles. Later, using a semi-analytical method, Brunetti and Vazza (2020) proposed that this emission could be originated by a turbulent re-acceleration (Fermi II process) which could also

amplified the magnetic field.
However, no conclusions about the emission model have been obtained so far.

A recent study on the bridge emission is the work made by Nunhokee et al. (2021). They investigated the spectral index of diffuse sources in the cluster pair A399–A401, using observations at 140 MHz (`LOFAR-HBA` data of Govoni et al. (2019)), 346 MHz and 1.4 GHz (Westerbork Synthesis Radio Telescope, WSRT). The bridge is only detected with the `LOFAR-HBA` data, and so for data at 346 MHz only upper limits have been used. They found a spectral index lower limit for the inter-cluster region of about 1.5, with a significance of 2σ ($\alpha > 1.5$).

No conclusions on the magnetic field strength have been obtained so far.

Throughout our work we used the Planck cosmology (Planck Collaboration et al., 2020), where 1" = 1.345 kpc at the cluster pair distance.

4.1 LOFAR Observations

The observations used in this work are part of the LoTSS (see Sec. 2.4). The A399–A401 pair was observed for an overall time of 8 hours, divided into 2 tranches of 4h each because of the low declination ($\delta \sim 13°$) of the target. Each 4 hours of target observation was followed by 10 minutes of calibrator observation, typically 3C196 and 3C295. For the LoTSS, and then for this study, observations were performed using the `HBA_DUAL_INNER` configuration of LOFAR. In such setting all the station within the Netherlands operate with 24 tiles and each substation in the core stations is correlated separately. This configuration does not reduce the number of short baselines or suffer from additional calibration difficulties caused by non-uniform beam shapes. However, by discarding 24 of the 48 tiles of the remote station, the sensitivity is reduced but the station gains a wider field of view.

4.1.1 Data reduction

The reduction of the LoTSS data is challenging due to the large data size, the requirement to reduce data almost in real time and the complexities involved in calibrating the direction-dependent ionospheric effects and beam model errors. Data from each pointing (8h 10min $\sim$ 16.35 TB) are archived with a time resolution of 1 s and a frequency resolution of 16 channels per 195.3 kHz sub-band by the observatory and stored in the LOFAR Long Term Archive (LTA). However, downloading this data is either prohibitively time consuming or expensive. To mitigate this, the data size is reduced

in the first steps of the calibration (Shimwell et al. 2019).
A complete treatment of the LoTSS data reduction and calibration can be found in Shimwell et al. (2017, 2019), here we briefly describe the main steps of such process.

At first, the standard LOFAR processing pipeline `PREFACTOR` was used to calculate the direction-independent corrections, then a direction-dependent calibration was subsequently performed to further improve the quality of the final images.

Direction independent calibration - PREFACTOR

As a first operation of the `PREFACTOR` pipeline, the LoTSS data (target + calibrator) are archived as 244 single sub-band files. Hence, each sub-band of the calibrator is flagged for interference with `AOFLAGGER`, averaged in frequency to two channels per 195 kHz sub-band and in time 8 s. After that, visibilities are calibrated using a model of the appropriate calibrator source.
Similarly, the 244 single sub-band target files are each flagged, corrected for ionospheric Faraday rotation, calibrated using the calibrator solutions, and averaged to a resolution of two channels per 195 kHz sub-band in frequency, and 8 s in time. In the final step of the direction-independent calibration pipeline, the data for each contiguous 10-SB block are sent to different compute nodes where they are each combined to a single file that is phase calibrated against a sky model for the target field, which is generated from the TIRF GMRT Sky Survey alternative data release (TGSS-ADR1, Intema et al. (2017)) catalogue.
Such first calibration would produce images like the one in Fig. 4.3.

Direction dependent calibration - DDFacet & KillMS

Further signal corruptions come from what are called Direction Dependent Effects (DDEs). These distortions are caused by ionospheric effects at low frequencies and errors in the station beam model of the HBA stations. In particular, they not only depend on direction but also on time, frequency and station. To correct for such corruptions one has to compute the corrections as for the direction-independent effects and then apply those corrections during imaging.
For the LoTSS, two software have been developed, `KillMS` to calculate the corrections and `DDFacet` to apply these when imaging.
The direction-dependent calibration goes through different and elaborated steps, performing several cycles of imaging and self-calibration (Shimwell et al., 2019). The basic idea is to subdivide the sky in 45 *facets*, as shown in Fig. 4.2, in order to calculate the corrections for each of these facets (i.e. for each direction). Before start the direction-dependent calibration, an initial direction-independent calibration is made obtaining

a model for the sky which is also integrated with the TGSS-ADR1 catalogue to ensure that all bright sources in the field are identified. The resulting sky model is used to define the 45 facets that cover the entire region. Subsequently, different cycles of direction-dependent calibration (with `KillMS`) and imaging (with `DDFacet`) are made. In each of these cycles the used sky model is the one produced in the previous cycle of imaging, this technique is called *self-calibration* and allows to improve the visibilities correction and producing better final images.
Although the direction-dependent correction faces many technical challenges, the improvement in the results is evident, as shown in Fig. 4.3.

Unfortunately, in the direction-dependent process it is assumed that the integrated polarization over the FoV is negligible. Usually this is a good assumptions unless there is an extended polarized source in the field, which is exactly the case of our study (See Sec. 4.2). Hence, the utilized data have been calibrated only direction independently with `PREFACTOR` and the direction-independent calibration of `DDFacet`.

4.2 Numerical simulations

As introduced in Sec. 1.4, we will consider the model proposed by Govoni et al. (2019) (and also described in Wittor et al., 2019) to explain the radio emission from the studied inter-cluster region.

The A399–A401 pair is made by two galaxy clusters in the early stages of a major merging process. Massive binary mergers are rare and powerful events, in which a large amount of kinetic energy is concentrated between the two main clusters in form of shock waves and turbulent motions, causing strong compression of gas matter in the inter-cluster region (Wittor et al., 2019). This compression leads to an amplification of the magnetic field, acceleration of energetic particles through DSA-like mechanisms, and also re-energization of pre-existent fossil plasma.
Therefore, as in the case of radio relics, shock or (re-)acceleration can power radio emitting electrons and explain this large radio ridge. Govoni et al. (2019) explored this scenario through simulations with the `ENZO` code (Bryan et al., 2014), accounting for MHD, cosmic expansion and gravity, but neglecting radiative losses and feedback. This simulation evolves a pair of merging galaxy clusters at a resolution of 3.95 kpc, with final masses and distance similar to the A399–A401 pair. To quantify the expected radio emission, they combined the electrons freshly accelerated at shock waves in the simulation with a radio emission model (Govoni et al., 2019).

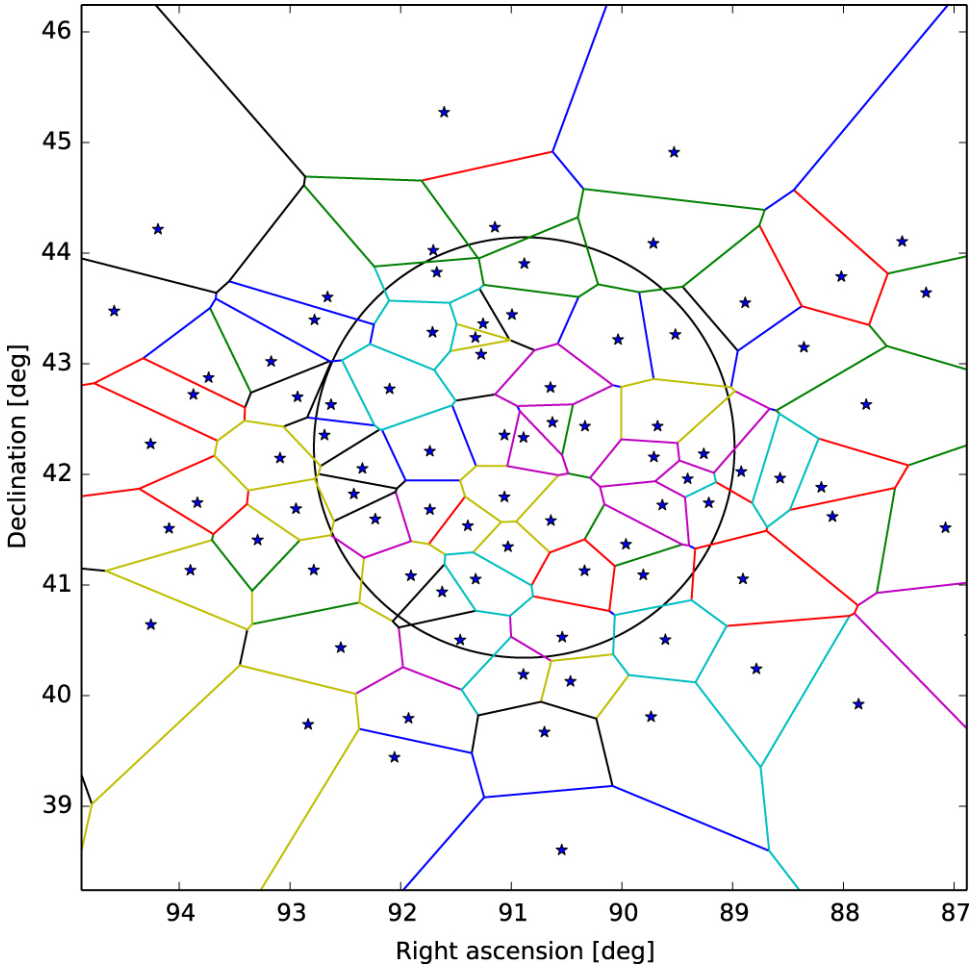

Figure 4.2: Voronoi tessellation used for the Toothbrush cluster field. The black circle indicates the Half Power Beam Width (HPBW) of the station beam at 150 MHz. Stars indicate the center points, placed on bright sources (or source groups), that define the tessellation. This tessellation scheme assigns each point on the sky to the closest calibrator source. The area covered by facets is limited by the maximum image size allowed by the user for a given facet. This is done to prevent facets from growing too large, which would lead to errors in the calibration of sources at the edge of a facet. A consequence of this is that the user must take care to have a reasonably uniform distribution of calibrator directions in order to avoid the appearance of gaps in the final image. From van Weeren et al. (2016).

They found that, due to the scarcity of strong shocks in this region and to the drop of the assumed electron acceleration efficiency for $M \leq 3$ shocks, radio emission by freshly accelerated electrons falls $\sim$ 1000 times below the sensitivity of LOFAR observations reported in Govoni et al. (2019). This generates a patchy emission that only traces the location of the strongest shocks. In this scenario, the only emission detectable by LOFAR observations would be associated with a substructure transiting transverse to the line of sight, while the detected emission shows a brighter and more broadly distributed pattern (see Govoni et al., 2019).

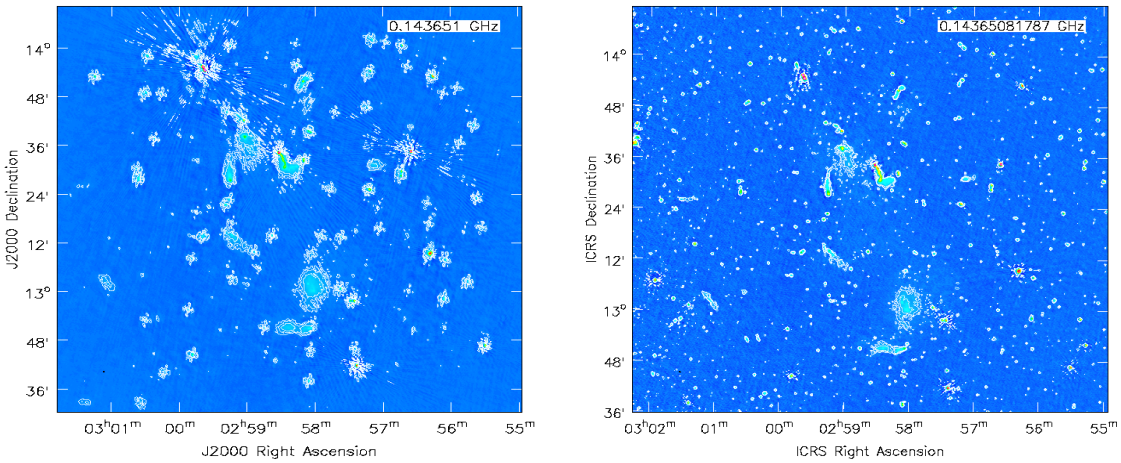

Figure 4.3: On the left panel is shown the image of the A399–A401 pair calibrated only with the direction-independent calibration. On the right, instead, is presented the same field, but this time with a direction-dependent calibration. The improvement is clearly visible. In particular, a number of point like sources appear on the right image due to the resolution improvement occurred with the direction-dependent calibration and there is also a significant reduction of the artefacts. Both images are made with a resolution of 20". Contours shown in white are: for the *left* image at 4, 8, 16 $\times$ RMS, where RMS is 360 μJy/beam; for the *right* image at 3, 6, 12 $\times$ RMS, with an RMS of 260μJy/beam. Therefore, also the background noise is reduced with the direction-dependend calibration.

As an alternative model, they tested the additional contribution from a pre-existing population of relativistic electrons which fills most of the bridge volume, and is re-accelerated by weak shocks ($M \sim 2-3$) in the bridge region (Govoni et al., 2019). This additional contribution from fossil plasma is able to reproduce the emission from the bridge (Fig. 4.4), but limits the age of these electrons to < 1 Gyr due to radiative losses.

Wittor et al. (2019) computed the polarized emission that should result from the second case. In Fig. 4.5 we can see that, in this shock-driven emission model, about 70% of the bridge emission should be polarized. Therefore, polarization studies of the bridge should be able to detect its emission.

4.3 Data analysis

LoTSS pointings have a FoV of $\sim 3° - 4°$, depending on the wavelength. The area covered by the bridge is much smaller than the LoTSS field of view, therefore, in order to speed up the subsequent steps, we selected the visibilities corresponding to the bridge region with a procedure called "extraction" which we illustrate below.

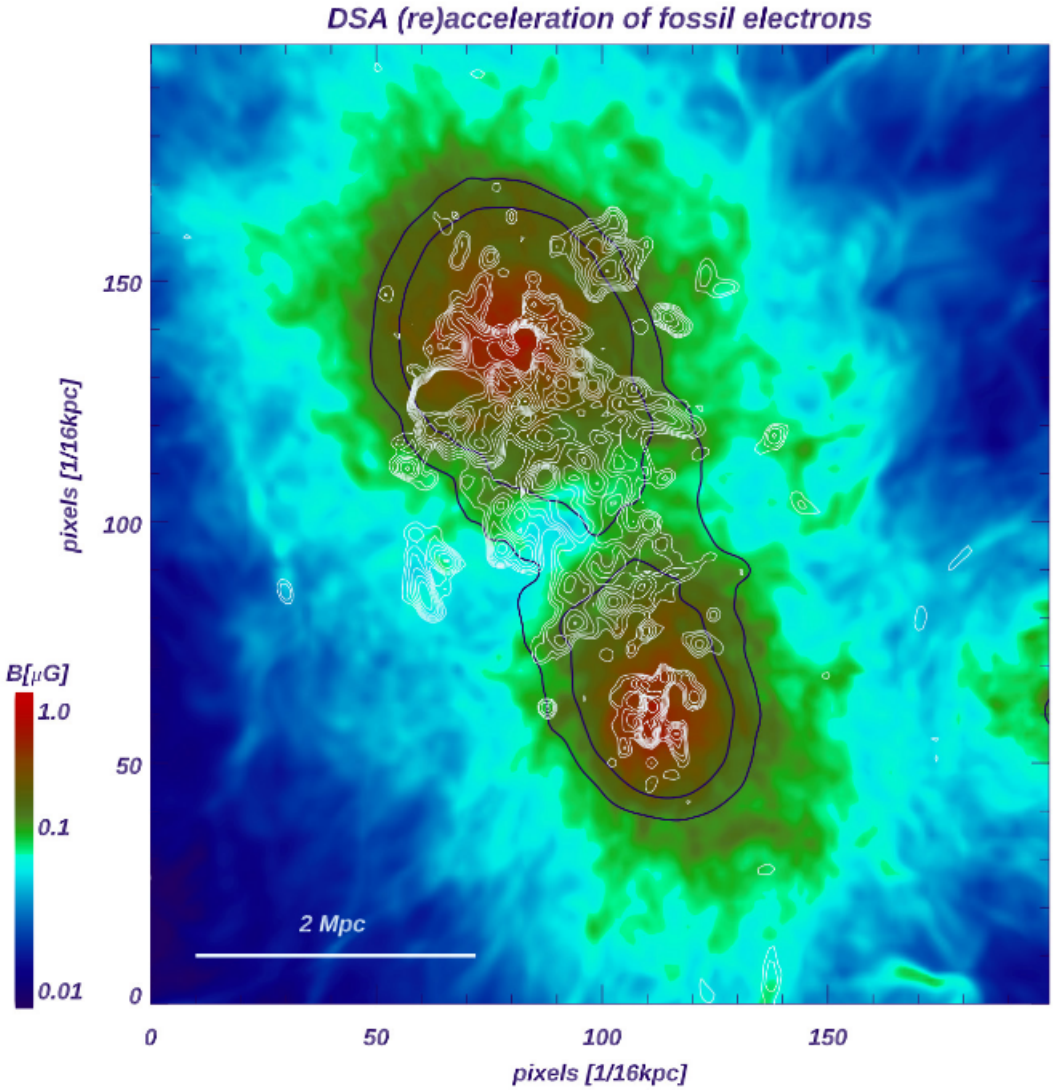

Figure 4.4: Image of a simulated interacting cluster pair by Wittor et al. (2019). The image shows: the projected magnetic field intensity in (colors); the integrated SZ signal (black contours); the radio emission (white contours). One can see that the radio emission is extended also in the inter-cluster region.

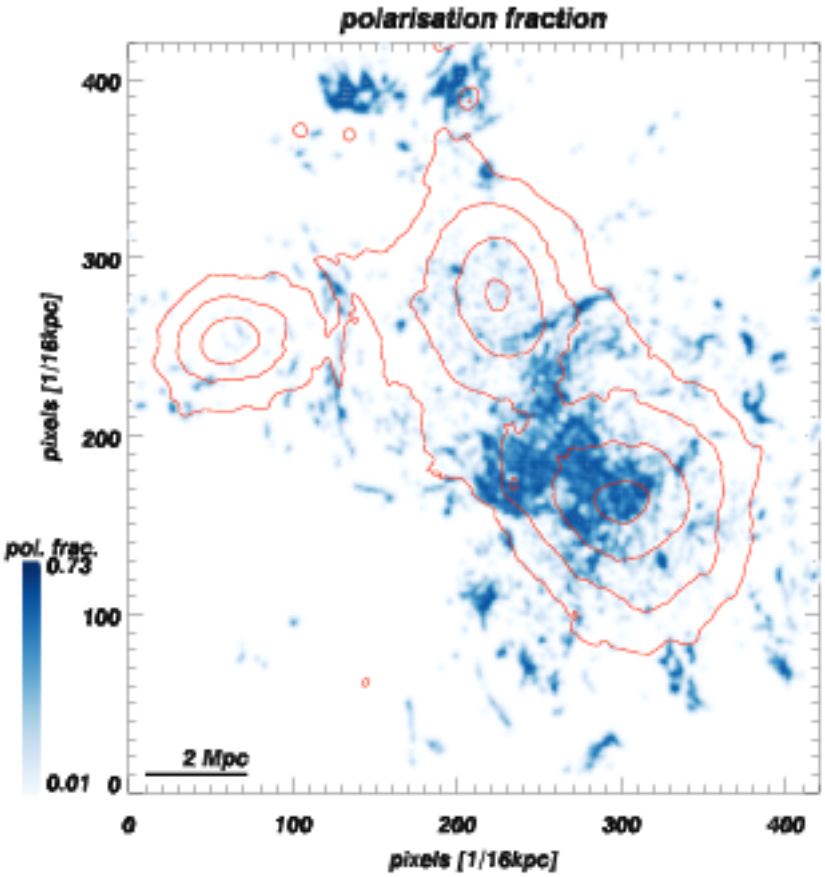

Figure 4.5: Numerical simulations of a cluster merger between two clusters similar to A399 and A401. In blue is shown the polarization fraction of the total emission, whether orange contours are the density levels of the region. It can be see that in the inter-cluster region the polarization fraction reach about 70% (from Wittor et al., 2019).

We made use of the script `sub-sources-outside-region.py` [1] passing as input the region-file which specifies the interested field region (Fig. 4.6) and a list of the Measurement Set files containing the visibilities of the entire observations. Starting from the clean image, the program selects the visibilities corresponding to the image portion within the provided region. Then, it Fourier transforms the whole image and, once in the Fourier space, subtracts all the visibilites which corresponds to image portions outside the wanted region (of the clean image). Finally, re-transforms the residual visibilities in the real space, obtaining an image of only the interested region.
Such script, allows also to average in frequency the visibility-subtracted data. Our choice was to keep the original frequency resolution obtained after `PREFACTOR`, in order to avoid bandwidth depolarization.

[1] https://github.com/mhardcastle/ddf-pipeline/blob/master/scripts/sub-sources-outside-region.py

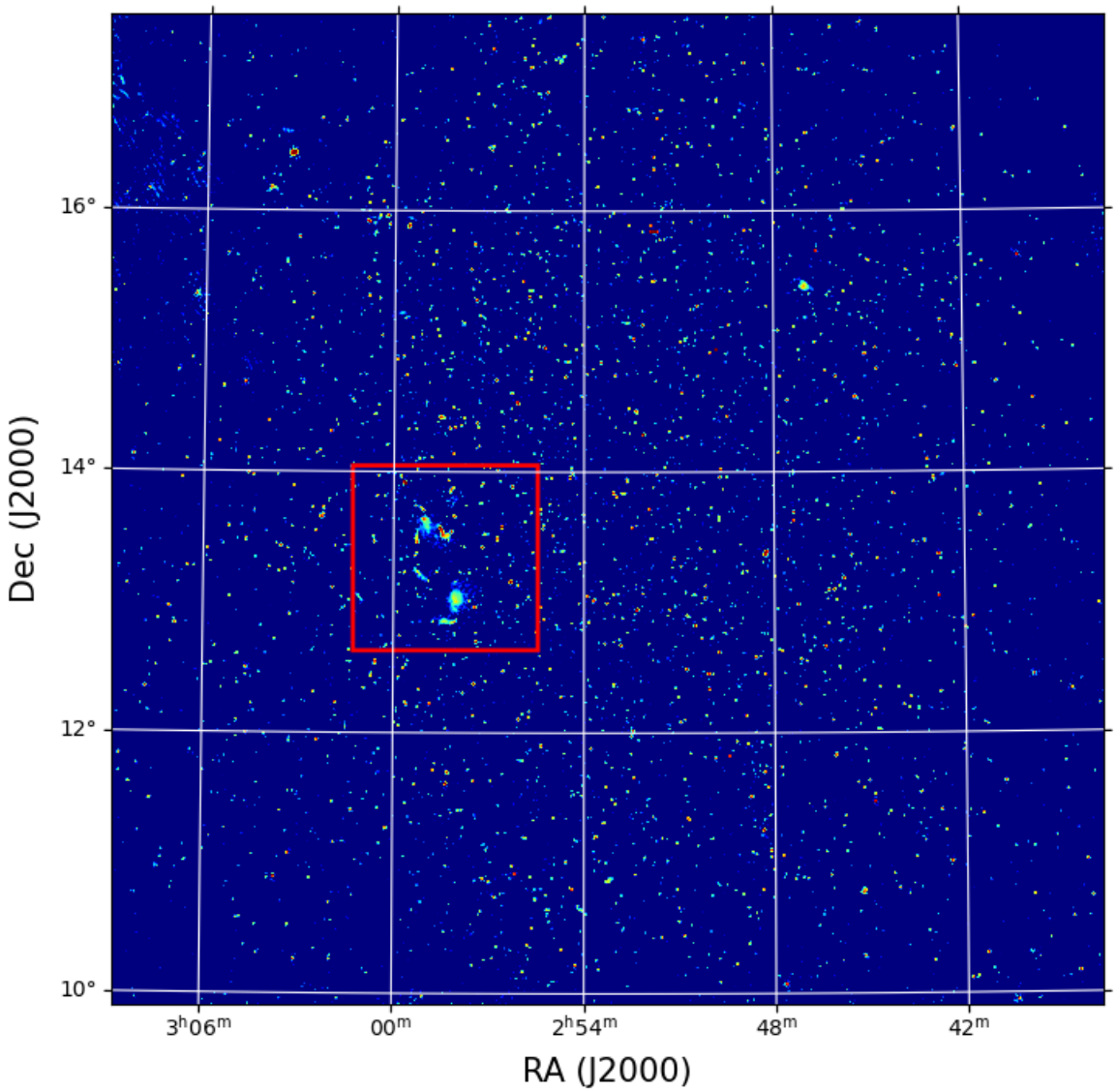

Figure 4.6: Full LoTSS P043+14 pointing, at a resolution of 20". The bridge region is highlighted in red.

After the subtraction, we computed the *primary beam correction* towards the target coordinates, and applied it directly to the visibilities. With this correction we accounted for the non-uniform response of the telescope to the total intensity in the observed region.
After these first steps we proceeded with the imaging.

4.3.1 Imaging

At first we made images with 6" and 20" resolution for both the studied observations, named L579353 and L576817, producing images like in Fig. 4.7 and 4.8.

With such images, we had a first look to the studied field at the same resolutions

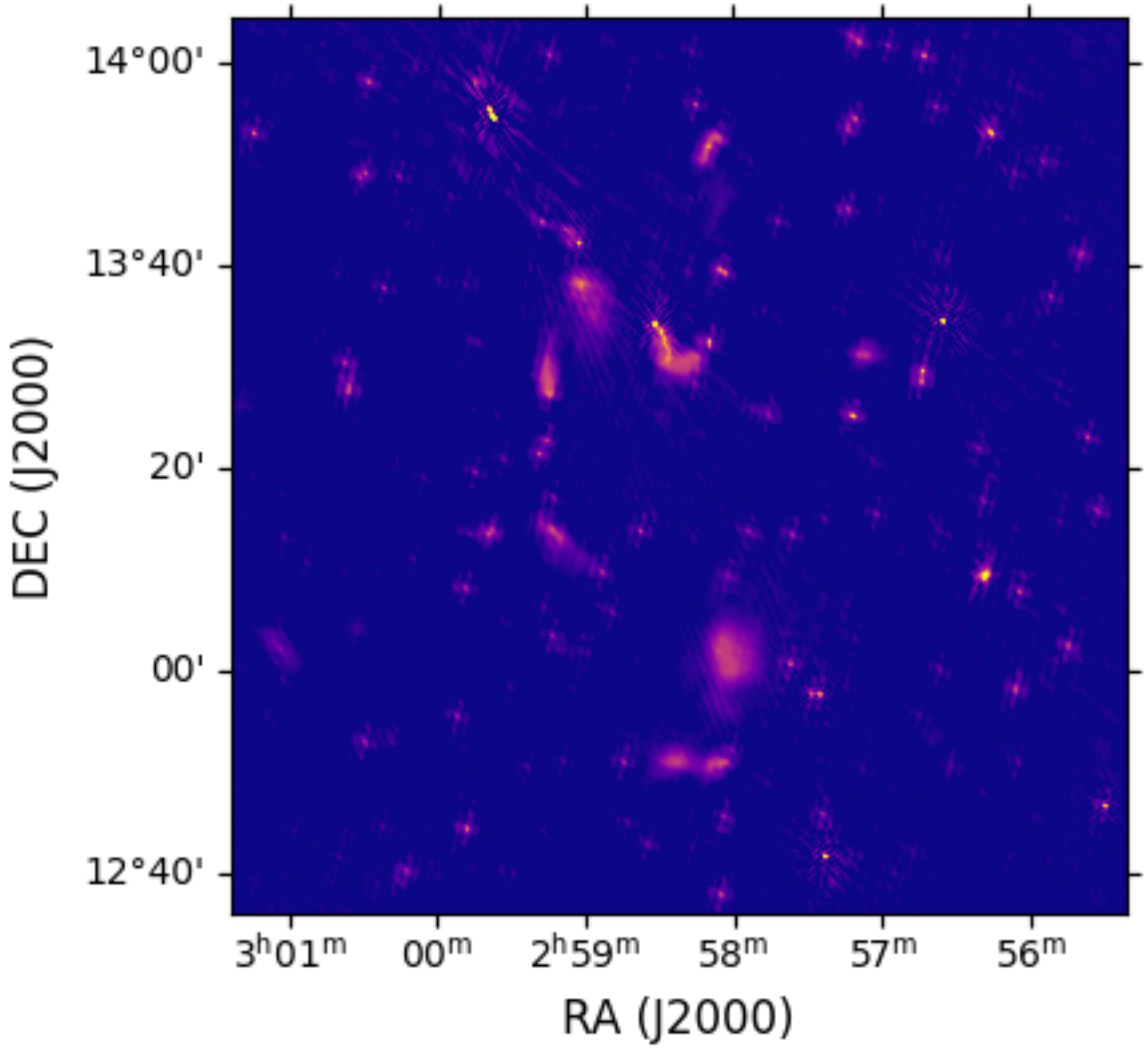

Figure 4.7: Images at 6" resolution of the same field presented in Fig. 4.3. In this high resolution image, the compact sources are better resolved but poor diffuse emission has been cleaned.

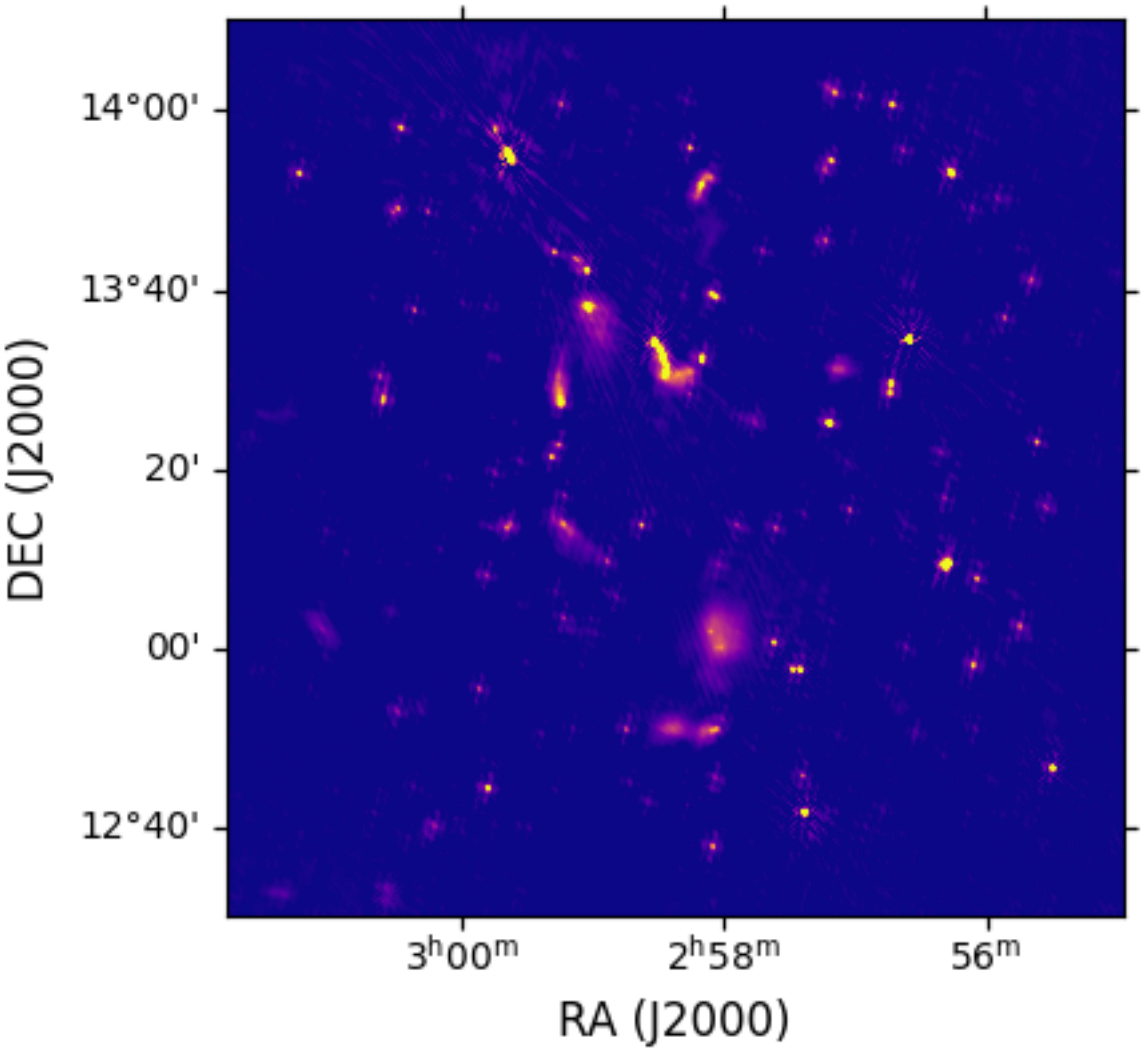

Figure 4.8: Images at 20" resolution of the same field presented in Fig. 4.3. In this lower resolution image we clearly see an evidenced detection of the diffuse emission.

as in the LoTSS. This allowed a comparison between our and LoTSS images and then checking for eventual errors in the calibration.
At these resolutions we did not find any sign of bridge emission. Therefore, we reduced the resolution in order to detect larger scale emission.

After these preliminary images, we focused on finding the best imaging parameters to detect the bridge and to recover its emission. In order to this, we tried different combinations of the `briggs` and `taper` parameters of *WSClean*. Different values of these parameters change the maximun and minimun resolution of the image, weighting differently the signal registered from long and short baselines. Because of the extended size of the bridge, the shortest baselines have the highest sensitivity to its emission. Also we had to take in account the problem of high secondary lobes in the telescope beam when "degrade" it using mainly the short baselines. We found a good compromise between low resolution images and the secondary lobes problem, imaging with a `briggs` and a `taper` values respectively of 0.5 and 40", resulting in a resolution of 107". With these parameters we obtained a clear detection of the bridge between the clusters as shown in Fig. 4.9.

In addition, we produced images at 6", 20" and 107" not only in total intensity, stokes parameter I, but also in the polarization parameters Q and U. In order to avoid depolarization, we did not average in frequency, producing image cubes with a frequency resolution of $\sim$ 97 kHz. In fact, as expressed by Eq. 3.31, too wide frequency (or wavelength) sampling will cause lack of sensitivity to polarized signal at high Faraday depth.

4.3.2 *RM* analysis

As explained in Chapter 3, *RM* studies provide information on magnetic field strength. Here, we used this method to obtain constraints on such features for the A399–A401 pair.

With the images in the Q and U Stokes parameters, we firstly performed the RM synthesis on the 6" and 20" resolution images using the scripts developed by Purcell et al. (2020). With the Q and U frequency cubes, we computed the Faraday spectra in the range ± 170 rad/m^2 and with a resolution of $\sim$ 1.17 rad/m^2. As output, we obtained 480 images of the field polarized emission for different values of ϕ. What we found were few roughly compact sources that show signs of polarized emission once their radiation has been de-rotated for a certain Faraday depth (Fig. 4.10).

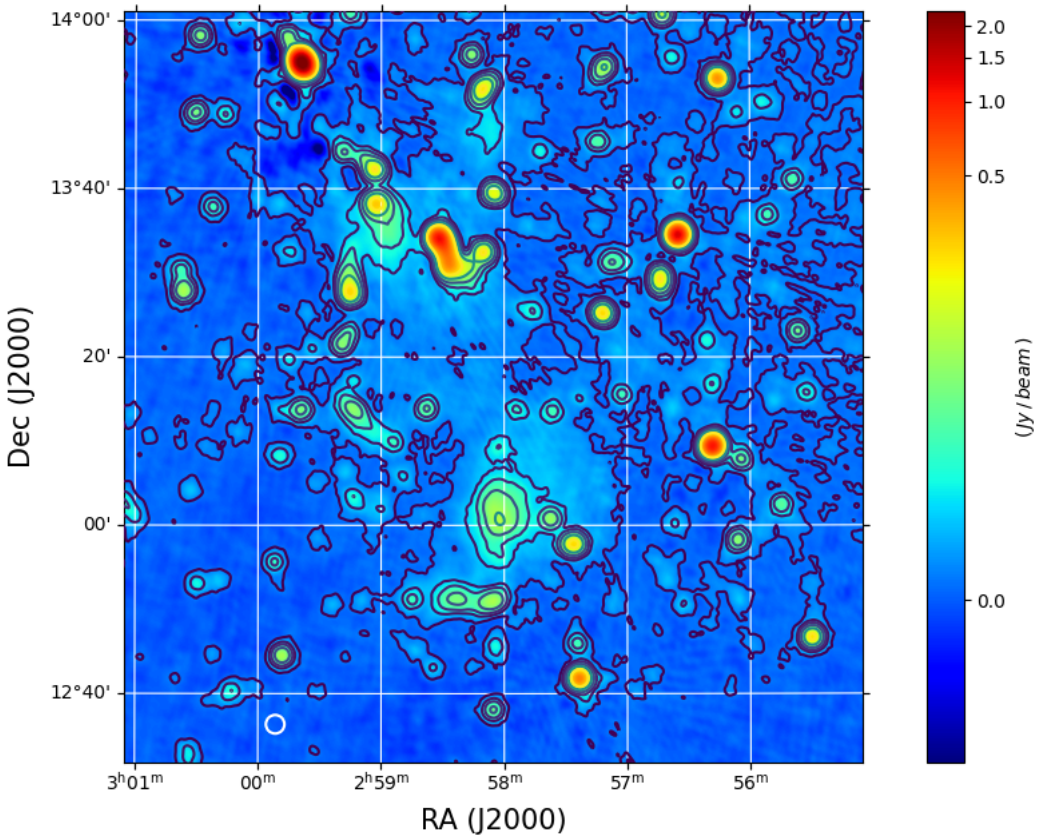

Figure 4.9: Image of the A399–A401 pair at $\sim$ 144 MHz. The restoring beam of $107'' \times 107''$ is shown in white in the bottom left. The contours in black are at 4, 20, 40, 80, 160 and 320 $\times$ RMS, where RMS is 620 μJy/beam.

Another way to look at these sources is studying the polarized emission as a function of the Faraday depth, i.e. the FDF spectrum generated by the RM synthesis (Fig. 4.12). If we consider the whole field emission, there are three main peaks in the FDF at different Faraday depths. Moving from higher to lower ϕ values, the first peak, at $\phi = \phi_{gal} = 7.5 \pm 0.001\,\mathrm{rad/m^2}$ [2] is due to the Galactic polarized emission (See. Fig 4.12). It is possible to identify the origin of this peak because it becomes more and more important increasing the size of the selected sky region as shown in Fig. 4.13. This is because the polarized emission of the Galaxy covers a wide area in the field and so, increasing the region size, more Galaxy emission is detected.

Another peak, in the Faraday spectrum, that is always present, is a peak located at $\phi = \phi_{instr} = 2.1 \pm 0.001$ rad/m^2. This one is generated by *instrumental leakage*, which occurs because no polarization calibration has been made on our data.
Finally, the last peak in the Faraday spectrum is at $\phi = -1.2 \pm 0.001$ rad/m^2. This is

[2]Errors have been computed following Brentjens and de Bruyn (2005)

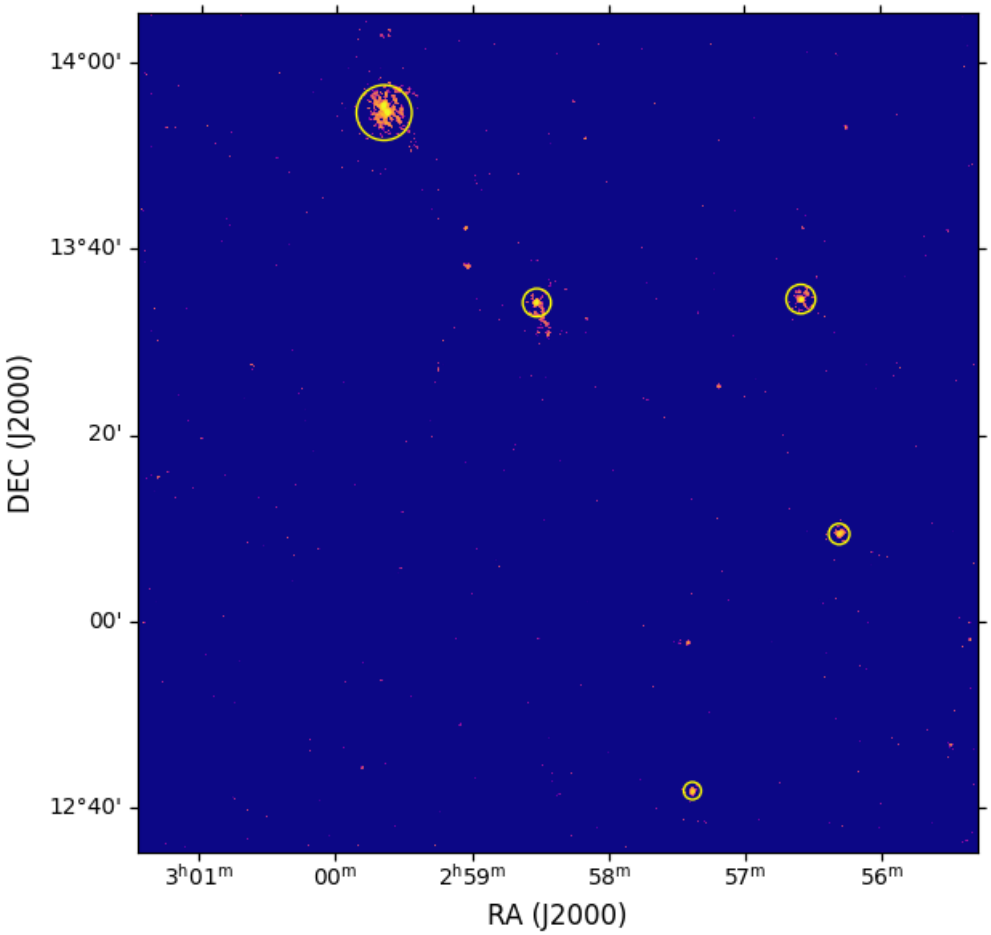

Figure 4.10: Slice of the FDF cube created by the RM synthesis at a fixed Faraday depth. It shows the polarized emission of the field once the radiation has been de-rotated by a Faraday depth of ~ -1.2 rad/m^2.

due to the polarized radiation of the brightest polarized source in the FoV, that is also transferred to the other polarized sources because of the issue mentioned in Sec. 4.1.1 for the direction-dependent calibration[3]. We note that no polarization peak is detected corresponding to the bridge emission.

Then, we performed the RM synthesis also for the Q and U images where the bridge is detected, i.e. with a resolution of 107". Studying the product of the RM synthesis on such images, Fig. 4.14, we found no detection of bridge polarized emission. In particular, analyzing the FDF of the region between the two clusters (see Fig. 4.17) we did not find any peak in the Faraday spectrum, apart from the galactic and instrumental

[3]We noticed that all sources that show a polarized emission after the RM synthesis, have the peak in the Faraday spectrum all at the same ϕ. This is of course strange and also non physical, because it would imply that the radiation from different sources at large angular distances is Faraday rotated by the same medium. Therefore, we deduced that also during the direction-independent step of the `DDFacet` pipeline some assumption are made on the polarized emission that causes this effect.

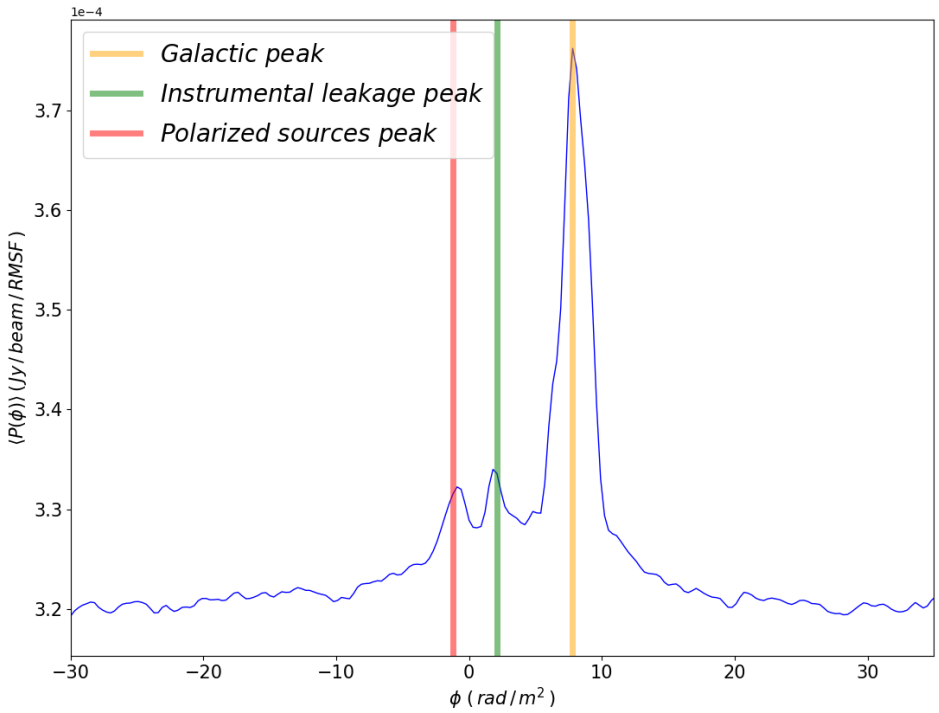

Figure 4.11: Faraday spectrum of the average polarized intensity $\langle P(\phi) \rangle$ of the whole studied field at 20" resolution. It presents three peaks, which are due to the galactic foreground medium, the instrumental leakage and the presence of polarized emission by field sources. Because of the studied region is the total field, the strongest peak is the one related to the galactic foreground. If we had selected a smaller region closer to one of the polarized sources, such peak would be less important, while the source peak would be dominant.

peak.

4.3.3 Limit on polarized emission and prediction from theoretical models

The observational results obtained above, i.e. no polarized emission detected from the bridge, can be used to obtain information on the origin of the bridge and on the magnetic field in the bridge region.

First, we tested whether the observational constraint is consistent with the prediction from the model used by Govoni et al. (2019) to explain the origin of the bridge.

In order to do this, we recovered the bridge emission from our images and used predictions from simulations (Wittor et al., 2019) to generate an emission model for the bridge. Having this model, we performed a Faraday rotation of it following Eq. (3.13) with an RM parameter $\gg \phi_{gal}$. Then, we injected this rotated model in the original data and re-computed the imaging process. Finally, we used the RM synthesis technique to recover the polarization emission of the field and testing whether the bridge

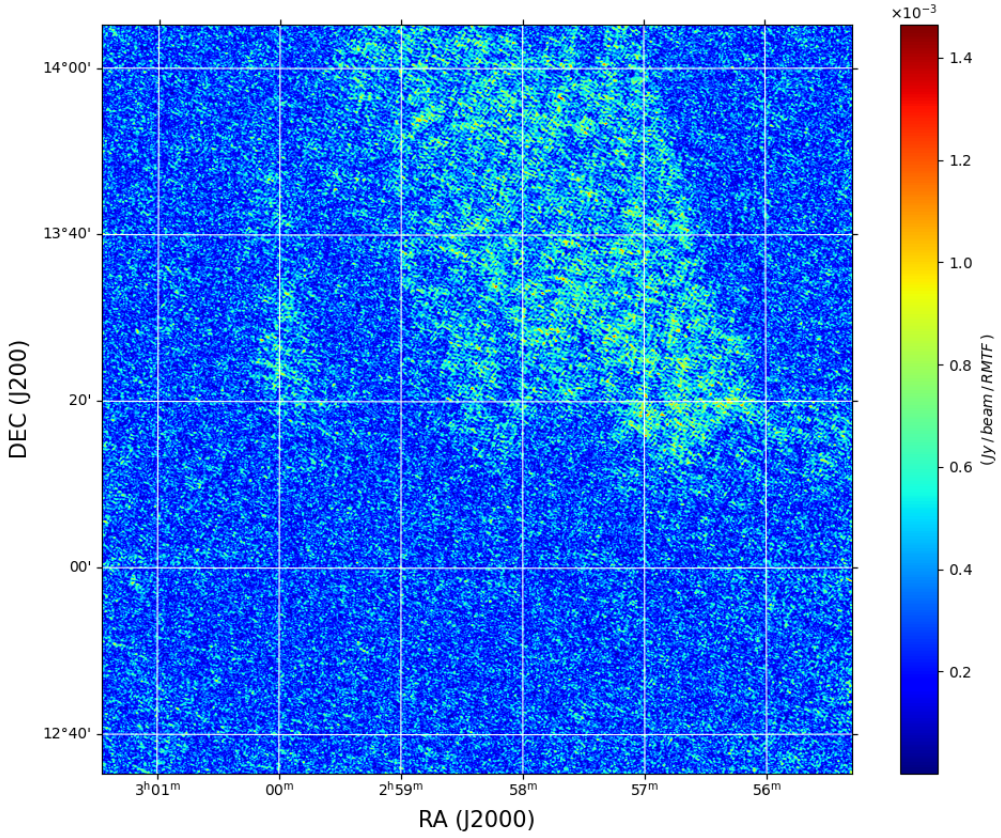

Figure 4.12: Slice of the FDF cube produced by the RM synthesis, at $\phi \sim 7.5$ rad/m^2. It shows the Galactic polarized emission detected in the field.

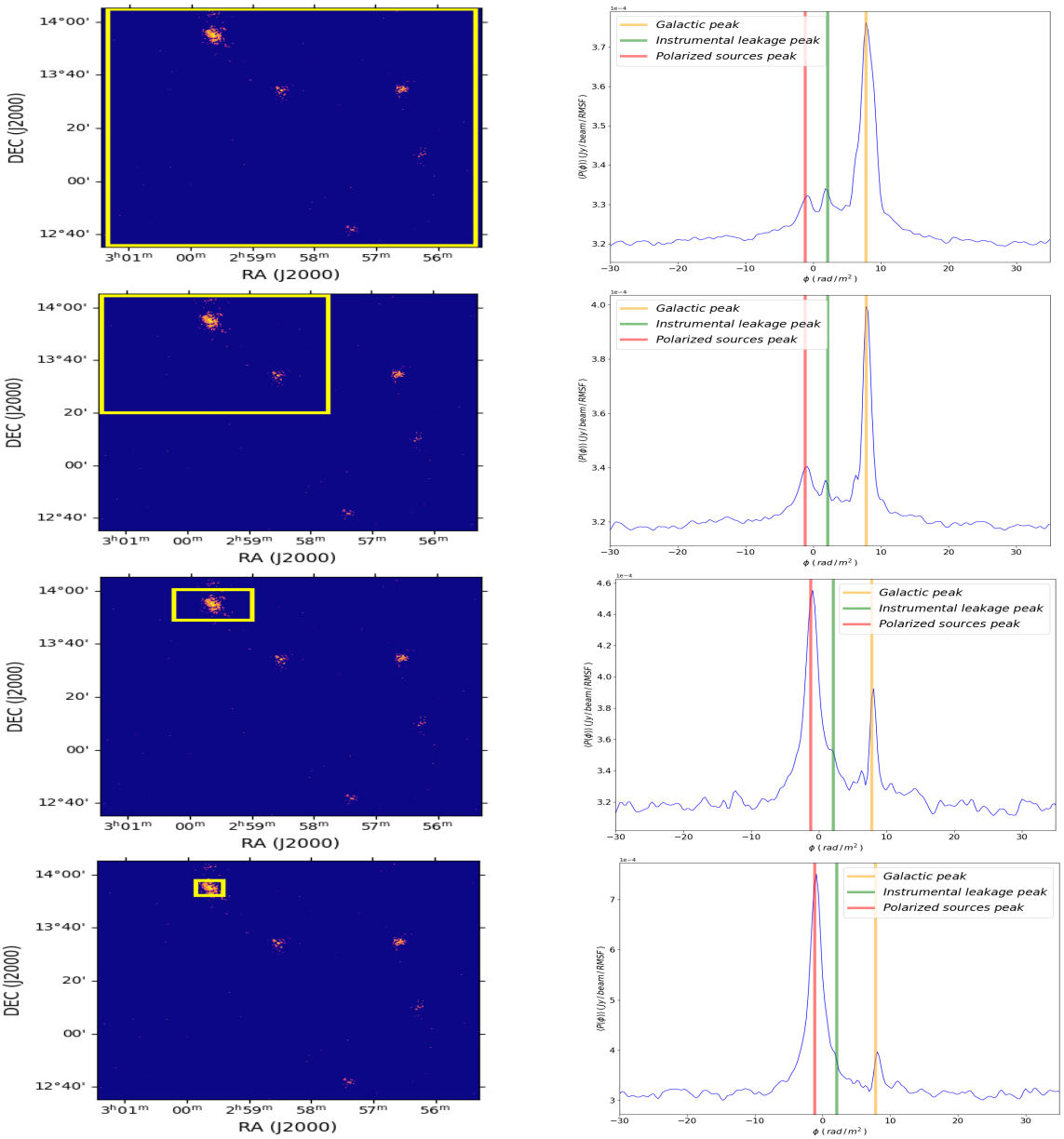

Figure 4.13: Faraday spectra of the average polarized emission $\langle P(\phi) \rangle$ over different selected regions from the same image. In particular, one can see that increasing the size of the considered region the galactic peak dominates on the others. Instead, choosing a region closer and closer to a polarized source the dominant peak becomes the one associated with that particular source.
The polarization map on the left has been obtained from the RM synthesis on images with a resolution of 20". In particular, it is the image in the polarization cube outputted by the RM synthesis, at $\phi \sim -1.2$ rad/m^2.

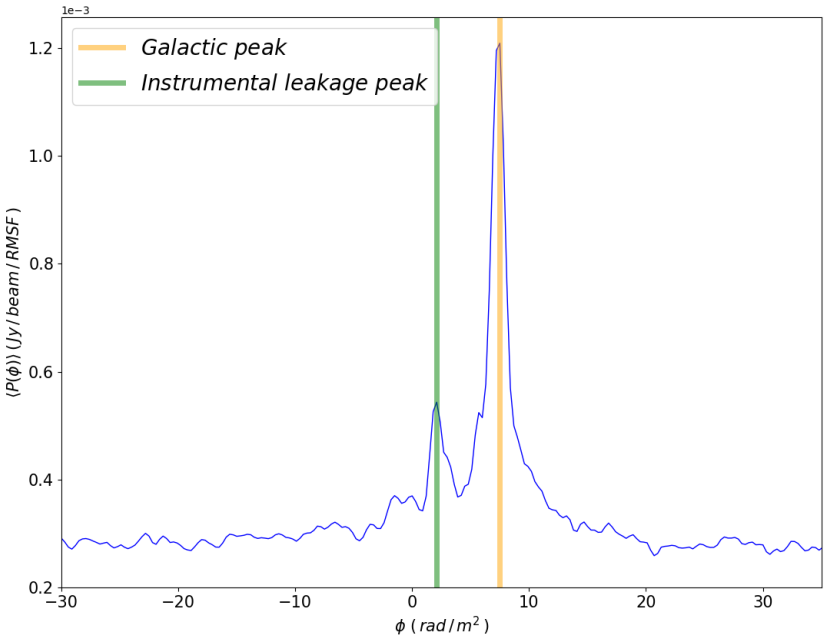

Figure 4.14: Faraday spectrum of the average polarized intensity $\langle P(\phi) \rangle$ of the bridge region, i.e. the sky region where the bridge is detected in Fig. 4.9. Obtained from 480 Q and U images with a resolution of 107".

emission, as predicted by the simulations, should have been detected or not.
Since this step, for simplicity [4], we decided to use only one of the two observations (n. L56817).

The bridge model was obtained performing the imaging process using the optimal bridge parameters of `taper` and `briggs` derived in Sec. 4.3.1.
To produce a more accurate emission model for the bridge, before imaging, we subtracted from the original data the emission from compact sources embedded in the bridge emission shown in Fig. 4.15. An example of this subtraction is shown in Fig. 4.16, where about 90% of the emission of source A in Fig. 4.15 has been removed. This allowed to extract a more accurate model for the bridge emission in the subsequent steps. With the imaging process, one will produce an emission map for the whole analyzed field. Therefore, in order to obtain only the bridge emission, we masked the overall map leaving the emission only in a specific region (Fig. 4.17) in the middle of the two clusters.

Once we had the bridge emission model in the total intensity (Stokes parameter I), we used the model proposed by Wittor et al. (2019) to obtain an emission model for the bridge polarized intensity. In particular, as explained in Sec. 4.2, from simulations

[4] We could have used both of the observations in order, for example, to increase the SNR. However, because on our data no polarization calibration were applied, the intrinsic polarization angle (Ψ_0, see Eq 3.7) of a certain source in the two observations could be different. Therefore, in order to use together both dataset, we would have performed a polarization corrections.

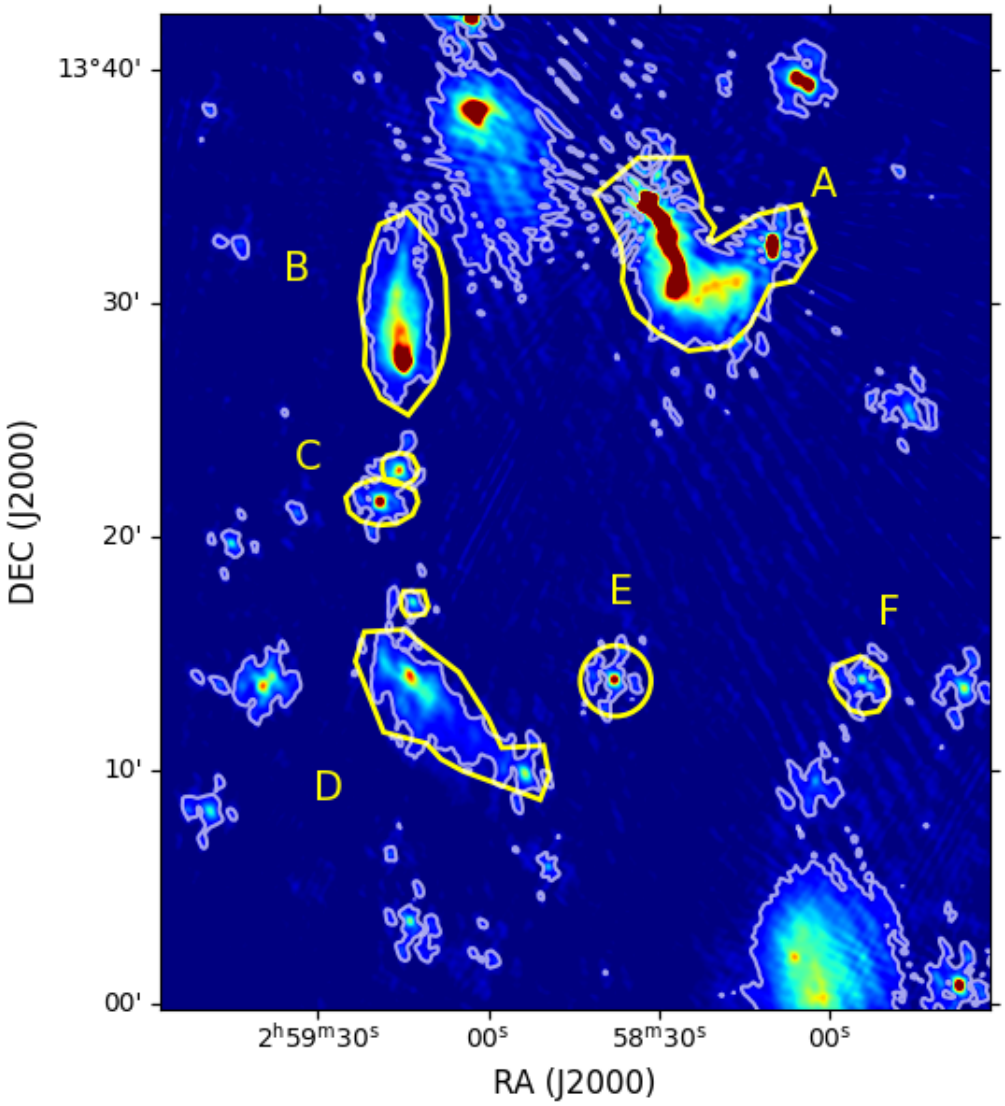

Figure 4.15: Zoom in of the bridge field, with highlighted the selected sources which will be subtracted by the dataset in order to recover the bridge emission model. Contours are at taken at $5 \times$ RMS, where RMS $= 3.5 \times 10^{-4}$ Jy/beam. The image has a resolution of 20".

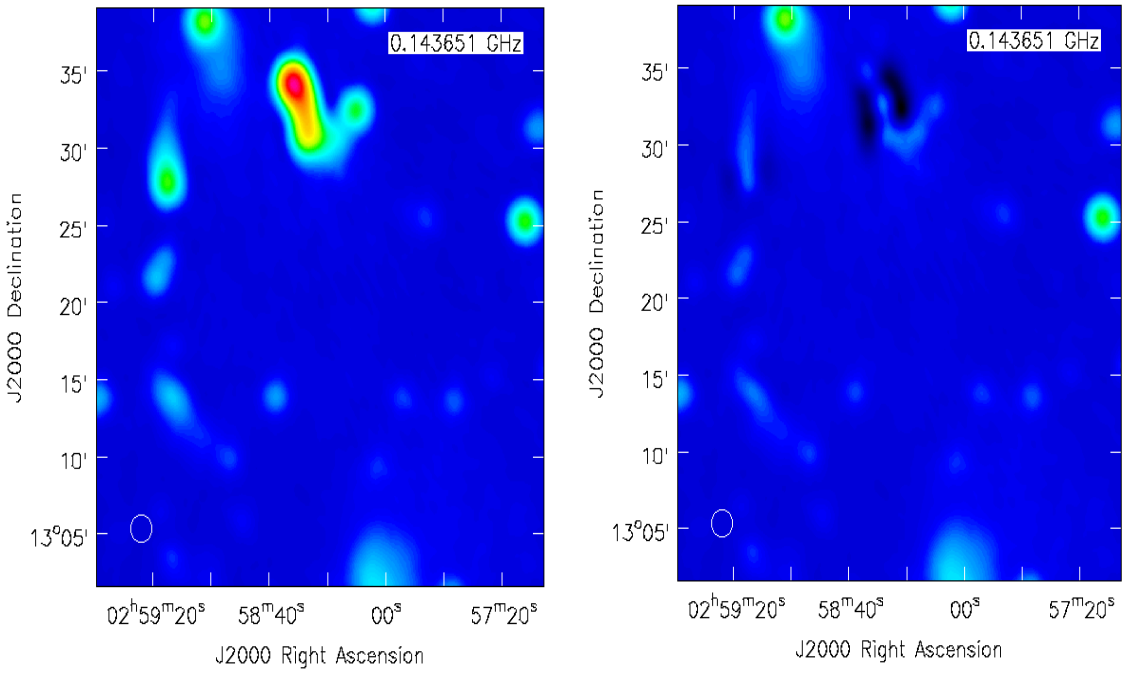

Figure 4.16: Zoom on the central bridge region, showing that the emission of the brightest sources the field (A, B, C and D in Fig. 4.15) have been subtracted. (source A in the top region of the bridge. The two images shown the source before (left) and after (right) the subtraction of the emission from the main compact sources near the bridge. In both images the resolution is 107" with the restoring beam shown in the lower left.

we would expect that about 70% of the bridge emission should be polarized, Fig. 4.5.

Therefore, in order to recover a polarized emission model of the bridge, we simply multiplied the total (I) emission model for a factor 0.7.
We want to obtain data with a bridge emission that has a polarized intensity $\sim 70\%$ of the observed flux in the stokes I parameter, i.e. $|P| = 0.7\,I$. Observationally, $|P|$ can be recovered through the Q and U Stokes parameters (See 3.1):

$$|P| = \sqrt{Q^2 + U^2} \tag{4.1}$$

which are directly related to the electric field components E_X and E_Y and their combinations:

$$Q = E_X^2 - E_Y^2 \tag{4.2}$$

$$U = 2E_X E_Y \cos(\Delta\phi) \tag{4.3}$$

where $\Delta\phi$ is the phase difference between the orthogonal components E_X and E_Y. Therefore, we are interested in the determining the Q and U parameters.

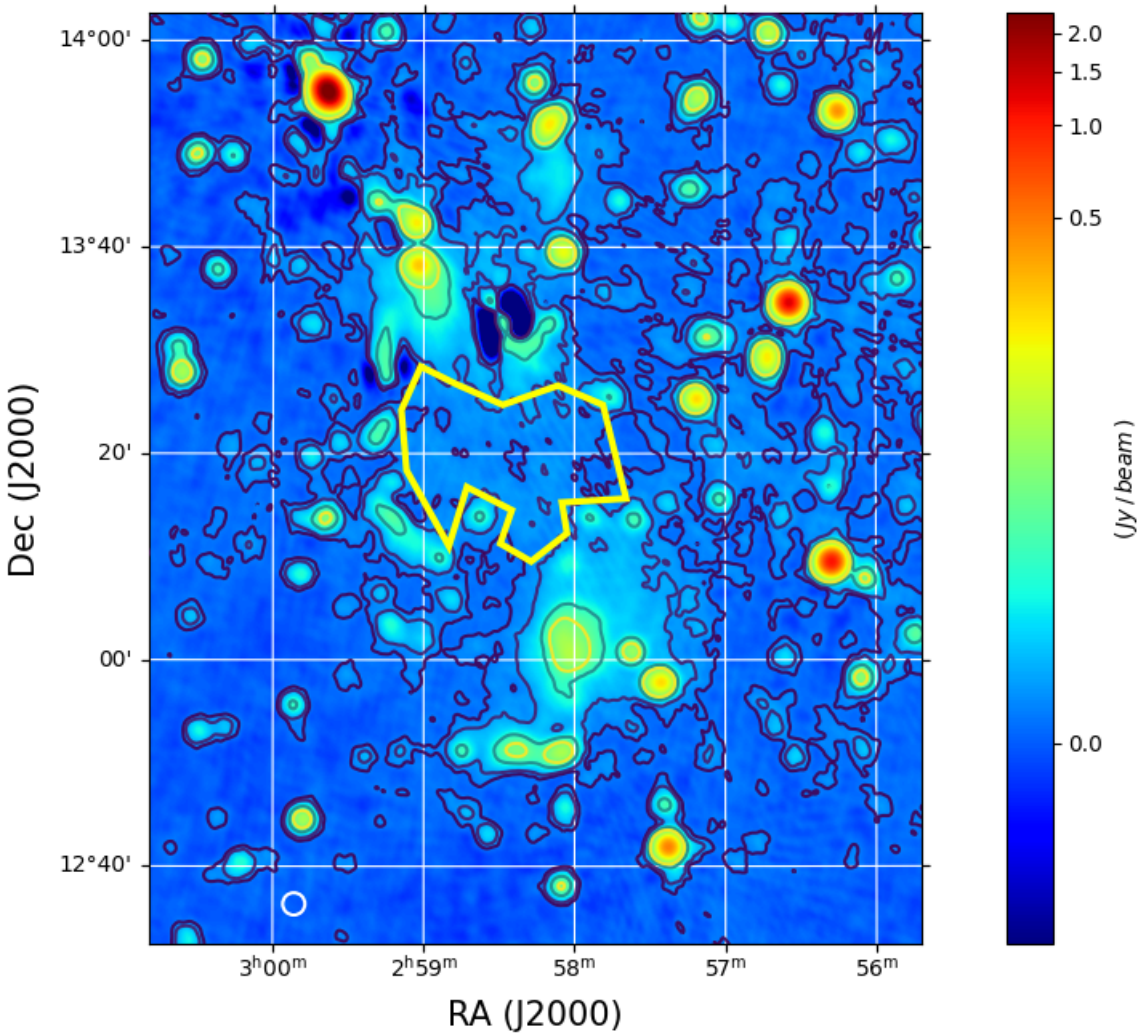

Figure 4.17: Image of the A399–A401 pair at $\sim$ 144 MHz once the sources cospatial with the bridge have been subtracted. In yellow is highlighted the region chosen to obtain the bridge emission model. The restoring beam of 107" $\times$ 107" is shown in white in the bottom left. The RMS of the image is $\sim$ 650 μJy/beam, with contours at 4, 10, 40 and 80 $\times$ RMS.

In addition, we have to assume what is the RM of the bridge that Faraday-rotates the emission. In fact, following the shock-driven emission model proposed by Wittor et al. (2019), we are assuming that the shocks have a size relatively small with respect the bridge size. So, we can consider a configuration where the shocks are located behind the bridge, and, consequently, their emission experiences Faraday rotation because of the bridge magnetized medium.

For now, we assume that the rotation is given by Eq. (3.13). We have assumed $RM = 20$ rad/m^2 because the FDF noise is almost constant apart in the region around the galactic ($\phi \sim 7.5$ rad/m^2) and instrumental ($\phi \sim 2.1$ rad/m^2) peaks which will be treat separately. Once obtained the polarization model map ($|P|$) and assumed RM, we have

to compute the Faraday-rotated Q and U map taking in account for the dependence on the wavelength (See Eq. 3.13). We derived the expressions on how compute the Q and U rotated signals starting from Eq. (3.13):

$$P = Q + iU = p_0\, e^{2i(\Psi_0 + RM\lambda^2)}.$$

For the purpose of this work we can assume $\Psi_0 = 0$, in fact we are only interested in how much the polarization angle is being rotated (because it is where the information on the magnetic field lies) and not what the intrinsic angle is.
Decomposing the intrinsic polarization, $p_0 e^{2i\Psi_0}$, in the two Stokes parameter (Q_0 and U_0):

$$P = (Q_0 + iU_0)\, e^{2iRM\lambda^2}. \tag{4.4}$$

Applying the Euler's formula and defining $\theta = RM\lambda^2$, the relation becomes:

$$P = (Q_0 + iU_0)(\cos 2\theta + i \sin 2\theta). \tag{4.5}$$

Then, computing the multiplications and grouping real and imaginary terms one derives the final expression:

$$P = (Q_0 \cos 2\theta - U_0 \sin 2\theta) + i(U_0 \cos 2\theta + Q_0 \sin 2\theta). \tag{4.6}$$

Thus, the Q and U components of the Faraday-rotated P vector are:

$$Q = Q_0 \cos 2\theta - U_0 \sin 2\theta \tag{4.7}$$

$$U = U_0 \cos 2\theta + Q_0 \sin 2\theta \tag{4.8}$$

Applying this method, we produced images of the bridge polarized emission rotated by a Faraday screen with a Faraday depth $\phi = 20$ rad/m^2.
In order to reduce the computational time, we decided to make 100 images in the frequency range of our observations, $120 - 168$ MHz, and not 480 as the original data. Therefore, for self-consistency, such image number is also the channel number of the images produced with the imaging process in the subsequent steps. According with Eq (3.31), this lower number of channels (with respect the original 480), will leads to a reduction of the maximum detectable Faraday depth. In particular 100 channels will limit the sensitivity to $\phi_{max} \sim 35$ rad/m^2. However this is not a problem because we saw no peak at such high values and we will inject the bridge emission at $\phi = 20$ rad/m^2.

To insert these rotated Q and U images in the original data, we calculated the anti-Fourier transform of the simulated images, accounting also for the antenna gain, and

injected these visibilities inside the real observations. Then, we produced new cubes of Q and U containing the mock polarized emission from the bridge and performed the RM synthesis. Results of this process are shown in Fig 4.18 and Fig. 4.19.

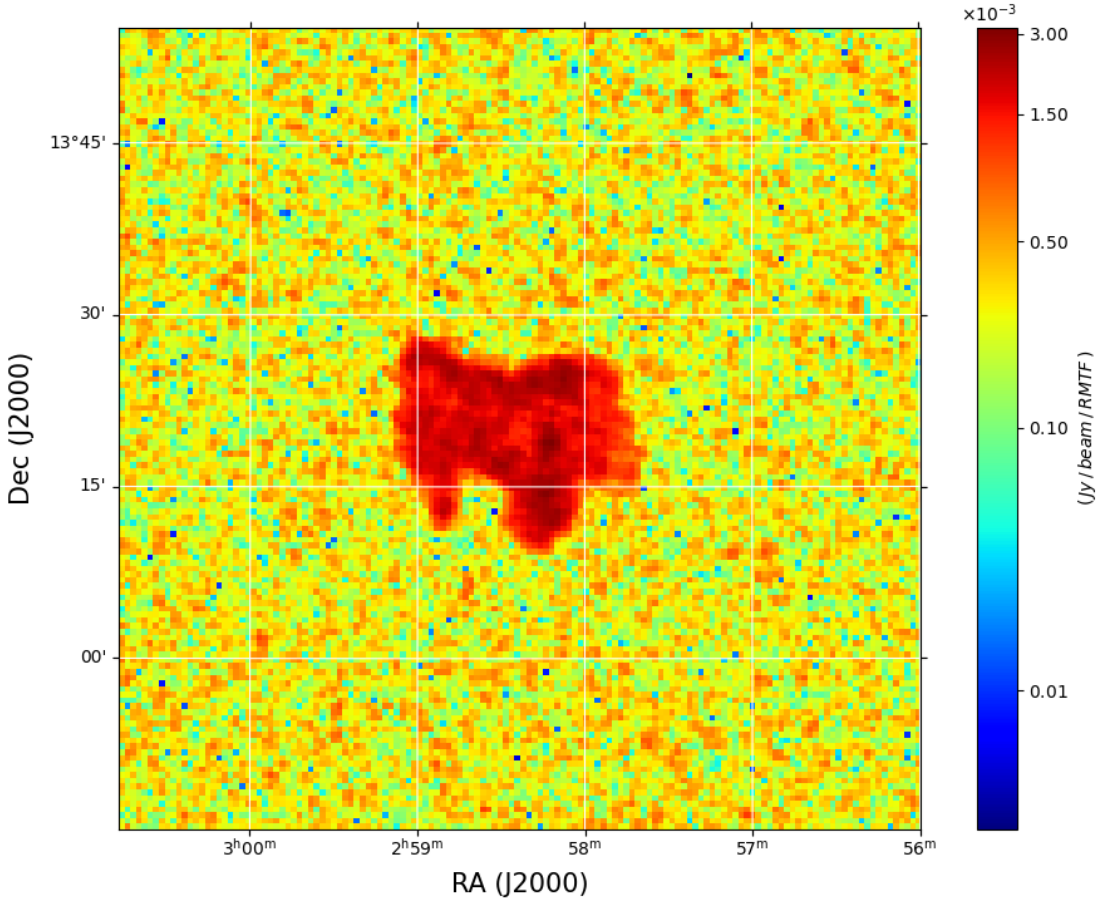

Figure 4.18: Slice at $\phi \simeq 20$ rad/m^2 of the FDF cube produced by the RM synthesis. Studying this particular slice, it is clear that the bridge emission should be detected if its emission was exactly the one predicted by the model.

Hence, if the emission was like the one predicted by the model, and rotated only by a simple Faraday-screen, the peak should be clearly visible in this spectrum with a SNR of ≈ 180. Yet, as presented in the previous section (Fig. 4.14), this is in contrast with observations. Therefore, we can conclude that some mechanism, like those presented in Sec. 3.2.1, must occur and cause depolarization of the bridge emission. In the case of depolarization for external Faraday dispersion (Sec. 3.2.1), this result also shows that a magnetic field is present in the bridge region, which, in particular, fluctuates on a scale range originating the depolarization.

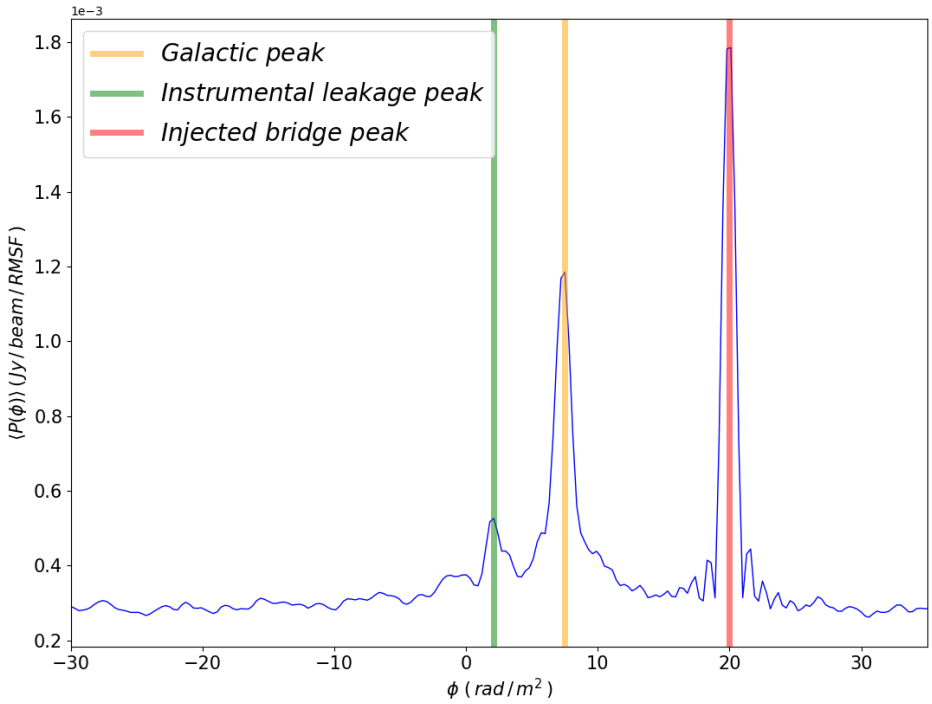

Figure 4.19: Faraday spectrum of the average polarized intensity $\langle P(\phi) \rangle$ over the bridge region (Fig. 4.17), obtained with the data where the bridge emission model has been injected. As for the previous spectra, instrumental and galactic peaks are present. This time, at $\phi \sim 20$ rad/m^2, there is an additional peak caused by the bridge emission that has been injected in the data. From this result, one can see that if the bridge had a high polarization fraction a clear peak should be visible in the Faraday spectrum, always assuming a simple Faraday screen that causes the Faraday rotation.

4.3.4 Constraints on the depolarization mechanisms

There are three main depolarization processes presented in Sec. 3.2.1 that can account for the non-detection of the bridge in polarization: (i) differential Faraday rotation, (ii) internal Faraday dispersion, and (iii) external Faraday dispersion.
As explained in Sec. 4.3.3, we are considering that shocks occur on scales much smaller than the bridge, and so we can assume that they are located behind it. Giving this configurations, we have considered the case of an external Faraday screen with the addition of a *turbulent* magnetic field that originates the depolarization reducing the polarized flux fraction. Consequently, if such depolarization process occurs, the intrinsic polarization flux p_0 experiences a modification given by Eq. 3.16:

$$P = p_0 \, e^{-2\sigma_{RM}^2 \lambda^4} \, e^{2i(\Psi_0 + RM\lambda^2)}.$$

As one can see, the depolarization is caused by an exponential factor that depends on the term σ_{RM} and the considered wavelength.
In particular, we are interested in the σ_{RM} term. In fact, because the magnetic field is

not uniform, different degrees of Faraday rotation occur along the line of sight causing different changes in the degree of polarization, which lead to an overall depolarization of the radiation. Such differences in the magnetic field, and then in the Faraday rotation, can be seen as differences in RM values of the medium along the line of sight. It means that some regions cause modifications on the radiation that can be described with a certain RM value, while others regions give rise to changes described by other RM values. Therefore, there is dispersion around a mean RM value across the source in the sky, which is parameterized by σ_{RM}.
Hence, the higher σ_{RM} the stronger the depolarization.

To constrain the value of σ_{RM}, we generated a simulated bridge emission, with the same intrinsic Faraday rotation as before but, this time, we also inserted the depolarization factor $e^{-2\sigma_{RM}^2\lambda^4}$.
As σ_{RM} increases, the observed $|P|$ decreases, i.e. the depolarization becomes stronger. At a certain point, σ_{RM} reaches a value that the depolarization will become so strong that the polarized emission of the bridge can no longer be detected in the Faraday spectrum (i.e. no peak in the FDF). As σ_{RM} is related to the magnetic field (See 3.2.1), constraining σ_{RM} will leads to constrain the magnetic field.

To generate the simulated bridge emission, accounting also for the depolarization, we used Eq.s (4.7) (4.8) with the addition of the exponential depolarization term. In particular, because the depolarization is simply parameterized by a multiplicative term, the simulated signals Q and U of the polarization vector, P, become:

$$Q = (Q_0 \cos 2\theta - U_0 \sin 2\theta) e^{-2\sigma_{RM}^2\lambda^4} \tag{4.9}$$

$$U = (U_0 \cos 2\theta + Q_0 \sin 2\theta) e^{-2\sigma_{RM}^2\lambda^4} \tag{4.10}$$

In addition to the exponential depolarization factor, another difference between Eq. (4.9)–(4.10) and Eq. (4.7)–(4.8), is in the RM term.
This time, we did not assume a fixed value of RM as before ($RM = 20$ rad/m^2) simply because, introducing the σ_{RM} parameter, we are considering a dispersion around the mean RM. Therefore, to be self-consistent with our assumptions, when we created the synthetic images, we inserted such intrinsic scatter due to magnetic field inhomogeneities. Specifically, for every pixel in each image at a certain frequency (or wavelength), we computed its Q and U signals using Eq. (4.9)-(4.10) and as RM value we inserted 20 plus a scatter, due to σ_{RM}. Such scatter has been determined by random sampling a value from a Gaussian distribution with mean 0 and standard deviation σ_{RM}.

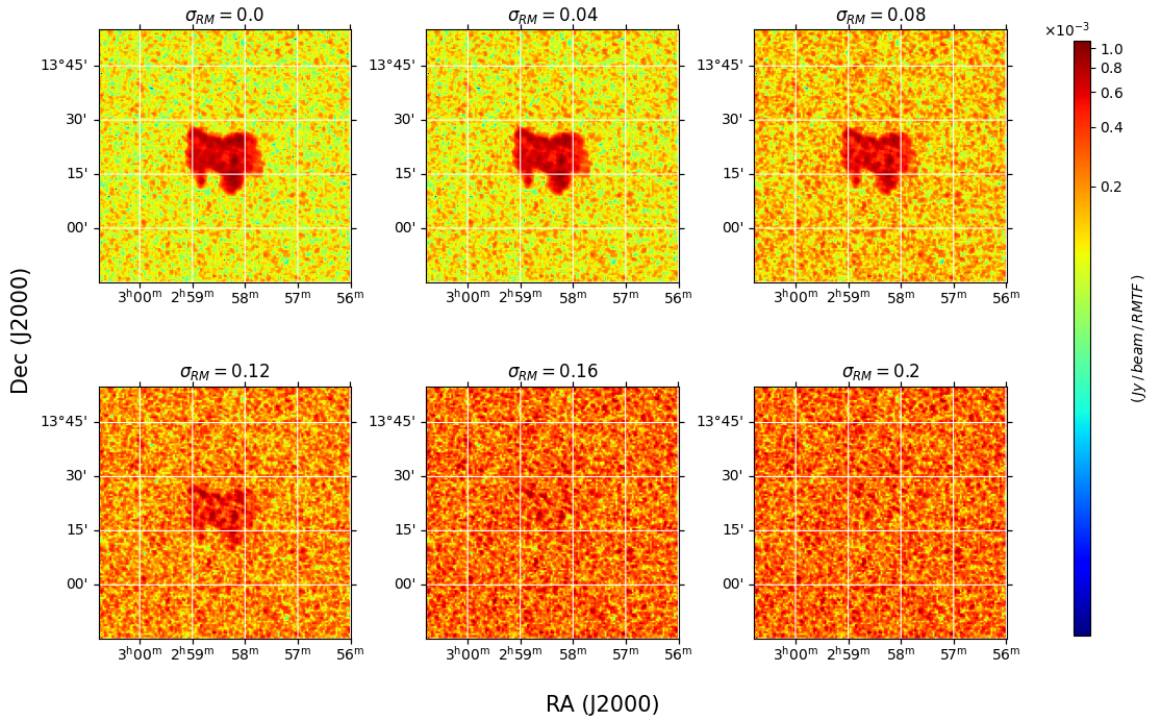

Figure 4.20: Different Faraday spectrum maps obtained from data where injected the bridge emission varying the value of σ_{RM}, i.e. changing the bridge degree of polarization. It is evident that the bridge peak decrease when increasing the depolarization until completely disappears.
The values of σ_{RM} are in the range 0 rad/m^2, in the upper left image, to 0.2 rad/m^2, in the lower right, with steps of 0.04 rad/m^2.

As in Sec. 4.3.3, we generated 100 Q and U images and then computed the same steps. We injected the images in the original data, we imaged them and finally performed the RM synthesis to recover for the polarized emission.
As expected we found a progressive decrease of the bridge peak in the Faraday spectrum when increasing σ_{RM}. A clear idea of what happens to such peak when increasing the σ_{RM} can be seen in Fig. 4.20 and Fig. 4.21.

Therefore, there is a minimum value of σ_{RM} that generates too much depolarization on the peak and make it disappear into the Faraday spectrum.
In order to recover for such lower limit on σ_{RM}, we compared the FDF of data where the bridge emission has been injected, with the FDF of real data from the observations. We considered the integral of the FDF in the proximity of the bridge peak ($\phi_{\text{bridge}} =$ 20 rad/m^2, then we accounted from $\phi = 15$ rad/m^2 to $\phi = 25$ rad/m^2), both for the "injected data" and for the real one. Then, we defined the following quantity:

$$P_{exc} = \frac{\int_\phi P_{inj}(\phi)\, d\phi - \int_\phi P_{real}(\phi)\, d\phi}{\int_\phi P_{real}(\phi)\, d\phi} \tag{4.11}$$

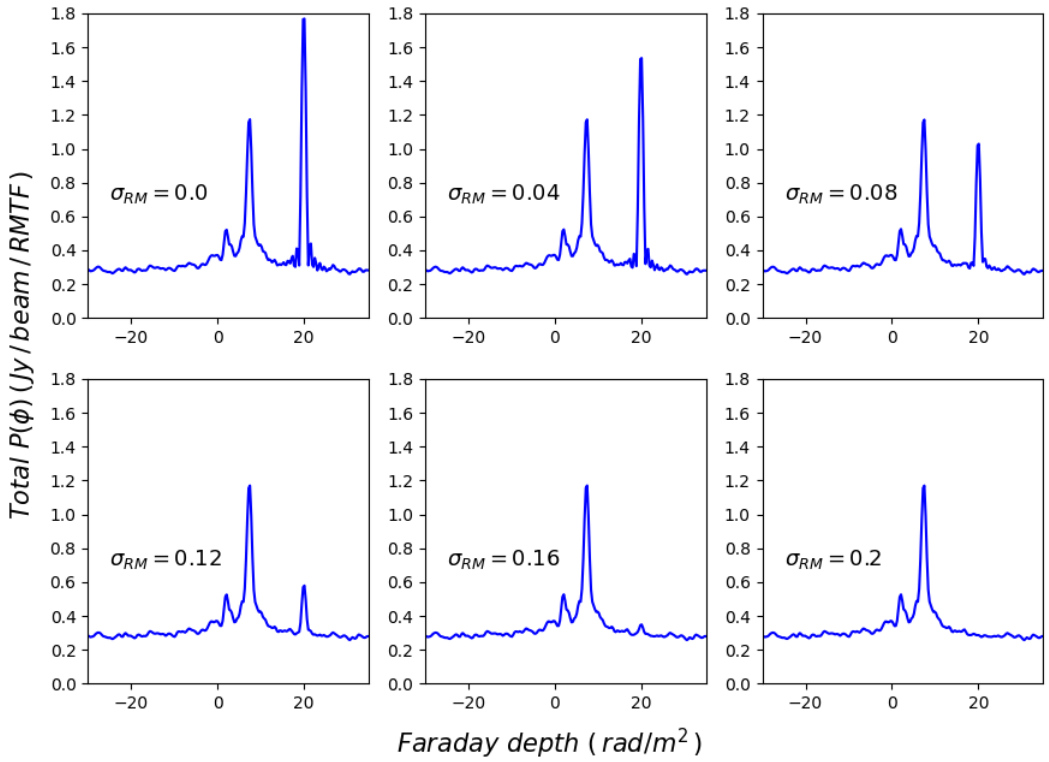

Figure 4.21: Different Faraday spectra of the total polarized intensity of the bridge region, obtained from data where injected the bridge emission varying the value of σ_{RM}, i.e. increasing the degree of depolarization. It is evident that the bridge peak decreases when increasing the depolarization until completely disappears.
The σ_{RM} steps are the same than in Fig. 4.20

Where $P_{inj}(\phi)$ is the polarized intensity in the Faraday spectrum of the data with the injected bridge emission and $P_{real}(\phi)$ is polarized intensity of the real data. This is a quantity that allows us to determine the relevance of the injected bridge emission over the real data, indicating how the emission excess, due to the bridge injection, is important with respect the observed emission. We noticed that such dimensionless quantity is well constrained between two finite values:

$$\lim_{\sigma_{RM}\to 0} P_{exc} = l < \infty \tag{4.12}$$

$$\lim_{\sigma_{RM}\to \infty} P_{exc} = 0 \tag{4.13}$$

These two limits tell us that $P_{exc}(\sigma_{RM})$ is a monotonically decreasing function. This is another evidence that there is a threshold σ_{RM} (σ^*) for which $P_{exc}(\sigma_{RM})$ differs from zero by a negligible value, i.e. for σ_{RM} grater than σ^* the bridge cannot be detected. Therefore, for values of σ_{RM} greater than this limit, the reproduced FDF is equal the one from the observations, i.e. σ^* represents a σ_{RM} lower limit.

Computing the Faraday spectra for different cases of depolarized bridge injection, we studied the trend of the integral of injected data $\left(\int_\phi P_{inj}(\phi)\, d\phi\right)$ as a function of σ_{RM}. Moreover, we compared these integrals with the integral of the FDF from the real data in order to see when the bridge becomes completely depolarized. Finally, we also calculated P_{exc} for different values of σ_{RM} and studied its trend too. These quantity are plotted in Fig. 4.22, where $\Sigma = \int_\phi P(\phi)\, d\phi$.

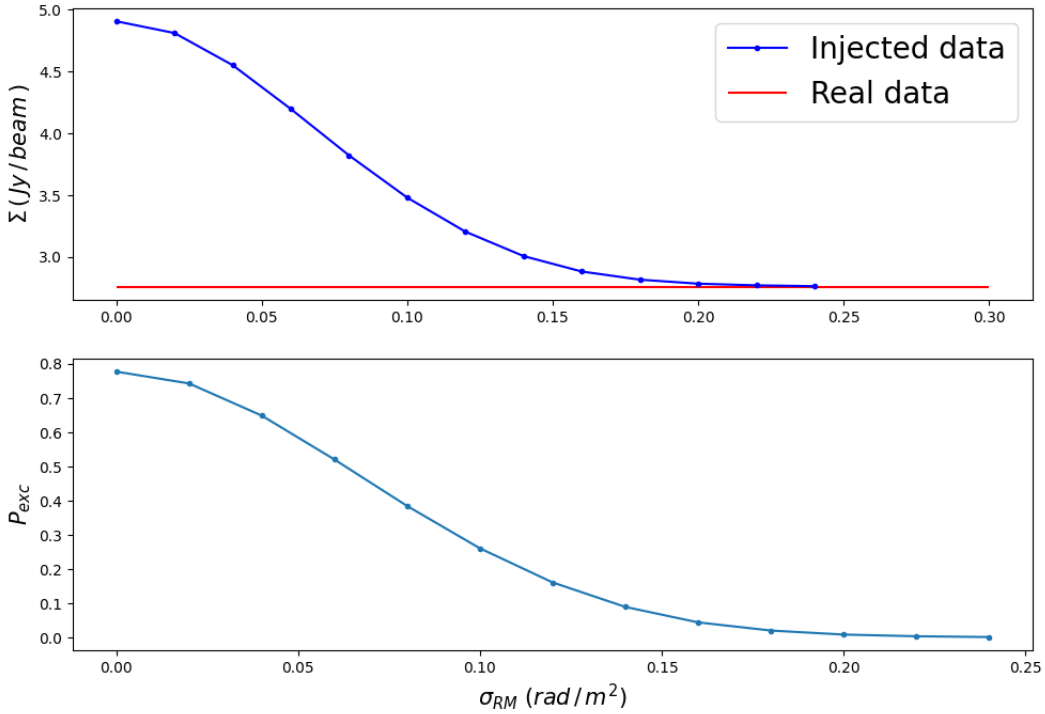

Figure 4.22: *Top*: Trend of the FDF integral of the polarized bridge emission with σ_{RM}, compared with the same integral of the real data FDF spectrum $\left(\Sigma = \int_\phi P(\phi)\, d\phi\right)$. Both the injected data and the real data FDF integral are shown. Again, it is clear that the bridge peak, in the case of no depolarization, is predominant in the FDF spectrum. *Bottom*: Trend of P_{exc}, (Eq. 4.11) for different values of σ_{RM}. Because of its definition, we can see its decreasing trend with σ_{RM}, until becomes ~ 0 when there is a sufficiently high depolarization.
In both plots the σ_{RM} values are in the range $0 - 0.24$ rad/m^2 and are sampled every 0.02 rad/m^2.

As expected, the emission from the bridge gets more and more depolarized increasing σ_{RM}, leading to a reduction of $P_{exc}(\sigma_{RM})$. The real data integral is, of course, constant. We can clearly see, as suggested by Fig. 4.21, that at a certain point the two integrals become identical. This means that the depolarization has become so important that the bridge peak contribution to the overall polarized emission is negligible, and the two FDF are identical.

Once obtained these results, we constructed the cumulative distribution function $F(P_{exc} < s)$ and normalized it over the chosen interval. What we obtain is plotted in Fig. 4.23. Again, the contribution from P_{exc} becomes more and more negligible for

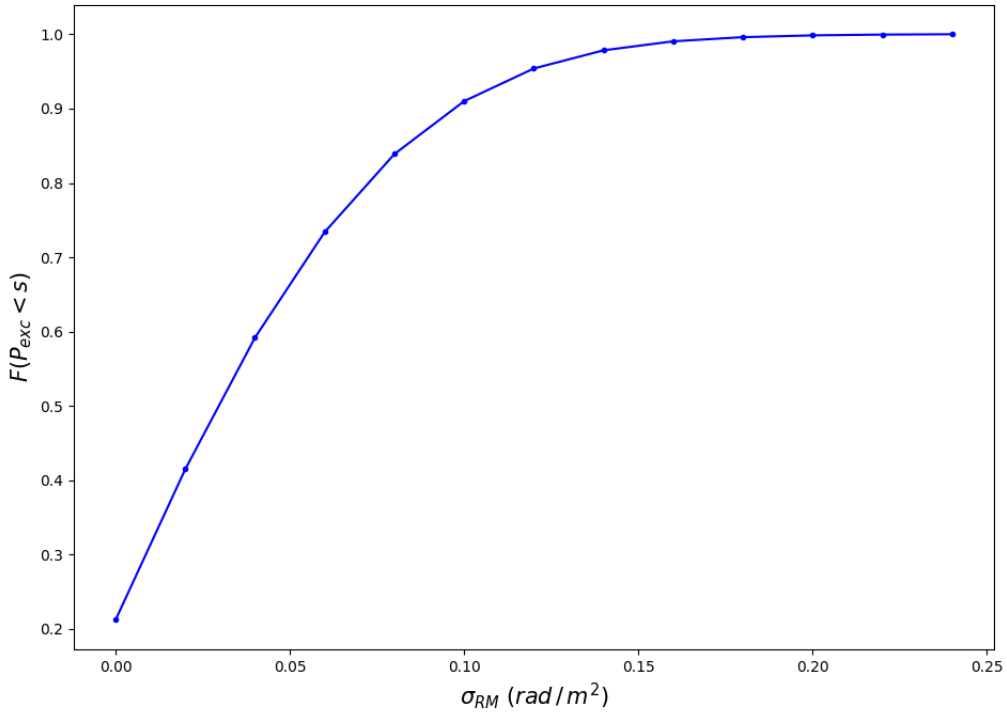

Figure 4.23: Normalized cumulative distribution of P_{exc} as a function of σ_{RM}.

higher values of σ_{RM}.
We found that $F(P_{exc} < s) = 95\%$ for $s = 0.17$, which corresponds to $\sigma^* = 0.12$ rad/m^2, and with an increasing probability for $\sigma_{RM} > 0.12$ rad/m^2. In other words, if the value σ_{RM} were smaller than 0.12 rad/m^2 we would have detected a peak in the Faraday spectrum with a 95% significance (or greater). Because we did no detect such FDF peak, we can set 0.12 rad/m^2 as lower limit on σ_{RM}.

The next step will be to use this lower limit on σ_{RM} to put constraints on the magnetic field (See 3.2.1).

4.4 Simulations analysis

As explained in Sec 3.2.1, the magnetic field is related to σ_{RM}. Therefore, it is possible to obtain a value of σ_{RM} assuming a model for the field. Here we assumed the magnetic field model provided by Govoni et al. (2019) (see Sec. 4.2). In particular, we analyzed these simulations in order to obtain a value of σ_{RM} in the simulated bridge region, and

to compare it with the lower limit obtained above.
To this purpose, we exploited the simulated 3D cube of both density and magnetic field. In the simulations, the bridge is seen in projection along the z-axis, hence, we considered only the B_z cube for the calculation of RM values.

First, we identified a possible bridge region inside the cluster studying the density cube from the simulations. We selected a field region with the same angular dimension as the one selected during the LOFAR data analysis (Fig 4.17, Sec 4.3.3) in order to take in account only for the bridge region properties (n_e and B_z). Such region is highlighted in red in Fig. 4.24.
Once defined the bridge region, we have produced a RM map of the simulation, using the density map and the z-axis magnetic field component. We computed for each pixel of the bridge region the value of ϕ using Eq. (3.10):

$$\phi \simeq 0.81 \int_0^L n_e \, \boldsymbol{B} \cdot d\boldsymbol{l} \left[\frac{\text{rad}}{\text{m}^2}\right]$$

In practice, we performed the integral above for each pixel, integrating over the whole line of sight, i.e. along all the density cube (~ 10 Mpc). Finally, we have convolved the simulated RM map with a Gaussian function having the FWHM equal to the beam (107" = 144 kpc) to take into account the beam depolarization. The obtained RM map is shown in Fig. 4.25.
From this analysis we obtained, over the bridge region, an average Faraday depth of 6.4 rad/m^2 and a σ_{RM} of 13.9 rad/m^2. The second result is consistent with our limit of $\sigma_{RM} > 0.12$ rad/m^2. Therefore, from the simulations we do not expect to observe the bridge polarized emission because of the high depolarization [5].

Using the simulations, we can derive the average magnetic field along the bridge extension. To do this, we have assumed that the magnetic field in each pixel is isotropic, therefore, $B_x = B_y = B_z$ and then $|\boldsymbol{B}| = \sqrt{3}\, B_z$. For each layer of the magnetic field cube, we computed the density-weighted average magnetic field intensity. Then we computed the average magnetic field of each layer, obtaining a global mean magnetic field intensity of 0.016 μG.

Knowing both σ_{RM} from the observations and from the simulation, the recently derived magnetic field intensity can be used to constrain the real magnetic field of the bridge.

[5] The average RM is 6.4 rad/m^2. Hence, accounting for the Galactic emission at $\phi_{gal} \sim 7.5$ rad/m^2, in the FDF spectrum the bridge emission should have been observed at $\phi \sim 6.4 + 7.5 \simeq 14$ rad/m^2. In such spectrum region the noise is similar to the noise at $\phi = 20$ rad/m^2 which is the chosen value for our injection-analysis

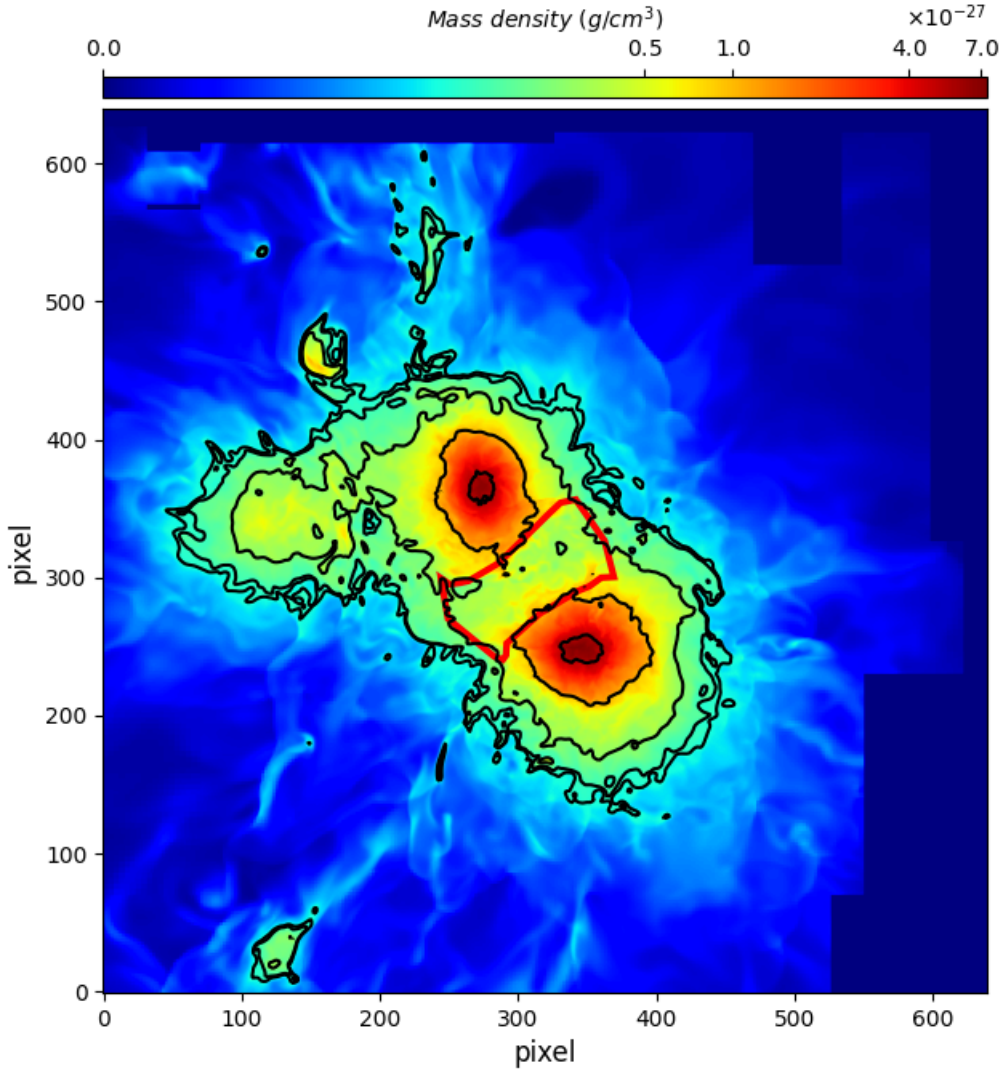

Figure 4.24: Central slice of the cube density from simulations. Moving towards the density cube, the average density of the medium initially increase, indicating the presence of the cluster pair, then starts to decrease until reaching 0 in the last slice, showing the ending regions of the cluster pair. As so, we selected the central slice of the cube as a best indicator of the density distribution.
The density contours are at 1, 1.24, 2.61, 10.3, 53.5×10^{-28} g/cm^3.
In red, is also highlighted the region selected as the bridge region for the simulation.

Let us consider the definition of σ^2_{RM} of an image:

$$\sigma^2_{RM} = \frac{\sum_{i=1}^{N} (RM_i - \langle RM \rangle)^2)}{N} \tag{4.14}$$

where RM_i is the RM of the i-th pixel, $\langle RM \rangle$ is the average RM of the map and N is the total pixel number that we are considering.
From Eq. (4.14) we can see that, if every RM_i of the map increase of a factor "X",

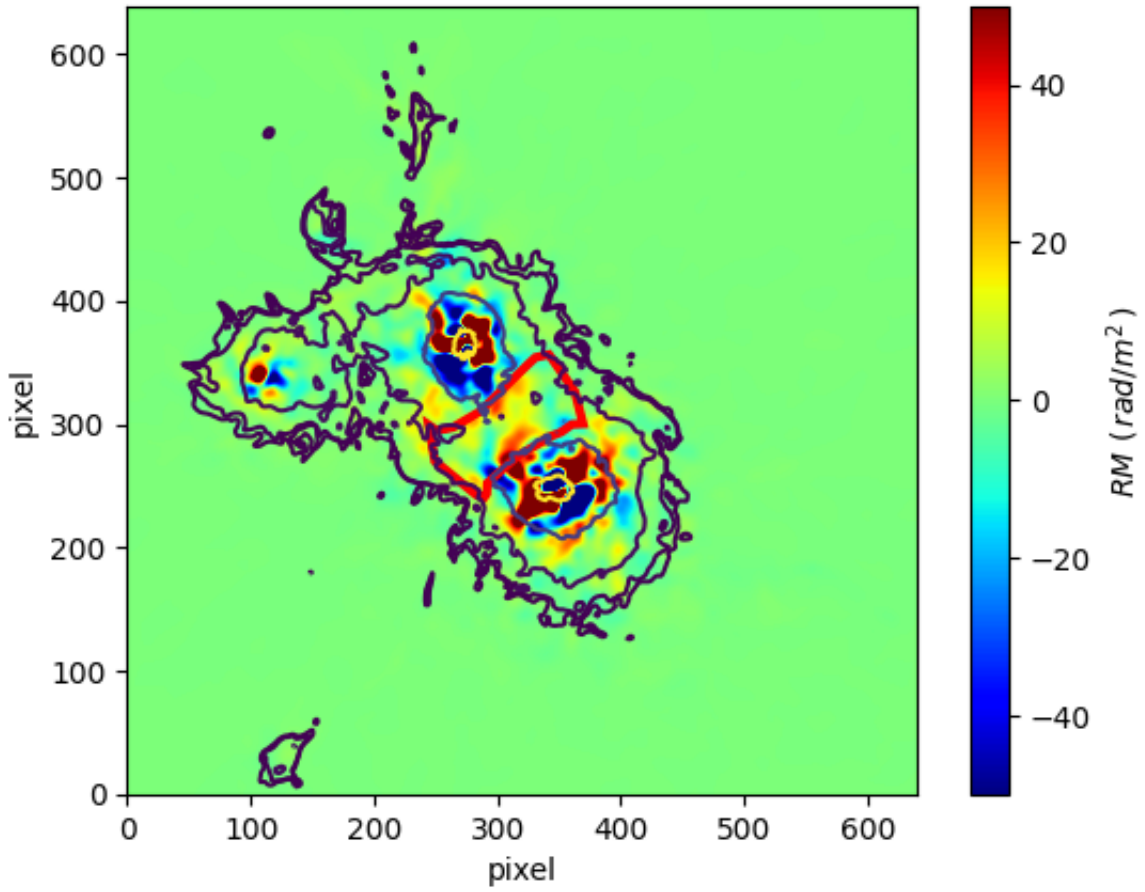

Figure 4.25: *RM* map obtained using the simulation data of density and magnetic field component along the line of sight. The contours overlapped are the density contours in Fig 4.24, while the selected simulation bridge region is highlighted in red.

then the $\langle RM \rangle$ increases by the same factor and σ^2_{RM} becomes $X^2\sigma^2_{RM}$. Therefore, σ_{RM} increases by a factor X, $X\sigma_{RM}$.
If the global RM, or ϕ, increases of a factor "X", it means that the integral in Eq (3.10) increases by the same factor. Therefore, in order to have an increment of such quantities, or the density or the magnetic field intensity should become higher (once fixed the depth of the medium).
In literature (e.g. Bonjean et al., 2018; Akamatsu et al., 2017, and reference therein), the density estimates in the cluster pair A399–A401 are all consistent with the density found in the used simulations, $\sim$ few 10^{-4} cm^{-3}. Thus, our density simulations are good models of the real gas density distribution (apart from the estimate provided by Hincks et al. 2021 that we will discuss separately). As so, when we calculate RM and σ_{RM} from simulations, the differences between these and observational results can be attributed to differences in the magnetic field intensity along the line of sight. In particular, if we focus on σ_{RM}, naming the observational lower limit σ_o and the model

prediction σ_m, we have that:

$$\sigma_o = X\,\sigma_m \tag{4.15}$$

Following the previous considerations, this difference of factor "X" in σ_{RM}, results in a difference, of the same factor, in $|\boldsymbol{B}|$:

$$B_o = X\,B_m \tag{4.16}$$

where B_o is the real magnetic field intensity, and B_m is the one from simulations. Actually, we can not recover the exact value of "X", in fact, having an upper limit on σ_o results on deriving an upper limit also on "X":

$$X > \frac{\sigma_o}{\sigma_m} = \frac{0.12}{13.9} = 0.009 \tag{4.17}$$

Now, we can use this value to recover a *lower* limit for B_o from Eq (4.16):

$$B_o > 0.01 \times B_m = 0.009 \times 0.016 = 0.14 \text{ nG} \tag{4.18}$$

Thus, the average magnetic field along the bridge region, which turbulence causes a completely depolarization of the bridge polarized emission, has intensity > 0.14 nG.

Low gas density distribution

In order to obtain the previous limit on $|\boldsymbol{B}|$ we assumed that our simulations provided a good approximation of the real gas density. As reported in the previous section, the density of the bridge region in our simulations is about few 10^{-4} cm^{-3}, which is in good agreement with most of the density estimates found in literature. However, a recent work of Hincks et al. (2021) reported an average bridge density of $(0.88 \pm 0.24) \times 10^{-4}$ cm^{-3}. With such low density, the simulated bridge $\langle RM \rangle$ and σ_{RM} values will change, causing changes also in the magnetic field limit. In particular, with an average density equal to half of the one from simulations, the bridge magnetic field lower limit would become 0.28 nG.

4.5 Instrumental and Galactic peak injection

Until now, we have considered only the case of a bridge peak, in the Faraday spectrum, at values of ϕ where there was only noise-like signal. However, there are other two possibilities.

In fact, the FDF bridge peak could lie in the proximity of the other two spectrum peaks, the instrumental peak ϕ_{instr} and the galactic peak ϕ_{gal}. In these cases the peak

detection would be different and then, also the lower limits could change.
Hence, we performed the same analysis described in the previous section, with the only difference that we have injected the bridge using the RM parameter of Eq (3.16) equal to 2.1 rad/m^2 and 7.5 rad/m^2, which were the two Faraday depth values of instrumental and galactic peak.

Starting from the galactic peak case, we operated the injection of the rotated (due to $RM = 7.5$ rad/m^2) and depolarized (due to σ_{RM}) bridge emission, varying the values of σ_{RM} from 0 to 0.24 rad/m^2 with steps of 0.03 rad/m^2. Then, we imaged the data, performed the RM synthesis, recovered the Faraday spectra in the bridge region and calculated the $P_{exc}(\sigma_{RM})$ quantity for each case of σ_{RM} (Fig 4.26). Finally we

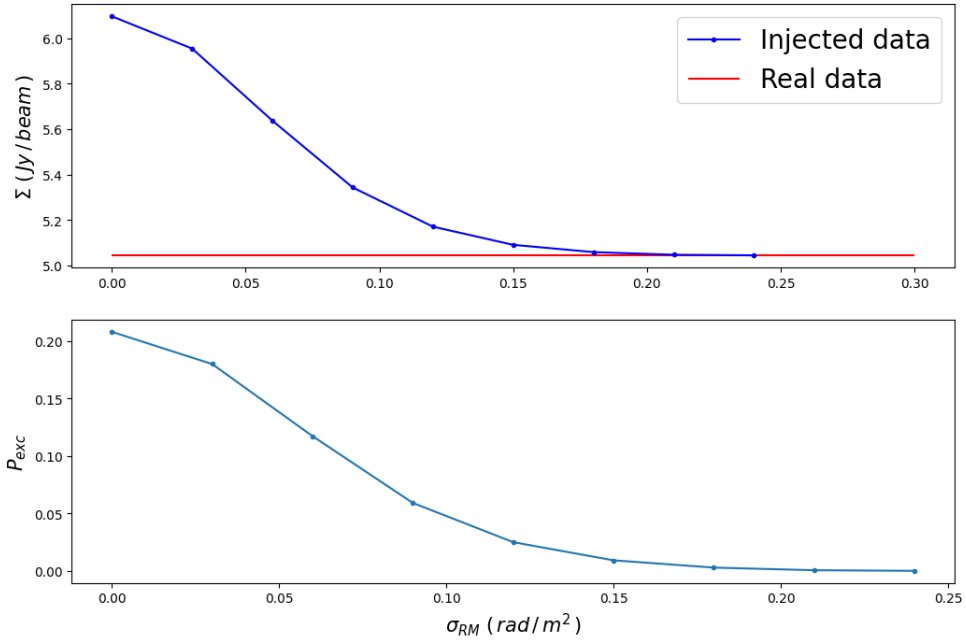

Figure 4.26: Trend of the FDF integral of the polarized emission, in ϕ-range $2.5 - 12.5$rad/m^2, when increasing σ_{RM}, compared with the same integral of the real data FDF spectrum. In the *upper* plot both the injected data, with the bridge injection at $\phi = \phi_{gal}$ and the real data FDF integral are shown. In the *lower* panel, instead, is shown the previously introduced P_{exc} quantity. Because of its definition, we can see its decreasing trend with σ_{RM}, until, becomes ~ 0 when there is a sufficiently high depolarization.
σ_{RM} values are in the range $0 - 0.24$ rad/m^2 and are sampled every 0.03 rad/m^2.

constructed the cumulative distribution (Fig 4.27), $F(P_{exc} < s)$, finding that $F(P_{exc} < s) = 95\%$, for $s = 0.05$, which corresponds to $\sigma^* = 0.1$ rad/m^2. This result sets the limit of σ_{RM} to a lower value than one obtained before.
Such outcome was expected because the *real* Faraday spectrum, in the region where we have injected the bridge, presents a higher emission, due to our Galaxy, than in the

previous case. This implies that the factor $\int_\phi P_{real}(\phi)\, d\phi$, in Eq (4.11), is "high" and so the injected bridge emission, compared with the real FDF, will be less important than before. This can be seen comparing the second plot of Fig. 4.22 and Fig. 4.26. We can clearly see that for $\sigma_{RM} = 0$ rad/m^2, the excess due to the bridge is roughly the 80% of the real data emission in Fig. 4.22 while is about 20% in Fig. 4.26. Therefore, in this case, because the bridge emission is "less" important with respect the real FDF, it becomes negligible at lower values of σ_{RM}.

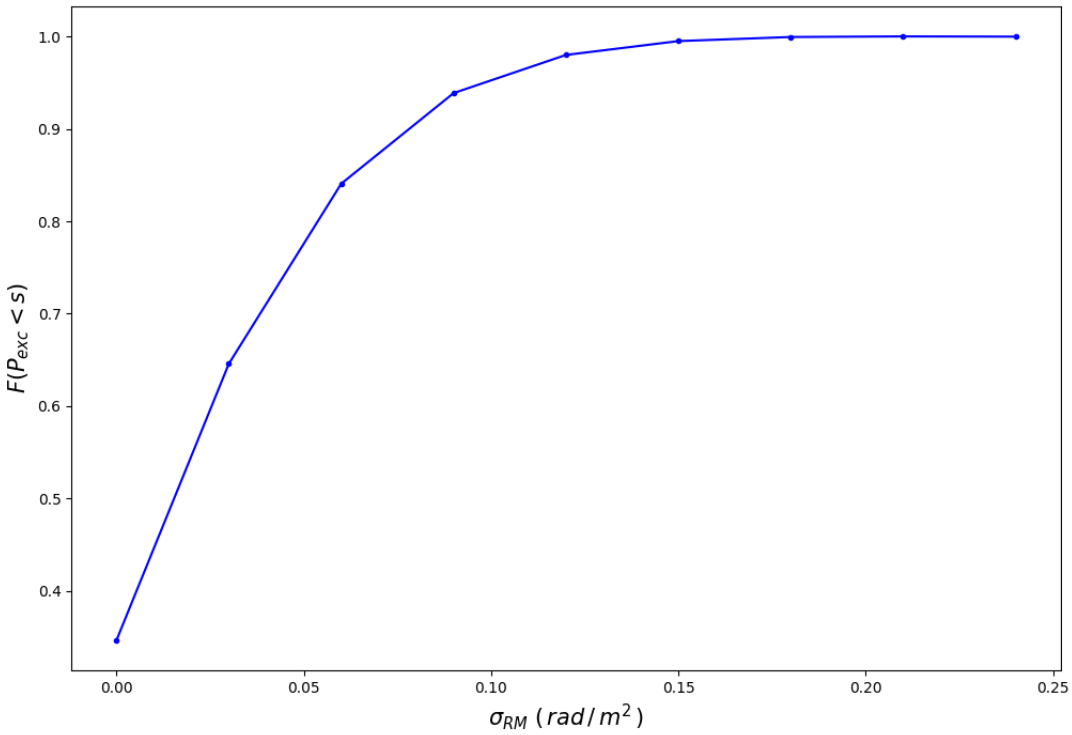

Figure 4.27: Normalized cumulative distribution function of $P_{exc}(\sigma_{RM})$, in the case of bridge injection at $RM = 7.5$ rad/m^2.

Performing the same analysis injecting the bridge emission at $\phi = \phi_{instr}$, the obtained results were roughly the same that for the case with $RM = 20$ rad/m^2, with a limit on $\sigma_{RM} \gtrsim 0.12$ rad/m^2 which corresponds to a $P_{exc}(\sigma_{RM}) \sim 0.1$. This result was expected as the peak corresponding to the instrumental leakage is not as prominent as the Galactic peak.

In the same way as in Sec 4.4, once obtained the limit on σ_{RM}, we can put limit on the magnetic field strength. In the case of injection in the proximity of ϕ_{instr}, the limit on the magnetic field would be equal to the one provided in Sec. 4.4 because of the equal limit on σ_{RM} ($B_o > 0.14$ nG).
Instead, for the case of bridge injection at ϕ_{gal}, the result would be slightly different.

In fact, if we recompute all calculations made in Sec. 4.4 with a σ_o of 0.1 rad/m^2, the resulting lower limit on the magnetic field would be $B_o > 0.11$ nG.

5. Summary and Conclusions

In this thesis we presented a radio polarization study of the merging cluster pair Abell 399–Abell 401. This object has been recently studied by Govoni et al. (2019) through LOFAR observations at $\sim$ 140 MHz, showing the first evidence of a diffuse radio emission (*radio bridge*) connecting two galaxy clusters. This emission is a signature of energetic particles and magnetic fields, which are trivial to be explained on Mpc scales.
They suggested a shock-driven emission model, where multiple weak shocks, originated by the clusters motion during the merging event, re-accelerate pre-existing population of electrons originating a radio emission with a high ($\sim$ 70%) polarization fraction (Sec. 4.2).

We analyzed the polarized radio emission of the bridge region imaging at 6", 20" and 107" resolution. Images at 6" and 20" were performed in order to investigate the presence of polarized sources co-spatial with the bridge. Such analysis showed a number of compact sources in the field, but did not detect the bridge emission. Instead, with images at 107" resolution (Fig. 4.9) we detected the bridge emission.
We analyzed the polarization emission at 6" 20" and 107" in the frequency range $120 - 168$ MHz. We performed the RM synthesis for images at 20" resolution finding a number of compact polarized sources in the target field (Fig. 4.10) but not in the bridge region, along with the Galactic polarized emission (Fig. 4.12) presents almost in the whole observed field. Performing the RM analysis on the images at 107" resolution we detected no significant polarized emission coming from the bridge (Fig. 4.14).

Hence, we investigated whether a bridge polarized emission like the one predicted by the model proposed by Govoni et al. (2019), should have been detected or not. We did this by synthesising model images of a simulation-like bridge polarized emission, for the whole frequency range of the observation, and Faraday-rotated by an RM of 20 rad/m^2. Then, we injected such emission inside the real data and re-computed the imaging and RM analysis. This showed that, if the bridge emission was like the one from the model, we should be able to observe the polarized peak in the FDF spectrum with a high significance (SNR $\sim$ 180). Therefore, we inferred that some depolarization mechanisms was occurring (See 3.2), implying, also, the presence of a turbulent mag-

netic field in the inter-cluster region.

Assuming the configuration of thin shocks, with respect the bridge size, illuminating the bridge from behind, we explored the depolarization case of an external Faraday screen with a turbulent magnetic field. We re-computed the same injection-steps did before, but injecting inside the data an emission progressively more depolarized, i.e. with an increasing σ_{RM} parameter in the "depolarization term" (See Eq. 3.16). From this analysis emerged that, as expected, increasing the value of σ_{RM} the bridge polarized peak in the FDF spectrum disappears (Fig 4.21).

To assess with a given confidence level the value of σ_{RM} that would make the bridge undetectable by our observations, we defined the quantity $P_{exc}(\sigma_{RM})$, Eq (4.11). It indicates the importance of the injected bridge emission, with respect the real detected emission, for different values of σ_{RM}. Computing the cumulative distribution of $P_{exc}(\sigma_{RM})$, we have been able to find a limit on σ_{RM} (0.12 rad/m^2) above which the bridge emission could not have been detected. Therefore, because of lack of bridge polarized emission in the real data, we put a lower limit on the σ_{RM} observed bridge region, $\sigma_o > 0.12$ rad/m^2.

Since σ_{RM} is related to the magnetic field, it is possible to recover a value of $|\mathbf{B}|$ comparing simulation and observational results. Hence, using simulation models, we analyzed the density and line of sight magnetic field component (B_z). With these two quantities we computed an RM map of the simulated field (Fig. 4.25) and analyzed it in a region similar to the real data bridge region (Fig. 4.24 and Fig. 4.17). From this model analysis we found $\langle RM \rangle \sim 6.4$ rad/m^2 and $\sigma_{RM} = 13.9$ rad/m^2. Comparing the results of the model (σ_m) and the observational (σ_o) RM dispersion allowed us to find a relation between the model bridge magnetic field intensity (B_m) and the real magnetic field intensity of the bridge region (B_o). In particular, having a lower limit on σ_o, has led to a lower limit on the bridge region magnetic field intensity, $B_o > 0.14$ nG (or > 0.28 nG if using the lower bridge density provided by Hincks et al. 2021).

For completeness we have also considered the case that the bridge RM was the same than the Galactic or instrumental Faraday depth in the FDF spectrum. In the latter case, we found no difference with our lower limit on σ_{RM} and so also on the bridge magnetic field. Instead, for the Galactic case, due to the higher relevance of the Galactic peak in the Faraday spectrum, we found a slightly difference on the limit on σ_{RM}). This has lead to a different constraint on the magnetic field intensity, $B_o > 0.11$ nG.

Our result is in agreement with both recent works from Locatelli et al. (2021)

and Vernstrom et al. (2021), who derived limits on the magnetic field of inter-cluster filaments using radio and stacked X-ray emission.
As explained in Sec. 1.2.2, studies like this one, which set magnetic field limits in regions outside the cluster environment, would potentially offer another method to constrain the primordial magnetic field and also to distinguish between field amplification models. Fig. 5.1 provide a schematic overview of different models of magnetic field origin and their range of uncertainties in the different seeding modes. It tells us roughly that, until filaments the main contribute to the magnetic field strength comes from primordial origin. Therefore, measuring magnetic field in low density regions allows to constrain such primordial-originated field. Instead, at higher values of overdensities, i.e. in denser regions, the magnetic field originated by astrophysical objects becomes more important, until becoming the main one on cluster scale.

Given the definition of *critical density* $\rho_c = \frac{3H^2}{8\pi G}$, where H is the Hubble constant

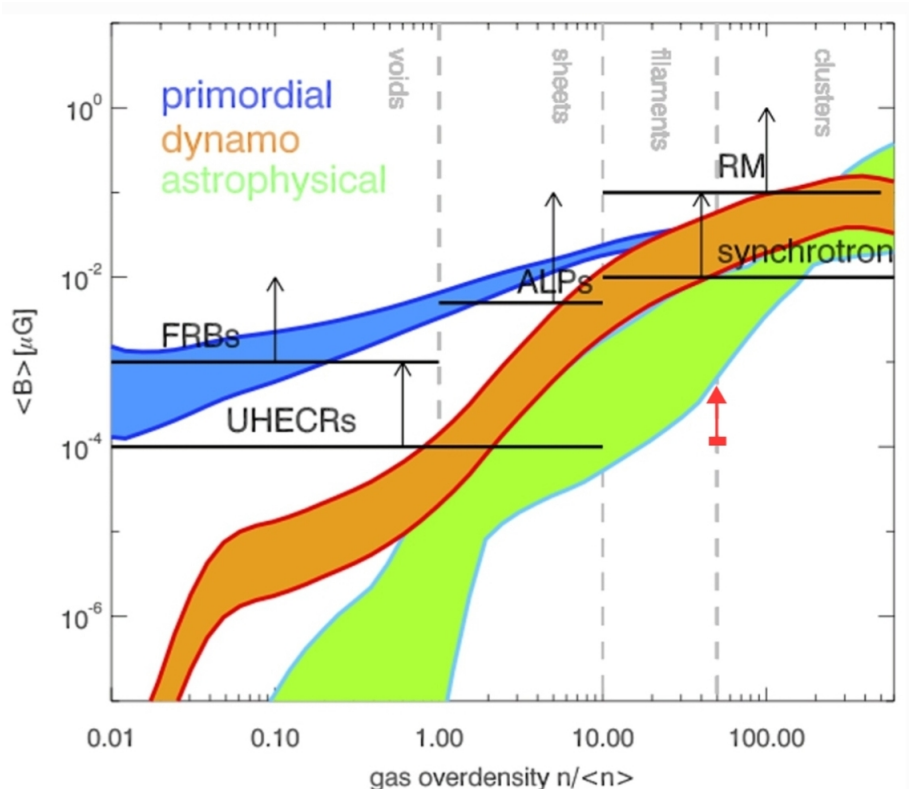

Figure 5.1: Distribution of extragalactic magnetic fields predicted by simulations of Vazza et al. (2017) and the approximate regime where different observational effects can measure them. In red our magnetic field lower limit.

and G is the gravitational constant, we used the cosmological parameter provided in Vazza et al. (2017), $H_0 = 67.8$km/s/Mpc (assuming H=H_0 due to the proximity of the A399-A401 pair), $\Omega_m = 0.2602$ and $\Omega_b = 0.0478$, to derive an approximate mean density of $8.8 \times 10^{-6}\ cm^{-3}$ for the bridge region. Assuming the bridge mean density

suggested by (Bonjean et al., 2018) of $\sim 4.3 \times 10^{-4}\ cm^{-3}$, we derived an estimate for the bridge overdensities of ~ 50. The red arrow indicates, approximately, the lower limit provided by this work in a filamentary-like region. However, the new technique that we are proposing will be able to set stringent limits once deeper observations and/or on a large λ^2 interval will become available.

With this work, we observationally proved that a depolarization process is required to justify the emission predicted by the shock model. Investigating the case of depolarization caused by an external Faraday screen suggested the presence of a turbulent magnetic field inside the bridge region. From this study, we were also able to derive lower limit for this field, providing the first magnetic field constraint on an inter-cluster region.

Our results provided new hints about the importance of low and high frequencies studies on such newly discovered objects, in order to better understand their origin and constrain the origin of our Universe.

Bibliography

Ahumada, R., Prieto, C. A., Almeida, A., Anders, F., Anderson, S. F., Andrews, B. H., Anguiano, B., Arcodia, R., Armengaud, E., Aubert, M., Avila, S., Avila-Reese, V., Badenes, C., Balland, C., Barger, K., Barrera-Ballesteros, J. K., Basu, S., Bautista, J., Beaton, R. L., Beers, T. C., Benavides, B. I. T., Bender, C. F., Bernardi, M., Bershady, M., Beutler, F., Bidin, C. M., Bird, J., Bizyaev, D., Blanc, G. A., Blanton, M. R., Boquien, M., Borissova, J., Bovy, J., Brandt, W. N., Brinkmann, J., Brownstein, J. R., Bundy, K., Bureau, M., Burgasser, A., Burtin, E., Cano-Díaz, M., Capasso, R., Cappellari, M., Carrera, R., Chabanier, S., Chaplin, W., Chapman, M., Cherinka, B., Chiappini, C., Doohyun Choi, P., Chojnowski, S. D., Chung, H., Clerc, N., Coffey, D., Comerford, J. M., Comparat, J., da Costa, L., Cousinou, M.-C., Covey, K., Crane, J. D., Cunha, K., Ilha, G. d. S., Dai, Y. S., Damsted, S. B., Darling, J., Davidson, James W., J., Davies, R., Dawson, K., De, N., de la Macorra, A., De Lee, N., Queiroz, A. B. d. A., Deconto Machado, A., de la Torre, S., Dell'Agli, F., du Mas des Bourboux, H., Diamond-Stanic, A. M., Dillon, S., Donor, J., Drory, N., Duckworth, C., Dwelly, T., Ebelke, G., Eftekharzadeh, S., Davis Eigenbrot, A., Elsworth, Y. P., Eracleous, M., Erfanianfar, G., Escoffier, S., Fan, X., Farr, E., Fernández-Trincado, J. G., Feuillet, D., Finoguenov, A., Fofie, P., Fraser-McKelvie, A., Frinchaboy, P. M., Fromenteau, S., Fu, H., Galbany, L., Garcia, R. A., García-Hernández, D. A., Oehmichen, L. A. G., Ge, J., Maia, M. A. G., Geisler, D., Gelfand, J., Goddy, J., Gonzalez-Perez, V., Grabowski, K., Green, P., Grier, C. J., Guo, H., Guy, J., Harding, P., Hasselquist, S., Hawken, A. J., Hayes, C. R., Hearty, F., Hekker, S., Hogg, D. W., Holtzman, J. A., Horta, D., Hou, J., Hsieh, B.-C., Huber, D., Hunt, J. A. S., Chitham, J. I., Imig, J., Jaber, M., Angel, C. E. J., Johnson, J. A., Jones, A. M., Jönsson, H., Jullo, E., Kim, Y., Kinemuchi, K., Kirkpatrick, Charles C., I., Kite, G. W., Klaene, M., Kneib, J.-P., Kollmeier, J. A., Kong, H., Kounkel, M., Krishnarao, D., Lacerna, I., Lan, T.-W., Lane, R. R., Law, D. R., Le Goff, J.-M., Leung, H. W., Lewis, H., Li, C., Lian, J., Lin, L., Long, D., Longa-Peña, P., Lundgren, B., Lyke, B. W., Ted Mackereth, J., MacLeod, C. L., Majewski, S. R., Manchado, A., Maraston, C., Martini, P., Masseron, T., Masters, K. L., Mathur, S., McDermid, R. M., Merloni, A., Merrifield, M., Mészáros, S., Miglio, A.,

Minniti, D., Minsley, R., Miyaji, T., Mohammad, F. G., Mosser, B., Mueller, E.-M., Muna, D., Muñoz-Gutiérrez, A., Myers, A. D., Nadathur, S., Nair, P., Nandra, K., do Nascimento, J. C., Nevin, R. J., Newman, J. A., Nidever, D. L., Nitschelm, C., Noterdaeme, P., O'Connell, J. E., Olmstead, M. D., Oravetz, D., Oravetz, A., Osorio, Y., Pace, Z. J., Padilla, N., Palanque-Delabrouille, N., Palicio, P. A., Pan, H.-A., Pan, K., Parker, J., Paviot, R., Peirani, S., Ramŕez, K. P., Penny, S., Percival, W. J., Perez-Fournon, I., Pérez-Ràfols, I., Petitjean, P., Pieri, M. M., Pinsonneault, M., Poovelil, V. J., Povick, J. T., Prakash, A., Price-Whelan, A. M., Raddick, M. J., Raichoor, A., Ray, A., Rembold, S. B., Rezaie, M., Riffel, R. A., Riffel, R., Rix, H.-W., Robin, A. C., Roman-Lopes, A., Román-Zúñiga, C., Rose, B., Ross, A. J., Rossi, G., Rowlands, K., Rubin, K. H. R., Salvato, M., Sánchez, A. G., Sánchez-Menguiano, L., Sánchez-Gallego, J. R., Sayres, C., Schaefer, A., Schiavon, R. P., Schimoia, J. S., Schlafly, E., Schlegel, D., Schneider, D. P., Schultheis, M., Schwope, A., Seo, H.-J., Serenelli, A., Shafieloo, A., Shamsi, S. J., Shao, Z., Shen, S., Shetrone, M., Shirley, R., Aguirre, V. S., Simon, J. D., Skrutskie, M. F., Slosar, A., Smethurst, R., Sobeck, J., Sodi, B. C., Souto, D., Stark, D. V., Stassun, K. G., Steinmetz, M., Stello, D., Stermer, J., Storchi-Bergmann, T., Streblyanska, A., Stringfellow, G. S., Stutz, A., Suárez, G., Sun, J., Taghizadeh-Popp, M., Talbot, M. S., Tayar, J., Thakar, A. R., Theriault, R., Thomas, D., Thomas, Z. C., Tinker, J., Tojeiro, R., Toledo, H. H., Tremonti, C. A., Troup, N. W., Tuttle, S., Unda-Sanzana, E., Valentini, M., Vargas-González, J., Vargas-Magaña, M., Vázquez-Mata, J. A., Vivek, M., Wake, D., Wang, Y., Weaver, B. A., Weijmans, A.-M., Wild, V., Wilson, J. C., Wilson, R. F., Wolthuis, N., Wood-Vasey, W. M., Yan, R., Yang, M., Yèche, C., Zamora, O., Zarrouk, P., Zasowski, G., Zhang, K., Zhao, C., Zhao, G., Zheng, Z., Zheng, Z., Zhu, G., and Zou, H. (2020). The 16th Data Release of the Sloan Digital Sky Surveys: First Release from the APOGEE-2 Southern Survey and Full Release of eBOSS Spectra. ApJS, 249(1):3.

Akamatsu, H., Fujita, Y., Akahori, T., Ishisaki, Y., Hayashida, K., Hoshino, A., Mernier, F., Yoshikawa, K., Sato, K., and Kaastra, J. S. (2017). Properties of the cosmological filament between two clusters: A possible detection of a large-scale accretion shock by Suzaku. *A&A*, 606:A1.

Allen, S. W., Evrard, A. E., and Mantz, A. B. (2011). Cosmological Parameters from Observations of Galaxy Clusters. ARA&A, 49(1):409–470.

Aragón-Calvo, M. A., Platen, E., van de Weygaert, R., and Szalay, A. S. (2010). THE SPINE OF THE COSMIC WEB. *The Astrophysical Journal*, 723(1):364–382.

Bagchi, J., Jacob, J., Gopal-Krishna, Werner, N., Wadnerkar, N., Belapure, J., and Kumbharkhane, A. (2009). A diffuse bubble-like radio-halo source mrc 0116+111:

Imprint of agn feedback in a low-mass cluster of galaxies. *Monthly Notices of The Royal Astronomical Society - MON NOTIC ROY ASTRON SOC*, 399:601–614.

Beck, R., Anderson, J., Heald, G., Horneffer, A., Iacobelli, M., Köhler, J., Mulcahy, D., Pizzo, R., Scaife, A., Wucknitz, O., and LOFAR Magnetism Key Science Project Team (2013). The LOFAR view of cosmic magnetism. *Astronomische Nachrichten*, 334(6):548–557.

Beck, R. and Krause, M. (2005). Revised equipartition and minimum energy formula for magnetic field strength estimates from radio synchrotron observations. *Astronomische Nachrichten*, 326(6):414–427.

Best, P. N., Ker, L. M., Simpson, C., Rigby, E. E., and Sabater, J. (2014). The cosmic evolution of radio-AGN feedback to z = 1. MNRAS, 445(1):955–969.

Blasi, P. and Colafrancesco, S. (1999). Cosmic rays, radio halos and nonthermal X-ray emission in clusters of galaxies. *Astroparticle Physics*, 12(3):169–183.

Böhringer, H. and Werner, N. (2010). X-ray spectroscopy of galaxy clusters: studying astrophysical processes in the largest celestial laboratories. A&A Rev., 18(1-2):127–196.

Bond, J. R., Kofman, L., and Pogosyan, D. (1996). How filaments of galaxies are woven into the cosmic web. Nature, 380(6575):603–606.

Bonjean, V., Aghanim, N., Salomé, P., Douspis, M., and Beelen, A. (2018). Gas and galaxies in filaments between clusters of galaxies. The study of A399-A401. *A&A*, 609:A49.

Botteon, A., van Weeren, R. J., Brunetti, G., de Gasperin, F., Intema, H. T., Osinga, E., Di Gennaro, G., Shimwell, T. W., Bonafede, A., Brüggen, M., Cassano, R., Cuciti, V., Dallacasa, D., Gastaldello, F., Mandal, S., Rossetti, M., and Röttgering, H. J. A. (2020). A giant radio bridge connecting two galaxy clusters in Abell 1758. *Monthly Notices of the Royal Astronomical Society: Letters*, 499(1):L11–L15.

Brentjens, M. A. and de Bruyn, A. G. (2005). Faraday rotation measure synthesis. *A&A*, 441(3):1217–1228.

Brüggen, M., Bykov, A., Ryu, D., and Röttgering, H. (2012). Magnetic fields, relativistic particles, and shock waves in cluster outskirts. *Space Science Reviews*, 166(1):187–213.

Bruggen, M., Ensslin, T. A., and Miniati, F. (2003). The luminosity function of cluster radio relics.

Brunetti, G. and Jones, T. W. (2014). Cosmic Rays in Galaxy Clusters and Their Nonthermal Emission. *International Journal of Modern Physics D*, 23(4):1430007–98.

Brunetti, G., Setti, G., Feretti, L., and Giovannini, G. (2001). Particle reacceleration in the Coma cluster: radio properties and hard X-ray emission. *Monthly Notices of the Royal Astronomical Society*, 320(3):365–378.

Brunetti, G. and Vazza, F. (2020). Second-order fermi reacceleration mechanisms and large-scale synchrotron radio emission in intracluster bridges. *Phys. Rev. Lett.*, 124:051101.

Bryan, G. L., Norman, M. L., O'Shea, B. W., Abel, T., Wise, J. H., Turk, M. J., Reynolds, D. R., Collins, D. C., Wang, P., Skillman, S. W., Smith, B., Harkness, R. P., Bordner, J., hoon Kim, J., Kuhlen, M., Xu, H., Goldbaum, N., Hummels, C., Kritsuk, A. G., Tasker, E., Skory, S., Simpson, C. M., Hahn, O., Oishi, J. S., So, G. C., Zhao, F., Cen, R., and and, Y. L. (2014). ENZO: AN ADAPTIVE MESH REFINEMENT CODE FOR ASTROPHYSICS. *The Astrophysical Journal Supplement Series*, 211(2):19.

Burn, B. J. (1966). On the depolarization of discrete radio sources by Faraday dispersion. MNRAS, 133:67.

Cassano, R., Brunetti, G., Giocoli, C., and Ettori, S. (2016). Can giant radio halos probe the merging rate of galaxy clusters? *A&A*, 593:A81.

Cassano, R., Brunetti, G., Röttgering, H. J. A., and Brüggen, M. (2010). Unveiling radio halos in galaxy clusters in the LOFAR era. *A&A*, 509:A68.

Clark, B. G. (1980). An efficient implementation of the algorithm 'CLEAN'. *A&A*, 89(3):377.

Clarke, T. E., Kronberg, P. P., and Boehringer, H. (2001). A New radio - X-ray probe of galaxy cluster magnetic fields. *Astrophys. J. Lett.*, 547:L111–L114.

Colless, M., Peterson, B. A., Jackson, C., Peacock, J. A., Cole, S., Norberg, P., Baldry, I. K., Baugh, C. M., Bland-Hawthorn, J., Bridges, T., Cannon, R., Collins, C., Couch, W., Cross, N., Dalton, G., De Propris, R., Driver, S. P., Efstathiou, G., Ellis, R. S., Frenk, C. S., Glazebrook, K., Lahav, O., Lewis, I., Lumsden, S., Maddox, S., Madgwick, D., Sutherland, W., and Taylor, K. (2003). The 2dF Galaxy Redshift Survey: Final Data Release. *arXiv e-prints*, pages astro–ph/0306581.

Condon, J. J. and Ransom, S. M. (2016). *Essential Radio Astronomy*. Princeton University Press.

Cuciti, V., Cassano, R., Brunetti, G., Dallacasa, D., de Gasperin, F., Ettori, S., Giacintucci, S., Kale, R., Pratt, G. W., van Weeren, R. J., and Venturi, T. (2021). Radio halos in a mass-selected sample of 75 galaxy clusters. II. Statistical analysis. *A&A*, 647:A51.

de Gasperin, F., Intema, H. T., Shimwell, T. W., Brunetti, G., Brüggen, M., Enßlin, T. A., van Weeren, R. J., Bonafede, A., and Röttgering, H. J. A. (2017). Gentle reenergization of electrons in merging galaxy clusters. *Science Advances*, 3(10).

Dennison, B. (1980). Formation of radio halos in clusters of galaxies from cosmic-ray protons. ApJ, 239:L93–L96.

Di Gennaro, G., van Weeren, R. J., Hoeft, M., Kang, H., Ryu, D., Rudnick, L., Forman, W., Röttgering, H. J. A., Brüggen, M., Dawson, W. A., Golovich, N., Hoang, D. N., Intema, H. T., Jones, C., Kraft, R. P., Shimwell, T. W., and Stroe, A. (2018). Deep Very Large Array Observations of the Merging Cluster CIZA J2242.8+5301: Continuum and Spectral Imaging. ApJ, 865(1):24.

Donnert, J., Vazza, F., Brüggen, M., and ZuHone, J. (2018). Magnetic field amplification in galaxy clusters and its simulation. *Space Science Reviews*, 214(8):122.

Eckert, D., Jauzac, M., Shan, H., Kneib, J.-P., Erben, T., Israel, H., Jullo, E., Klein, M., Massey, R., Richard, J., and Tchernin, C. (2015). Warm-hot baryons comprise 5-10 per cent of filaments in the cosmic web. Nature, 528(7580):105–107.

Enßlin, T. A. and Gopal-Krishna (2001). Reviving fossil radio plasma in clusters of galaxies by adiabatic compression in environmental shock waves. *A&A*, 366:26–34.

Enßlin, T., Pfrommer, C., Miniati, F., and Subramanian, K. (2011). Cosmic ray transport in galaxy clusters: implications for radio halos, gamma-ray signatures, and cool core heating. *A&A*, 527:A99.

Gendron-Marsolais, M., Hlavacek-Larrondo, J., van Weeren, R. J., Clarke, T., Fabian, A. C., Intema, H. T., Taylor, G. B., Blundell, K. M., and Sanders, J. S. (2017). Deep 230-470 MHz VLA observations of the mini-halo in the Perseus cluster. MNRAS, 469(4):3872–3880.

Giovannini, G., Bonafede, A., Feretti, L., Govoni, F., Murgia, M., Ferrari, F., and Monti, G. (2009). Radio halos in nearby (z ¡ 0.4) clusters of galaxies. *A&A*, 507(3):1257–1270.

Govoni, F. and Feretti, L. (2004). Magnetic Fields in Clusters of Galaxies. *International Journal of Modern Physics D*, 13(8):1549–$V_\nu(u, v)$ is a continuous function, but our

measures are discrete, and $V_\nu(u,v)$ are sampled only in certain points of the (u,v) plane. Therefore, what we really measure is $V_\nu(u,v)S_\nu(u,v)$, where $S_\nu(u,v)$ is the *sampling function*, which is equal to 1 where $V_\nu(u,v)$ is measured and 0 otherwise. Therefore, what we actually do is to Fourier transform $V1594$.

Govoni, F., Orrù, E., Bonafede, A., Iacobelli, M., Paladino, R., Vazza, F., Murgia, M., Vacca, V., Giovannini, G., Feretti, L., Loi, F., Bernardi, G., Ferrari, C., Pizzo, R. F., Gheller, C., Manti, S., Brüggen, M., Brunetti, G., Cassano, R., de Gasperin, F., Enßlin, T. A., Hoeft, M., Horellou, C., Junklewitz, H., Röttgering, H. J. A., Scaife, A. M. M., Shimwell, T. W., van Weeren, R. J., and Wise, M. (2019). A radio ridge connecting two galaxy clusters in a filament of the cosmic web. *Science*, 364(6444):981–984.

Hales, C. A., Gaensler, B. M., Norris, R. P., and Middelberg, E. (2012). Analytic detection thresholds for measurements of linearly polarized intensity using rotation measure synthesis. MNRAS, 424(3):2160–2172.

Hardcastle, M. J., Gürkan, G., van Weeren, R. J., Williams, W. L., Best, P. N., de Gasperin, F., Rafferty, D. A., Read, S. C., Sabater, J., Shimwell, T. W., Smith, D. J. B., Tasse, C., Bourne, N., Brienza, M., Brüggen, M., Brunetti, G., Chyży, K. T., Conway, J., Dunne, L., Eales, S. A., Maddox, S. J., Jarvis, M. J., Mahony, E. K., Morganti, R., Prandoni, I., Röttgering, H. J. A., Valiante, E., and White, G. J. (2016). LOFAR/H-ATLAS: a deep low-frequency survey of the Herschel-ATLAS North Galactic Pole field. MNRAS, 462(2):1910–1936.

Heald, G., Braun, R., and Edmonds, R. (2009). The Westerbork SINGS survey. II Polarization, Faraday rotation, and magnetic fields. *A&A*, 503(2):409–435.

Hincks, A. D., Radiconi, F., Romero, C., Madhavacheril, M. S., Mroczkowski, T., Austermann, J. E., Barbavara, E., Battaglia, N., Battistelli, E., Bond, J. R., Calabrese, E., de Bernardis, P., Devlin, M. J., Dicker, S. R., Duff, S. M., Duivenvoorden, A. J., Dunkley, J., Dünner, R., Gallardo, P. A., Govoni, F., Hill, J. C., Hilton, M., Hubmayr, J., Hughes, J. P., Lamagna, L., Lokken, M., Masi, S., Mason, B. S., McMahon, J., Moodley, K., Murgia, M., Naess, S., Page, L., Piacentini, F., Salatino, M., Schillaci, A., Sievers, J. L., Sifón, C., Staggs, S., Ullom, J. N., Vacca, V., Van Engelen, A., Vissers, M. R., Wollack, E. J., and Xu, Z. (2021). A high-resolution view of the filament of gas between Abell 399 and Abell 401 from the Atacama Cosmology Telescope and MUSTANG-2. *arXiv e-prints*, page arXiv:2107.04611.

Högbom, J. A. (1974). Aperture Synthesis with a Non-Regular Distribution of Interferometer Baselines. A&AS, 15:417.

Huchra, J. P., Macri, L. M., Masters, K. L., Jarrett, T. H., Berlind, P., Calkins, M., Crook, A. C., Cutri, R., Erdoğdu, P., Falco, E., George, T., Hutcheson, C. M., Lahav, O., Mader, J., Mink, J. D., Martimbeau, N., Schneider, S., Skrutskie, M., Tokarz, S., and Westover, M. (2012). THE 2mass REDSHIFT SURVEY—DESCRIPTION AND DATA RELEASE. *The Astrophysical Journal Supplement Series*, 199(2):26.

Iacobelli, M., Haverkorn, M., Orrú, E., Pizzo, R. F., Anderson, J., Beck, R., Bell, M. R., Bonafede, A., Chyzy, K., Dettmar, R. J., Enßlin, T. A., Heald, G., Horellou, C., Horneffer, A., Jurusik, W., Junklewitz, H., Kuniyoshi, M., Mulcahy, D. D., Paladino, R., Reich, W., Scaife, A., Sobey, C., Sotomayor-Beltran, C., Alexov, A., Asgekar, A., Avruch, I. M., Bell, M. E., van Bemmel, I., Bentum, M. J., Bernardi, G., Best, P., Bırzan, L., Breitling, F., Broderick, J., Brouw, W. N., Brüggen, M., Butcher, H. R., Ciardi, B., Conway, J. E., de Gasperin, F., de Geus, E., Duscha, S., Eislöffel, J., Engels, D., Falcke, H., Fallows, R. A., Ferrari, C., Frieswijk, W., Garrett, M. A., Grießmeier, J., Gunst, A. W., Hamaker, J. P., Hassall, T. E., Hessels, J. W. T., Hoeft, M., Hörandel, J., Jelic, V., Karastergiou, A., Kondratiev, V. I., Koopmans, L. V. E., Kramer, M., Kuper, G., van Leeuwen, J., Macario, G., Mann, G., McKean, J. P., Munk, H., Pandey-Pommier, M., Polatidis, A. G., Röttgering, H., Schwarz, D., Sluman, J., Smirnov, O., Stappers, B. W., Steinmetz, M., Tagger, M., Tang, Y., Tasse, C., Toribio, C., Vermeulen, R., Vocks, C., Vogt, C., van Weeren, R. J., Wise, M. W., Wucknitz, O., Yatawatta, S., Zarka, P., and Zensus, A. (2013). Studying Galactic interstellar turbulence through fluctuations in synchrotron emission. First LOFAR Galactic foreground detection. *A&A*, 558:A72.

Intema, H. T., Jagannathan, P., Mooley, K. P., and Frail, D. A. (2017). The GMRT 150 MHz all-sky radio survey. First alternative data release TGSS ADR1. *A&A*, 598:A78.

Jarvis, M., Bacon, D. J., Blake, C., Brown, M. L., Lindsay, S., Raccanelli, A., Santos, M., and Schwarz, D. J. (2015). Cosmology with SKA Radio Continuum Surveys. *PoS*, AASKA14:018.

Kale, R., Venturi, T., Giacintucci, S., Dallacasa, D., Cassano, R., Brunetti, G., Cuciti, V., Macario, G., and Athreya, R. (2015). The Extended GMRT Radio Halo Survey II: Further results and analysis of the full sample. *Astron. Astrophys.*, 579:A92.

LaBella, N. (2020). First evidence of a shock in a radio mini-halocluster: implications from new lofar data.

Locatelli, N., Vazza, F., Bonafede, A., Banfi, S., Bernardi, G., Gheller, C., Botteon, A., and Shimwell, T. (2021). New constraints on the magnetic field in cosmic web filaments. *A&A*, 652:A80.

Mazzotta, P. and Giacintucci, S. (2008). Do Radio Core-Halos and Cold Fronts in Non-Major-Merging Clusters Originate from the Same Gas Sloshing? ApJ, 675(1):L9.

Miniati, F., Ryu, D., Kang, H., and Jones, T. W. (2001). Cosmic-ray protons accelerated at cosmological shocks and their impact on groups and clusters of galaxies. *The Astrophysical Journal*, 559(1):59–69.

Miniati, F., Ryu, D., Kang, H., Jones, T. W., Cen, R., and Ostriker, J. P. (2000). Properties of cosmic shock waves in large-scale structure formation. *The Astrophysical Journal*, 542(2):608–621.

Nunhokee, C. D., Bernardi, G., Manti, S., Govoni, F., Bonafede, A., Venturi, T., Dallacasa, D., Murgia, M., Orrú, E., Pizzo, R. F., Smirnov, O. M., and Vacca, V. (2021). Radio multifrequency observations of galaxy clusters. The Abell 399−401 pair. *arXiv e-prints*, page arXiv:2102.02900.

Offringa, A. R., McKinley, B., Hurley-Walker, N., Briggs, F. H., Wayth, R. B., Kaplan, D. L., Bell, M. E., Feng, L., Neben, A. R., Hughes, J. D., Rhee, J., Murphy, T., Bhat, N. D. R., Bernardi, G., Bowman, J. D., Cappallo, R. J., Corey, B. E., Deshpande, A. A., Emrich, D., Ewall-Wice, A., Gaensler, B. M., Goeke, R., Greenhill, L. J., Hazelton, B. J., Hindson, L., Johnston-Hollitt, M., Jacobs, D. C., Kasper, J. C., Kratzenberg, E., Lenc, E., Lonsdale, C. J., Lynch, M. J., McWhirter, S. R., Mitchell, D. A., Morales, M. F., Morgan, E., Kudryavtseva, N., Oberoi, D., Ord, S. M., Pindor, B., Procopio, P., Prabu, T., Riding, J., Roshi, D. A., Shankar, N. U., Srivani, K. S., Subrahmanyan, R., Tingay, S. J., Waterson, M., Webster, R. L., Whitney, A. R., Williams, A., and Williams, C. L. (2014). WSCLEAN: an implementation of a fast, generic wide-field imager for radio astronomy. MNRAS, 444(1):606–619.

O'Sullivan, S. P., Brown, S., Robishaw, T., Schnitzeler, D. H. F. M., McClure-Griffiths, N. M., Feain, I. J., Taylor, A. R., Gaensler, B. M., Landecker, T. L., Harvey-Smith, L., and Carretti, E. (2012). Complex Faraday depth structure of active galactic nuclei as revealed by broad-band radio polarimetry. MNRAS, 421(4):3300–3315.

O'Sullivan, S. P., Brüggen, M., Vazza, F., Carretti, E., Locatelli, N. T., Stuardi, C., Vacca, V., Vernstrom, T., Heald, G., Horellou, C., Shimwell, T. W., Hardcastle, M. J., Tasse, C., and Röttgering, H. (2020). New constraints on the magnetization of the cosmic web using LOFAR Faraday rotation observations. MNRAS, 495(3):2607–2619.

Pearce, C. J. J., van Weeren, R. J., Andrade-Santos, F., Jones, C., Forman, W. R., Brüggen, M., Bulbul, E., Clarke, T. E., Kraft, R. P., Medezinski, E., Mroczkowski, T., Nonino, M., Nulsen, P. E. J., Randall, S. W., and Umetsu, K. (2017). VLA radio

observations of theHSTFrontier fields cluster abell 2744: The discovery of new radio relics. *The Astrophysical Journal*, 845(1):81.

Peebles, P. J. E. (1980). *The large-scale structure of the universe.*

Peebles, P. J. E. and Yu, J. T. (1970). Primeval Adiabatic Perturbation in an Expanding Universe. ApJ, 162:815.

Pfrommer, C., Pakmor, R., Schaal, K., Simpson, C. M., and Springel, V. (2017). Simulating cosmic ray physics on a moving mesh. *Mon. Not. Roy. Astron. Soc.*, 465(4):4500–4529.

Planck Collaboration, Aghanim, N., Akrami, Y., Ashdown, M., Aumont, J., Baccigalupi, C., Ballardini, M., Banday, A. J., Barreiro, R. B., Bartolo, N., Basak, S., Battye, R., Benabed, K., Bernard, J. P., Bersanelli, M., Bielewicz, P., Bock, J. J., Bond, J. R., Borrill, J., Bouchet, F. R., Boulanger, F., Bucher, M., Burigana, C., Butler, R. C., Calabrese, E., Cardoso, J. F., Carron, J., Challinor, A., Chiang, H. C., Chluba, J., Colombo, L. P. L., Combet, C., Contreras, D., Crill, B. P., Cuttaia, F., de Bernardis, P., de Zotti, G., Delabrouille, J., Delouis, J. M., Di Valentino, E., Diego, J. M., Doré, O., Douspis, M., Ducout, A., Dupac, X., Dusini, S., Efstathiou, G., Elsner, F., Enßlin, T. A., Eriksen, H. K., Fantaye, Y., Farhang, M., Fergusson, J., Fernandez-Cobos, R., Finelli, F., Forastieri, F., Frailis, M., Fraisse, A. A., Franceschi, E., Frolov, A., Galeotta, S., Galli, S., Ganga, K., Génova-Santos, R. T., Gerbino, M., Ghosh, T., González-Nuevo, J., Górski, K. M., Gratton, S., Gruppuso, A., Gudmundsson, J. E., Hamann, J., Handley, W., Hansen, F. K., Herranz, D., Hildebrandt, S. R., Hivon, E., Huang, Z., Jaffe, A. H., Jones, W. C., Karakci, A., Keihänen, E., Keskitalo, R., Kiiveri, K., Kim, J., Kisner, T. S., Knox, L., Krachmalnicoff, N., Kunz, M., Kurki-Suonio, H., Lagache, G., Lamarre, J. M., Lasenby, A., Lattanzi, M., Lawrence, C. R., Le Jeune, M., Lemos, P., Lesgourgues, J., Levrier, F., Lewis, A., Liguori, M., Lilje, P. B., Lilley, M., Lindholm, V., López-Caniego, M., Lubin, P. M., Ma, Y. Z., Macías-Pérez, J. F., Maggio, G., Maino, D., Mandolesi, N., Mangilli, A., Marcos-Caballero, A., Maris, M., Martin, P. G., Martinelli, M., Martínez-González, E., Matarrese, S., Mauri, N., McEwen, J. D., Meinhold, P. R., Melchiorri, A., Mennella, A., Migliaccio, M., Millea, M., Mitra, S., Miville-Deschênes, M. A., Molinari, D., Montier, L., Morgante, G., Moss, A., Natoli, P., Nørgaard-Nielsen, H. U., Pagano, L., Paoletti, D., Partridge, B., Patanchon, G., Peiris, H. V., Perrotta, F., Pettorino, V., Piacentini, F., Polastri, L., Polenta, G., Puget, J. L., Rachen, J. P., Reinecke, M., Remazeilles, M., Renzi, A., Rocha, G., Rosset, C., Roudier, G., Rubiño-Martín, J. A., Ruiz-Granados, B., Salvati, L., Sandri, M., Savelainen, M., Scott, D., Shellard, E. P. S., Sirignano, C., Sirri, G., Spencer,

L. D., Sunyaev, R., Suur-Uski, A. S., Tauber, J. A., Tavagnacco, D., Tenti, M., Toffolatti, L., Tomasi, M., Trombetti, T., Valenziano, L., Valiviita, J., Van Tent, B., Vibert, L., Vielva, P., Villa, F., Vittorio, N., Wandelt, B. D., Wehus, I. K., White, M., White, S. D. M., Zacchei, A., and Zonca, A. (2020). Planck 2018 results. VI. Cosmological parameters. *A&A*, 641:A6.

Pogosyan, D., Pichon, C., Gay, C., Prunet, S., Cardoso, J. F., Sousbie, T., and Colombi, S. (2009). The local theory of the cosmic skeleton. MNRAS, 396(2):635–667.

Press, W. H. and Schechter, P. (1974). Formation of Galaxies and Clusters of Galaxies by Self-Similar Gravitational Condensation. ApJ, 187:425–438.

Purcell, C. R., Van Eck, C. L., West, J., Sun, X. H., and Gaensler, B. M. (2020). RM-Tools: Rotation measure (RM) synthesis and Stokes QU-fitting.

Raccanelli, A., Zhao, G.-B., Bacon, D. J., Jarvis, M. J., Percival, W. J., Norris, R. P., Röttgering, H., Abdalla, F. B., Cress, C. M., Kubwimana, J.-C., Lindsay, S., Nichol, R. C., Santos, M. G., and Schwarz, D. J. (2012). Cosmological measurements with forthcoming radio continuum surveys. MNRAS, 424(2):801–819.

Rajpurohit, K., Hoeft, M., van Weeren, R. J., Rudnick, L., Röttgering, H. J. A., Forman, W. R., Brüggen, M., Croston, J. H., Andrade-Santos, F., Dawson, W. A., Intema, H. T., Kraft, R. P., Jones, C., and Jee, M. J. (2018). Deep VLA observations of the cluster 1rxs j0603.3+4214 in the frequency range of 1–2 GHz. *The Astrophysical Journal*, 852(2):65.

Randall, S. W., Clarke, T. E., van Weeren, R. J., Intema, H. T., Dawson, W. A., Mroczkowski, T., Blanton, E. L., Bulbul, E., and Giacintucci, S. (2016). Multiwavelength Observations of the Dissociative Merger in the Galaxy Cluster CIZA J0107.7+5408. ApJ, 823(2):94.

Rossetti, M. and Molendi, S. (2004). Is there a hard tail in the Coma Cluster X-ray spectrum? *A&A*, 414:L41–L44.

Ruszkowski, M. and Oh, S. P. (2010). SHAKEN AND STIRRED: CONDUCTION AND TURBULENCE IN CLUSTERS OF GALAXIES. *The Astrophysical Journal*, 713(2):1332–1342.

Ryu, D., Kang, H., Hallman, E., and Jones, T. W. (2003). Cosmological shock waves and their role in the large-scale structure of the universe. *The Astrophysical Journal*, 593(2):599–610.

Schlickeiser, R., Sievers, A., and Thiemann, H. (1987). The diffuse radio emission from the Coma cluster. *A&A*, 182:21–35.

Schwarz, D. J., Bacon, D. J., Chen, S., Clarkson, C., Huterer, D., Kunz, M., Maartens, R., Raccanelli, A., Rubart, M., and Starck, J.-L. (2015). Testing foundations of modern cosmology with SKA all-sky surveys. *PoS*, AASKA14:032.

Shimwell, T. W., Röttgering, H. J. A., Best, P. N., Williams, W. L., Dijkema, T. J., de Gasperin, F., Hardcastle, M. J., Heald, G. H., Hoang, D. N., Horneffer, A., Intema, H., Mahony, E. K., Mandal, S., Mechev, A. P., Morabito, L., Oonk, J. B. R., Rafferty, D., Retana-Montenegro, E., Sabater, J., Tasse, C., van Weeren, R. J., Brüggen, M., Brunetti, G., Chyży, K. T., Conway, J. E., Haverkorn, M., Jackson, N., Jarvis, M. J., McKean, J. P., Miley, G. K., Morganti, R., White, G. J., Wise, M. W., van Bemmel, I. M., Beck, R., Brienza, M., Bonafede, A., Calistro Rivera, G., Cassano, R., Clarke, A. O., Cseh, D., Deller, A., Drabent, A., van Driel, W., Engels, D., Falcke, H., Ferrari, C., Fröhlich, S., Garrett, M. A., Harwood, J. J., Heesen, V., Hoeft, M., Horellou, C., Israel, F. P., Kapińska, A. D., Kunert-Bajraszewska, M., McKay, D. J., Mohan, N. R., Orrú, E., Pizzo, R. F., Prandoni, I., Schwarz, D. J., Shulevski, A., Sipior, M., Smith, D. J. B., Sridhar, S. S., Steinmetz, M., Stroe, A., Varenius, E., van der Werf, P. P., Zensus, J. A., and Zwart, J. T. L. (2017). The LOFAR Two-metre Sky Survey. I. Survey description and preliminary data release. *A&A*, 598:A104.

Shimwell, T. W., Tasse, C., Hardcastle, M. J., Mechev, A. P., Williams, W. L., Best, P. N., Röttgering, H. J. A., Callingham, J. R., Dijkema, T. J., de Gasperin, F., Hoang, D. N., Hugo, B., Mirmont, M., Oonk, J. B. R., Prandoni, I., Rafferty, D., Sabater, J., Smirnov, O., van Weeren, R. J., White, G. J., Atemkeng, M., Bester, L., Bonnassieux, E., Brüggen, M., Brunetti, G., Chyży, K. T., Cochrane, R., Conway, J. E., Croston, J. H., Danezi, A., Duncan, K., Haverkorn, M., Heald, G. H., Iacobelli, M., Intema, H. T., Jackson, N., Jamrozy, M., Jarvis, M. J., Lakhoo, R., Mevius, M., Miley, G. K., Morabito, L., Morganti, R., Nisbet, D., Orrú, E., Perkins, S., Pizzo, R. F., Schrijvers, C., Smith, D. J. B., Vermeulen, R., Wise, M. W., Alegre, L., Bacon, D. J., van Bemmel, I. M., Beswick, R. J., Bonafede, A., Botteon, A., Bourke, S., Brienza, M., Calistro Rivera, G., Cassano, R., Clarke, A. O., Conselice, C. J., Dettmar, R. J., Drabent, A., Dumba, C., Emig, K. L., Enßlin, T. A., Ferrari, C., Garrett, M. A., Génova-Santos, R. T., Goyal, A., Gürkan, G., Hale, C., Harwood, J. J., Heesen, V., Hoeft, M., Horellou, C., Jackson, C., Kokotanekov, G., Kondapally, R., Kunert-Bajraszewska, M., Mahatma, V., Mahony, E. K., Mandal, S., McKean, J. P., Merloni, A., Mingo, B., Miskolczi, A., Mooney, S., Nikiel-Wroczyński, B., O'Sullivan, S. P., Quinn, J., Reich, W., Roskowiński, C., Rowlinson, A., Savini, F.,

Saxena, A., Schwarz, D. J., Shulevski, A., Sridhar, S. S., Stacey, H. R., Urquhart, S., van der Wiel, M. H. D., Varenius, E., Webster, B., and Wilber, A. (2019). The LOFAR Two-metre Sky Survey. II. First data release. *A&A*, 622:A1.

SloanDigitalSkySurvey-WebSite (n.d.). "https://www.sdss.org/science/".

Smith, D. J. B., Jarvis, M. J., Hardcastle, M. J., Vaccari, M., Bourne, N., Dunne, L., Ibar, E., Maddox, N., Prescott, M., Vlahakis, C., Eales, S., Maddox, S. J., Smith, M. W. L., Valiante, E., and de Zotti, G. (2014). The temperature dependence of the far-infrared-radio correlation in the Herschel-ATLAS. MNRAS, 445(3):2232–2243.

Sokoloff, D. D., Bykov, A. A., Shukurov, A., Berkhuijsen, E. M., Beck, R., and Poezd, A. D. (1998). Depolarization and Faraday effects in galaxies. MNRAS, 299(1):189–206.

Springel, V., White, S. D. M., Jenkins, A., Frenk, C. S., Yoshida, N., Gao, L., Navarro, J., Thacker, R., Croton, D., Helly, J., Peacock, J. A., Cole, S., Thomas, P., Couchman, H., Evrard, A., Colberg, J., and Pearce, F. (2005a). Simulations of the formation, evolution and clustering of galaxies and quasars. Nature, 435(7042):629–636.

Springel, V., White, S. D. M., Jenkins, A., Frenk, C. S., Yoshida, N., Gao, L., Navarro, J., Thacker, R., Croton, D., Helly, J., Peacock, J. A., Cole, S., Thomas, P., Couchman, H., Evrard, A., Colberg, J., and Pearce, F. (2005b). Simulations of the formation, evolution and clustering of galaxies and quasars. Nature, 435(7042):629–636.

Stuardi, C. (2021). *Magnetic fields in radio relics and in the outskirts of galaxy clusters*. PhD thesis, Alma Mater Studiorum - Università di Bologna.

Sunyaev, R. A. and Zeldovich, Y. B. (1972). Formation of Clusters of Galaxies; Protocluster Fragmentation and Intergalactic Gas Heating. *A&A*, 20:189.

van Haarlem, M. P., Wise, M. W., Gunst, A. W., Heald, G., McKean, J. P., Hessels, J. W. T., de Bruyn, A. G., Nijboer, R., Swinbank, J., Fallows, R., Brentjens, M., Nelles, A., Beck, R., Falcke, H., Fender, R., Hörandel, J., Koopmans, L. V. E., Mann, G., Miley, G., Röttgering, H., Stappers, B. W., Wijers, R. A. M. J., Zaroubi, S., van den Akker, M., Alexov, A., Anderson, J., Anderson, K., van Ardenne, A., Arts, M., Asgekar, A., Avruch, I. M., Batejat, F., Bähren, L., Bell, M. E., Bell, M. R., van Bemmel, I., Bennema, P., Bentum, M. J., Bernardi, G., Best, P., Bîrzan, L., Bonafede, A., Boonstra, A.-J., Braun, R., Bregman, J., Breitling, F., van de Brink, R. H., Broderick, J., Broekema, P. C., Brouw, W. N., Brüggen, M., Butcher, H. R., van Cappellen, W., Ciardi, B., Coenen, T., Conway, J., Coolen, A., Corstanje, A., Damstra, S., Davies, O., Deller, A. T., Dettmar, R.-J., van Diepen, G., Dijkstra,

K., Donker, P., Doorduin, A., Dromer, J., Drost, M., van Duin, A., Eislöffel, J., van Enst, J., Ferrari, C., Frieswijk, W., Gankema, H., Garrett, M. A., de Gasperin, F., Gerbers, M., de Geus, E., Grießmeier, J.-M., Grit, T., Gruppen, P., Hamaker, J. P., Hassall, T., Hoeft, M., Holties, H. A., Horneffer, A., van der Horst, A., van Houwelingen, A., Huijgen, A., Iacobelli, M., Intema, H., Jackson, N., Jelic, V., de Jong, A., Juette, E., Kant, D., Karastergiou, A., Koers, A., Kollen, H., Kondratiev, V. I., Kooistra, E., Koopman, Y., Koster, A., Kuniyoshi, M., Kramer, M., Kuper, G., Lambropoulos, P., Law, C., van Leeuwen, J., Lemaitre, J., Loose, M., Maat, P., Macario, G., Markoff, S., Masters, J., McFadden, R. A., McKay-Bukowski, D., Meijering, H., Meulman, H., Mevius, M., Middelberg, E., Millenaar, R., Miller-Jones, J. C. A., Mohan, R. N., Mol, J. D., Morawietz, J., Morganti, R., Mulcahy, D. D., Mulder, E., Munk, H., Nieuwenhuis, L., van Nieuwpoort, R., Noordam, J. E., Norden, M., Noutsos, A., Offringa, A. R., Olofsson, H., Omar, A., Orrú, E., Overeem, R., Paas, H., Pandey-Pommier, M., Pandey, V. N., Pizzo, R., Polatidis, A., Rafferty, D., Rawlings, S., Reich, W., de Reijer, J.-P., Reitsma, J., Renting, G. A., Riemers, P., Rol, E., Romein, J. W., Roosjen, J., Ruiter, M., Scaife, A., van der Schaaf, K., Scheers, B., Schellart, P., Schoenmakers, A., Schoonderbeek, G., Serylak, M., Shulevski, A., Sluman, J., Smirnov, O., Sobey, C., Spreeuw, H., Steinmetz, M., Sterks, C. G. M., Stiepel, H.-J., Stuurwold, K., Tagger, M., Tang, Y., Tasse, C., Thomas, I., Thoudam, S., Toribio, M. C., van der Tol, B., Usov, O., van Veelen, M., van der Veen, A.-J., ter Veen, S., Verbiest, J. P. W., Vermeulen, R., Vermaas, N., Vocks, C., Vogt, C., de Vos, M., van der Wal, E., van Weeren, R., Weggemans, H., Weltevrede, P., White, S., Wijnholds, S. J., Wilhelmsson, T., Wucknitz, O., Yatawatta, S., Zarka, P., Zensus, A., and van Zwieten, J. (2013). Lofar: The low-frequency array. *A&A*, 556:A2.

van Weeren, R. J., de Gasperin, F., Akamatsu, H., Brüggen, M., Feretti, L., Kang, H., Stroe, A., and Zandanel, F. (2019). Diffuse radio emission from galaxy clusters. *Space Science Reviews*, 215(1):16.

van Weeren, R. J., Williams, W. L., Hardcastle, M. J., Shimwell, T. W., Rafferty, D. A., Sabater, J., Heald, G., Sridhar, S. S., Dijkema, T. J., Brunetti, G., Brüggen, M., Andrade-Santos, F., Ogrean, G. A., Röttgering, H. J. A., Dawson, W. A., Forman, W. R., de Gasperin, F., Jones, C., Miley, G. K., Rudnick, L., Sarazin, C. L., Bonafede, A., Best, P. N., Bîrzan, L., Cassano, R., Chyży, K. T., Croston, J. H., Ensslin, T., Ferrari, C., Hoeft, M., Horellou, C., Jarvis, M. J., Kraft, R. P., Mevius, M., Intema, H. T., Murray, S. S., Orrú, E., Pizzo, R., Simionescu, A., Stroe, A., van der Tol, S., and White, G. J. (2016). LOFAR FACET CALIBRATION. *The Astrophysical Journal Supplement Series*, 223(1):2.

Vazza, F., Brüggen, M., Gheller, C., Hackstein, S., Wittor, D., and Hinz, P. M. (2017). Simulations of extragalactic magnetic fields and of their observables. *Classical and Quantum Gravity*, 34(23):234001.

Vernstrom, T., Gaensler, B. M., Brown, S., Lenc, E., and Norris, R. P. (2017). Low-frequency radio constraints on the synchrotron cosmic web. MNRAS, 467(4):4914–4936.

Vernstrom, T., Heald, G., Vazza, F., Galvin, T. J., West, J. L., Locatelli, N., Fornengo, N., and Pinetti, E. (2021). Discovery of magnetic fields along stacked cosmic filaments as revealed by radio and X-ray emission. MNRAS, 505(3):4178–4196.

Voit, G. M. (2005). Tracing cosmic evolution with clusters of galaxies. *Reviews of Modern Physics*, 77(1):207–258.

Wik, D. R., Sarazin, C. L., Finoguenov, A., Matsushita, K., Nakazawa, K., and Clarke, T. E. (2009). ASUZAKUSEARCH FOR NONTHERMAL EMISSION AT HARD x-RAY ENERGIES IN THE COMA CLUSTER. *The Astrophysical Journal*, 696(2):1700–1711.

Wilman, R. J., Miller, L., Jarvis, M. J., Mauch, T., Levrier, F., Abdalla, F. B., Rawlings, S., Klöckner, H. R., Obreschkow, D., Olteanu, D., and Young, S. (2008). A semi-empirical simulation of the extragalactic radio continuum sky for next generation radio telescopes. MNRAS, 388(3):1335–1348.

Wittor, D., Domínguez-Fernández, P., Vazza, F., and Brüggen, M. (2019). A Song of Shocks and Dynamo: Numerical Studies of a Galaxy Cluster Merger in the HIMAG Project. *arXiv e-prints*, page arXiv:1909.10792.

Xu, Y., Kronberg, P. P., Habib, S., and Dufton, Q. W. (2006). A faraday rotation search for magnetic fields in large-scale structure. *The Astrophysical Journal*, 637(1):19–26.

Zel'Dovich, Y. B. (1970). Reprint of 1970A&A.....5...84Z. Gravitational instability: an approximate theory for large density perturbations. *A&A*, 500:13–18.

Zwicky, F. (1937). On the Masses of Nebulae and of Clusters of Nebulae. ApJ, 86:217.